Aus der
Klinik und Poliklinik für Nuklearmedizin
Klinik der Universität München
Direktor: Prof. Dr. Rudolf Alexander Werner

In vivo Detektion von
reaktiver Astrozytose und Synapsenverlust
in Alzheimer-Mausmodellen
mittels Positronen-Emissions-Tomographie

Dissertation
zum Erwerb des Doktorgrades der Medizin
an der Medizinischen Fakultät
der Ludwig-Maximilians-Universität zu München

vorgelegt von
Anna Ballweg, geb. Schander

aus
Thälmann

Jahr
2025

Mit Genehmigung der Medizinischen Fakultät
der Universität München

Berichterstatter:	Prof. Dr. Dr. Matthias Brendel
Mitberichterstatter:	PD Dr. Matthias P. Fabritius
	Dr. Michael Dieter Ludwig Willem
	Prof. Dr. Dominik Paquet
Mitbetreuung durch den promovierten Mitarbeiter:	Dr. Johannes Gnörich
Dekan:	Prof. Dr. med. Thomas Gudermann
Tag der mündlichen Prüfung:	10.07.2025

I. Affidavit und Übereinstimmungserklärung

LUDWIG-
MAXIMILIANS-
UNIVERSITÄT
MÜNCHEN
LMU

Promotionsbüro
Medizinische Fakultät

MMRS

Eidesstattliche Versicherung

Ballweg, Anna
_____
Name, Vorname

Ich erkläre hiermit an Eides statt, dass ich die vorliegende Dissertation mit dem Titel:

In vivo Detektion von reaktiver Astrozytose und Synapsenverlust in Alzheimer-Mausmodellen

mittels Positronen-Emissions-Tomographie

selbständig verfasst, mich außer der angegebenen keiner weiteren Hilfsmittel bedient und alle Er-kenntnisse, die aus dem Schrifttum ganz oder annähernd übernommen sind, als solche kenntlich gemacht und nach ihrer Herkunft unter Bezeichnung der Fundstelle einzeln nachgewiesen habe.

Ich erkläre des Weiteren, dass die hier vorgelegte Dissertation nicht in gleicher oder in ähnlicher Form bei einer anderen Stelle zur Erlangung eines akademischen Grades eingereicht wurde.

Külsheim, 17.03.2025   Anna Ballweg
_____   _____
Ort, Datum   Unterschrift Doktorandin bzw. Doktorand

LUDWIG-MAXIMILIANS-UNIVERSITÄT MÜNCHEN

Dekanat Medizinische Fakultät
Promotionsbüro

Erklärung zur Übereinstimmung der gebundenen Ausgabe der Dissertation mit der elektronischen Fassung

Ballweg, Anna
_____
Name, Vorname

Hiermit erkläre ich, dass die elektronische Version der eingereichten Dissertation mit dem Titel:

**In vivo Detektion von reaktiver Astrozytose und Synapsenverlust
in Alzheimer-Mausmodellen mittels Positronen-Emissions-Tomographie**

in Inhalt und Formatierung mit den gedruckten und gebundenen Exemplaren übereinstimmt.

Külsheim, 14.07.2025
_____
Ort, Datum

Anna Ballweg
_____
Unterschrift Anna Ballweg

Übereinstimmung abgegebener Exemplare   Stand: 14.07.2025

Inhaltsverzeichnis

II. Abkürzungsverzeichnis

AD	Alzheimer's Disease
APP	Amyloid Precursor Protein
β	Beta
FDG	Fluoroxyglucose
[^{18}F]F-DED	[^{18}F]Fluorodeprenyl-D2
FAD	Familial Alzheimer Disease
GFAP	Glial Fibrillary Acidic Protein
MAO	Monoaminooxidase
MAPT	Mikrotubuli-assoziiertes Protein-Tau
PET	Positronen-Emissions-Tomographie
PS	Presenilin
TG	Transgen
TSPO	Translokatorprotein
SV2A	Synaptisches Vesikel-Glukoprotein 2a
VOI	Volume-of-Interest
WT	Wildtyp

1.   Publikationen der kumulativen Dissertation und Beschreibung des Eigenanteils

1.1   Publikationsliste

Die vorliegende kumulative Dissertation umfasst zwei bereits publizierte Manuskripte:

Ballweg A, Klaus C, Vogler L, Katzdobler S, Wind K, Zatcepin A, Ziegler SI, Secgin B, Eckenweber F, Bohr B, Bernhardt A, Fietzek U, Rauchmann BS, Stoecklein S, Quach S, Beyer L, Scheifele M, Simmet M, Joseph E, Lindner S, Berg I, Koglin N, Mueller A, Stephens AW, Bartenstein P, Tonn JC, Albert NL, Kümpfel T, Kerschensteiner M, Perneczky R, Levin J, Paeger L, Herms J, Brendel M. **[^{18}F]F-DED PET imaging of reactive astrogliosis in neurodegenerative diseases: preclinical proof of concept and first-in-human data.** J Neuroinflammation. 2023 Mar 11;20(1):68. doi: 10.1186/s12974-023-02749-2. PMID: 36906584; PMCID: PMC10007845.

Vogler L, **Ballweg A**, Bohr B, Briel N, Wind K, Antons M, Kunze LH, Gnörich J, Lindner S, Gildehaus FJ, Baumann K, Bartenstein P, Boening G, Ziegler SI, Levin J, Zwergal A, Höglinger GU, Herms J, Brendel M. **Assessment of synaptic loss in mouse models of β-amyloid and tau pathology using [^{18}F]UCB-H PET imaging.** Neuroimage Clin. 2023;39:103484. doi: 10.1016/j.nicl.2023.103484. Epub 2023 Jul 26. PMID: 37541098;

1.2 Beitrag zu Paper I: "[¹⁸F]F-DED PET imaging of reactive astrogliosis in neurodegenerative diseases: preclinical proof of concept and first-in-human data"

Erarbeitung eines Studienkonzepts gemeinsam mit dem Betreuer. Mitarbeit bei Versorgung und Überwachung der Versuchsmäuse. Durchführung der Kleintier PET Scans mit den drei Radiotracern [¹⁸F]F-DED, [¹⁸F]GE-180 und [¹⁸F]-Florbetaben. Prozessierung der Datensätze aus den PET Scans mit anschließender statistischer Analyse, Auswertung und Interpretation der Scan-Daten und der Immunhistochemie, stets in enger Absprache mit dem Betreuer. Erstellung der Abbildungen, Tabellen, Graphen und Diagrammen. Literaturrecherche, vor allem mit dem Schwerpunkt auf dem neuartigen Tracer [¹⁸F]F-DED und reaktiver Astrozytose. Verfassen eines ersten Manuskriptes, Überarbeitung des Entwurfs bis zur finalen Abstimmung mit dem Betreuer. Erstellen einer Response-Datei nach Eingang des Reviews und erneute Überarbeitung des Manuskript.

Wir entschieden uns für eine geteilte Erstautorenschaft, um die präklinischen PET Daten multimodal und translational zu publizieren (drei Säulen). Es erfolgte die präklinische Analyse und Evaluierung mit PET Scans in einem Mausmodell zur Untersuchung des neuen Tracers [¹⁸F]F-DED und ein Vergleich mit anderen Tracern. Als zweite Säule Validierung der PET Daten durch den Goldstandard der Histologie bzw. Immunhistochemie (Anteil Carolin Klaus). Um einen translationalen Ausblick in die praktische Anwendung des Tracers zu geben, erfolgte die Untersuchung des Tracers in humanen Scans als dritte Säule (Anteil Letizia Vogler).

1.3 Beitrag zu Paper II: "Assessment of synaptic loss in mouse models of β-amyloid and tau pathology using [^{18}F]UCB-H PET imaging"

Mitarbeit bei Versorgung und Überwachung der Versuchsmäuse. Mithilfe bei der Durchführung der Kleintier PET Scans mit den Radiotracern [^{18}F]FDG, [^{18}F]UCB-H und [^{18}F]GE-180. Einarbeitung einer weiteren Doktorandin in die Prozessierung, Auswertung und Analyse der Daten der Kleintier PET Scans. Prozessierung der Datensätze aus den PET Scans mit anschließender Sichtung, statistischer Analyse, Auswertung und Interpretation der Daten. Beitrag zur Erstellung eines primären Manuskripts.

Wir entschieden uns für eine Koautorenschaft, da der praktische Studienteil (Versorgung Versuchstiere, Scans, Einarbeitung in bzw. Mithilfe bei Datenauswertung) hauptsächlich durch Bernd Bohr und mich durchgeführt wurden. Letizia Vogler übernahm die Erstellung der Darstellungen, Graphen und Diagramme sowie des Manuskripts mit Implementierung der Revisionsanmerkungen der Gutachter des Journals.

2. Einleitung

2.1 Allgemeine Einführung

Der Begriff „Demenz" umfasst eine heterogene Gruppe von Erkrankungen, die vor allem durch den Verlust der geistigen Leistungsfähigkeit und Alltagskompetenzen gekennzeichnet sind. Durch das Auftreten von Einschränkungen in multiplen Bereichen, wie beispielsweise Störungen des Gedächtnisses, der Orientierung, des Urteilvermögens, der Sprache und Motorik sowie der sozialen Interaktion, leiden Betroffene unter einer stark eingeschränkten Lebensqualität. Der Morbus Alzheimer stellt die häufigste Form der dementiellen Syndrome dar [1] und führt aufgrund der steigenden Inzidenz zu einer wachsenden Belastung für das Gesundheitswesen [2]. Schätzungen der Weltgesundheitsorganisation zufolge leiden rund 55 Millionen Menschen weltweit an einer Demenz. Es wird erwartet, dass diese Zahl infolge des demographischen Wandels der Gesellschaft bis zum Jahr 2030 auf 78 Millionen und bis zum Jahr 2050 auf 139 Millionen steigen wird [3]. Dies geht zum einen mit einer sozialen Belastung für Patienten und Angehörige und zum anderen mit einer finanziellen Herausforderung für die Industrienationen einher. Gemäß den Angaben des statistischen Bundesamtes summierten sich die Krankheitskosten für Demenz im Jahr 2020 in Deutschland auf knapp 20 Milliarden Euro. Das stellt einen Anteil von 4,6% an den gesamten Krankheitskosten dar [4]. Angesichts dieser zunehmenden gesamtgesellschaftlichen Relevanz wächst der Stellenwert der Erforschung neuer frühdiagnostischer und therapeutischer Biomarker beziehungsweise Medikamente. Die bisherige Therapie des Morbus Alzheimer basiert auf einer symptomatischen Behandlung durch Acteylcholinesteraseinhibitoren und nicht-kompetitiven NMDA-Antagonisten [5, 6]. Dabei ist der Bedarf in Bezug auf krankheitsmodifizierende Medikamente hoch. Es existiert bereits eine Vielzahl klinischer Studien zu monoklonalen Antikörpern, die gegen β-Amyloid gerichtet sind. Als potentielle spezifische Therapeutika sind Aducanumab und Lecanemab (BAN2401) als neuere Antikörper gegen spezifische

β-Amyloid-Subtypen gerichtet [7] und werden durch die U.S. Food and Drug Administration (FDA) für eine beschleunigte Zulassung geprüft [8]. Neue Ansätze verfolgen die Untersuchung von immunmodulatorischen Medikamenten, die unter anderem – durch Aktivierung oder Hemmung – in die Regulierung von Neuroinflammation eingreifen [9]. Dies könnte eine mögliche Ergänzung zu den monoklonalen Antikörpern in Bezug auf krankheitsmodifizierenden Therapien von Morbus Alzheimer sein.

2.2   Pathophysiologie des Morbus Alzheimer

Die Diagnostik und Detektion der neuropathologischen Auffälligkeiten des Morbus Alzheimer verschob sich aufgrund intensiver Forschung von einer ursprünglich rein pathologischen (post mortem), zu klinisch-symptomatisch, zu schließlich klinisch und biologisch (Biomarker in PET und Liquor, Bildgebung). Das ATN-Schema umfasst die charakteristischen Merkmale der Alzheimer Krankheit: extrazelluläre β-Amyloid Plaques (A), intrazelluläre Fibrillen aus hyperphosphoryliertem Tau-Protein (T) und die unter anderem daraus resultierende Neurodegeneration (N) [10]. Die einzelnen Pathologien weisen eine enge Wechselwirkung in ihrer Entstehung und Ausprägung auf. Basierend auf der Amyloid-Kaskade-Hypothese, stellt die Bildung und Akkumulation von β-Amyloid Ablagerungen vermutlich die zentrale Pathologie im Anfangsstadium dar, während die Aggregation der charakteristischen Tau Fibrillen zu einem späteren Zeitpunkt erfolgt [11-13]. Aktuelle Studien erweitern das ATN-Schema um „X" zum ATX(N)-Schema. Durch das „X" wird beispielsweise der Stellenwert der Neuroinflammation als ein weiterer Pathomechanismus hervorgehoben, wobei unter anderem eine neuroimmunologische Dysregulation, synaptische Dysfunktion und Veränderungen in der Blut-Hirn-Schranke darunter subsumiert werden [14]. In den letzten Jahren nahm das Interesse an der Untersuchung der Rolle von nicht-neuronalen Zellen in der Pathophysiologie neurologischer Erkrankungen, insbesondere der Alzheimer Krankheit, zu. Es gibt zunehmend Hinweise, dass Neuroinflammation ein weiteres zentrales Hauptmerkmal der Krankheit ist. Ein be-

sonderes Augenmerk liegt auf der Erforschung der Frage, ob Neuroinflammation als primäres oder sekundäres Ereignis im Verlauf neurodegenerativer Erkrankungen auftritt und ob dieses Auftreten eine neurotoxische oder neuroprotektive Wirkung auf den Hirnmetabolismus aufweist [15, 16]. Dysregulierte Mikroglia und reaktive Astrozyten tragen erheblich zum Fortschreiten der Alzheimer Krankheit und verschiedener anderer neurodegenerativer Erkrankungen bei, oft bereits vor dem Einsetzen des kognitiven Verfalls und dem Anstieg anderer Biomarker [17-19]. Insbesondere der Nachweis reaktiver Astrozyten als entzündlicher Biomarker bietet das Potential für die Detektion von Neuroinflammation [19]. Dysfunktionale Neuronen, die exemplarisch durch Aggregation von β-Amyloid und Tau entstehen, führen zu einer Aktivierung einer mikroglialen Immunantwort. Die reaktive Mikroglia sezerniert Zytokine, die eine funktionelle Umstellung der Astrozyten bewirken. Die dadurch entstandene Reaktivität der Astrozyten bedingt den Verlust ihrer unterstützenden Wirkung auf die Neuronen und verursacht stattessen Neurotoxizität. Dieser Prozess löst einen Synapsenverlust und Untergang von Neuronen aus, was wiederum zu weiterer Neurodegeneration führt [20].

2.3   Neuroinflammation in der Pathophysiologie – Astrozytose

Astrozyten sind die am häufigsten vorkommenden Immunzellen im Gehirn von Säugetieren [21]. Die physiologischen Aufgaben der Astrozyten umfassen exemplarisch die Aufrechterhaltung der Homöostase durch Eingriff in den Ionen- und Neurotransmitterhaushalt, den Schutz des zentralen Nervensystems, die Beteiligung an der Bildung der Blut-Hirn-Schranke und die Phagozytose [22]. Astrozyten besitzen die Fähigkeit durch Änderung ihrer Funktion, Morphologie und ihres Genexpressionsprofils einen reaktiven Zustand infolge verschiedener Stimuli, wie dem Untergang von Neuronen, einzunehmen [23]. Dieser reaktive Zustand kann in diversen neurodegenerativen Prozessen oder nach Gehirnverletzungen beobachtet werden [24-26]. Reaktive Astrozyten zeigen eine Hochregulation von Proteinen auf, wie beispielsweise dem glial fibrillary acidic protein (GFAP)

[27], das als Biomarker für Astrozytose im Hirngewebe, Blut oder Liquor bestimmt werden kann [23]. Das Flavoprotein Monoaminoxidase (MAO) kommt in zwei Isoformen (MAO-A und MAO-B) vor. Die Funktion des Enzyms MAO-B ist unter anderem der Katabolismus von Katecholaminen, wie beispielsweise der Abbau von Dopamin [28, 29]. MAO-B stellt neben GFAP einen weiteren Surrogatmarker für reaktive Astrozytose dar [30]. Im Gegensatz zu GFAP kann MAO-B mittels Radiotracer in PET Scans quantifiziert werden. MAO-B befindet sich überwiegend in der äußeren Mitochondrienmembran in Astrozyten [29]. Es ist außerdem in geringeren Mengen in serotonergen Neuronen, Oligodendrozyten und Mikroglia zu finden [31]. Eine Überexpression von MAO-B in reaktiven Astrozyten kann aufgrund von neuroinflammatorischen Prozessen bei Morbus Alzheimer festgestellt werden [32].

2.4   Neurodegeneration in der Pathophysiologie – Synapsenverlust

Synapsen sind essenziell für die kognitive Funktion des gesunden Menschen. Der durch Neurodegeneration verursachte Synapsenverlust stellt einen elementaren Bestandteil neurodegenerativer Erkrankungen dar [33, 34]. So kommt es bei Morbus Alzheimer zu einem relevanten Abfall der Synapsendichte in verschiedenen Hirnregionen, wie beispielsweise dem Hippocampus, was sich durch eine signifikante Korrelation zwischen Synapsenanzahl und dem Ergebnis in Mini Mental State Untersuchung zeigte [35]. Das synaptische Vesikel-Glukoprotein 2 (SV2) ist ein Protein, das in der Membran von synaptischen sekretorischen Vesikeln von Neuronen und endokrinen Zellen lokalisiert ist [36, 37]. Die Isoform SV2A wird ubiquitär im Gehirn exprimiert [38] und dient als Biomarker für die Synapsendichte. SV2A fungiert als Bindungsstelle für das Antiepileptikum Levetiracetam [39], wodurch eine Abwandlung des Antiepileptikums als Radioligand in der PET Bildgebung als Synapsendichtemarker dienen kann [40].

2.5 PS2APP und P301S – transgene Mausmodelle für Proteinaggregation bei Morbus Alzheimer

Die Etablierung transgener Mausmodelle in der präklinischen Forschung dient als Basis für ein besseres Verständnis der molekularpathologischen Besonderheiten verschiedener neurodegenerativer Erkrankungen wie dem Morbus Alzheimer. Untersuchungen an transgenen Mausmodellen bieten die Möglichkeit neue diagnostische und medikamentöse Ansätze zu evaluieren [41]. Der Anteil der autosomal-dominant vererbten Form der familiären Alzheimer-Krankheit (FAD) an allen Alzheimer Demenzen liegt bei lediglich unter 1% [42]. Gleichwohl ist das wissenschaftliche Interesse an der Untersuchung der hereditären Form groß, da die Erforschung der betroffenen Gene einen wichtigen Beitrag zu einem besseren Verständnis der pathophysiologischen Prozesse der Krankheit leisten. Humane Gene die Veränderungen in unterschiedlichen Proteinen auslösen, wie das Amyloid Precursor Protein (APP), Presenilin 1/2 (PS1, PS2), Mikrotubuli-assoziiertes Tau-Protein (MAPT), werden in Mäusestämme eingebracht und lösen dort eine molekularpathologische Kaskade mit Ausbildung von β-Amyloid Plaques beziehungsweise Tau Fibrillen aus [43].

Das transgene Mausmodell **PS2APP** umfasst ein β-Amyloid Modell, das durch die Überexpression von mutierten humanen Formen von PS2 (N141I) und APP (K670N, M671L) gekennzeichnet ist [44]. Die Entstehung erster Amyloid Plaques kann bereits im Alter von fünf bis sechs Monaten im Cortex und Hippocampus festgestellt werden [45].

Bei **P301S** Mäusen handelt es sich um ein Tau Modell, welches überwiegend die 4-repeat Isoform exprimiert, jedoch auch Anteile der für die Alzheimer Krankheit typischen 3/4R Isoform aufweisen. Diese Mauslinie ist gekennzeichnet durch die gleichnamige Expression einer mutierten Form des menschlichen MAPT-Gens. Ausgelöst durch die Mutation wird hyperphosphoryliertes Tau ausgebildet, das sich zu Tau Fibrillen im zerebra-

len Cortex, Hippocampus und Hirnstamm ablagern [46]. Dies führt wiederum, im Vergleich zu gesunden Wildtypmäusen, zu einer Neuroinflammation in oben genannten Hirnbereichen [47].

Als Basis für diese transgenen Mausmodelle dienen meist **C57BL/6** Wildtypen.

2.6   Radioliganden und PET-Bildgebung in transgenen Mausmodellen des Morbus Alzheimer

Die Verwendung von PET für molekulare Bildgebung in transgenen Mausmodellen die spezifische pathognomonische Pathologien ausweisen, bietet die einzigartige Möglichkeit das quantitative und qualitative Auftreten und die Interaktion unterschiedlicher Biomarker zu untersuchen. Ebenso können Veränderungen in der Pathologieausprägung longitudinal in vivo beobachtet werden, um den Krankheitsprozess im Verlauf zu charakterisieren. Hierzu existieren bereits diverse etablierte Radiotracer, die eine nicht-invasive Untersuchung verschiedener molekularer Zielstrukturen im Gehirn ermöglichen. Das Vorhandensein von β-Amyloid und der Verlauf der Amyloidose können beispielsweise durch den Radiotracer [18F]-Florbetaben detektiert werden [48, 49].

Der Radiotracer [18F]-Fluorodeoxyglucose ([18F]-FDG) erlaubt die Analyse des cerebralen Glukosestoffwechsels in vivo. Bei der Evaluierung der Rolle des Glukosemetabolismus in transgenen Mausmodellen ergeben sich diskrepante Ergebnisse. Während bei Patienten mit Morbus Alzheimer in bestimmten Hirnarealen ein Hypometabolismus aufgrund von des Untergangs von Neuronen beobachtet werden kann [50], weisen einige Mauslinien ein Hypermetabolismus auf, der möglicherweise durch einen erhöhten Stoffwechsel in Astrozyten und Mikroglia basierend auf Neuroinflammation erklärt werden kann [51].

Bei der PET Bildgebung von Neuroinflammation erwies sich der TSPO-Ligand [18F]GE-180 als geeigneter Tracer für die Detektion aktivierter Mikroglia [52, 53]. Als Proteinziel-

struktur dient das 18-kD Translokatorprotein (TSPO), welches in der äußeren Mito-
chondrienmembran von aktivierten Mikroglia überexprimiert wird [54]. TSPO zeigt in
PS2APP Mäusen einen altersabhängigen Anstieg der Mikrogliaaktivität [52].

Es liegen Hinweise aus Studien vor, dass eine erhöhte Mikrogliaaktivität für Veränderun-
gen des [^{18}F]FDG-PET Signals bei Patienten mit neurodegenerativen Erkrankungen und
Amyloid-Mausmodellen verantwortlich sein können [55]. Aufgrund der diskrepanten Er-
gebnisse bezüglich eines Hypo- beziehungsweise Hypermetabolismus im Glukosestoff-
wechsel, ist es notwendig, einen sensitiven Marker für Synapsenverlust zu entwickeln,
der unabhängig vom cerebralen Glukosemetabolismus fungiert. Der Untergang von Sy-
napsen wurde lange mit Immunhistochemie durch die Färbung von beispielsweise Sy-
naptophysin quantifiziert [56]. Die Möglichkeit der in vivo Darstellung des Synapsenver-
lusts durch PET Scans ermöglichte weitere Optionen. Hierzu existieren bereits auf [^{11}C]-
basierende (beispielsweise [^{11}C]UCB-A) und auf [^{18}F]-basierende ([^{18}F-UCB-J) [57]
SV2A-Liganden [58]. Der Radioligand [^{18}F]UCB-H präsentierte eine ähnliche cerebrale
Verteilung wie [^{11}C]UCB-J [59]. Humane Scans mit [^{18}F]UCB-H wiesen in Patienten mit
Morbus Alzheimer einen Synapsenverlust vor allem im Hippocampus auf [60], was die
weitere Untersuchung dieses Tracers für die Detektion von Neurodegeneration durch
Synapsenverlust interessant macht.

Die Annahme, dass Proteinaggregation und Neuroinflammation als frühe Ereignisse in
der Krankheitskaskade der Morbus Alzheimer auftreten, erhöht die Notwendigkeit der
Etablierung sensitiver Tracer, die spezifische Komponenten der Neuroinflammation
nachweisen können [61]. PET Studien mit [^{11}C]-markierten Radioliganden, die Deprenyl
als chemischen Leitstoff verwenden, wie z. B. [^{11}C]Deprenyl [62], [^{11}C]Deuterium-L-De-
prenyl [63] oder [^{11}C]SL25.1188 [64] veranschaulichten, dass die in vivo Bildgebung von
MAO-B den Nachweis einer signifikant höheren Bindung bei Patienten im Prodromalsta-
dium der Alzheimer Krankheit im Vergleich zu gesunden Kontrollen ermöglicht [65]. Auf-
grund der kurzen Halbwertszeit von Kohlenstoff (20,4 Minuten), steht die Untersuchung
von Fluor-basierten Tracern im Fokus künftiger Entwicklungen. [^{18}F]Fluordeprenyl zeigt

in Untersuchungen bei Affen ein ähnliches Bindungsmuster wie auf [^{11}C]-basierte Tracer [66]. Infolge der Deuterierung von Deprenyl, konnte die Einfangrate verringert und die Eliminierung aus Regionen mit geringer MAO-B Expression erhöht werden [67]. Daher hängt der in unserer Studie untersuchte neuartige Tracer [^{18}F]Fluordeprenyl-D2 ([^{18}F]F-DED) von der Konzentration der MAO-B-Expression ab, statt von einer Kombination aus MAO-B-Expression und Blutfluss. Aufgrund vielversprechender Ergebnisse, die die Bild-gebung von reaktiver Astrozytose im Menschen erforschten [68, 69], bestand unsere Zielsetzung darin, den Radioliganden [^{18}F]F-DED zu untersuchen und die Möglichkeit der Detektion von reaktiver Astrozytose zu evaluieren.

2.7   Zielsetzung der Dissertation

Die Relevanz von PET Biomarkern in der Diagnostik und in möglichen Therapieansätzen von neurodegenerativen Erkrankungen nimmt kontinuierlich zu. Die Untersuchung neu-rodegenerativer und neuroinflammatorischer Prozesse und damit die Etablierung spezi-fischer PET Tracer stellt einen relevanten Bestandteil dieser Entwicklung dar. Primäres Ziel dieser Dissertation ist die Untersuchung der Fähigkeit eines neuartigen MAO-B PET Liganden ([^{18}F]F-DED) zur Überwachung reaktiver Astrozytose beziehungsweise eines SV2A PET Liganden ([^{18}F]UCB-H) als präklinischer Biomarker für neurodegenerative Prozesse in transgenen Mausmodellen des Morbus Alzheimer.

Gegenstand aktueller Forschung ist die Untersuchung des zeitlichen und kausalen Zu-sammenhangs von Neuroinflammation mit anderen pathologischen Merkmalen der Alz-heimer Krankheit [49, 52, 70]. Es wird insbesondere untersucht, ob Neuroinflammation als primäres oder sekundäres Ereignis im Verlauf neurodegenerativer Erkrankungen auftritt und ob diese positive oder schädliche Auswirkungen auf den Hirnmetabolismus hat [15, 16]. In früheren PET Studien mit dem [^{11}C]-markierten MAO-B Inhibitor Deprenyl wurde bereits eine signifikant höhere Bindung in Gehirnen von Patienten im Prodromal-stadium der Alzheimer Krankheit im Vergleich zu gesunden Kontrollen festgestellt [65].

Der limitierende Faktor liegt bei Kohlenstoff jedoch in der kurzen Halbwertszeit von 20,4 Minuten. Als nützlichere Alternative für den klinischen Alltag wurden daraufhin Fluor-basierte Tracer untersucht, die ähnliche Bindungsmuster wie [^{11}C]-basierte Tracer aufwiesen und weniger vom Blutfluss abhängig waren [67]. Es zeigten sich erste vielsprechende Ergebnisse in humanen Studien mit Schwerpunkt der Untersuchung von reaktiver Astrozytose bei Patienten mit Morbus Alzheimer [68, 69]. Ziel unserer Studie war die in vivo Detektion von reaktiver Astrozytose in einem transgenen Mausmodell (PS2APP) für Morbus Alzheimer in verschiedenen Altersstufen unter der Verwendung des Radiotracers [^{18}F]F-DED. Es erfolgte eine histologische Validierung der präklinischen PET Ergebnisse durch GFAP-Immunfärbung. In einer Pilotstudie von Patienten mit verschiedenen neurodegenerativen Erkrankungen untersuchten wir die klinische Anwendbarkeit von [^{18}F]F-DED. Durch eine Korrelation von [^{18}F]F-DED mit den Radiotracern [^{18}F]GE-180 und [^{18}F]Florbetaben, strebten wir den Vergleich des zeitlichen und örtlichen Verlaufs der reaktiven Astrozytose mit anderen etablierten Biomarkern der Alzheimer Krankheit (Mikrogliaaktivierung und β-Amyloid Aggregation) an.

Bisher wurden neurodegenerative Prozesse durch humane PET Bildgebung vorwiegend durch den verringerten regionalen Glukosestoffwechsel und einer somit verringerten [^{18}F]FDG-Aufnahme demonstriert [71]. In präklinischen Studien existieren jedoch diskrepante Ergebnisse, die einen Hyper- versus Hypometabolismus in Mausmodellen für Alzheimer Krankheit diskutieren [51]. Der Hypermetabolismus wird auf den erhöhten Glukosestoffwechsel durch Neuroinflammation zurückgeführt [55, 72]. Die Unterschiede zwischen der Ergebnisse der humanen und präklinischen PET Bildgebung verstärken die Bedeutung der Identifizierung alternativer Biomarker zur regionalen Bewertung von Neurodegeneration. Frühere humane und präklinische Studien zeigten, dass die Abnahme der [^{18}F]UCB-H Bindung mit Synapsenverlust in typischen Hirnregionen bei Morbus Alzheimer übereinstimmen [60, 73]. In unserer Studie untersuchten wir die mögliche Verwendung von [^{18}F]UCB-H als alternativen Neurodegenerationsbiomarker durch verminderte Ausbildung von SV2A durch Synapsenverlust in einem transgenen β-Amyloid

Mausmodell (PS2APP) und einem transgenen Tau Mausmodell (P301S). Die in vivo Ergebnisse wurden histologisch durch Immunfärbung von SV2A validiert. Anschließend überprüften wir die Beziehung zwischen der Bindung von [^{18}F]UCB-H und [^{18}F]FDG in beiden Mausmodellen.

3. Zusammenfassung

Ziel dieser Arbeit war die Exploration neuer alternativer präklinischer Biomarker für neuroinflammatorische beziehungsweise neurodegenerative Prozesse in transgenen Mausmodellen. Wir untersuchten unter anderem die Fähigkeit des neuartigen Fluor-basierten MAO-B Liganden [18F]Flurodeprenyl-D2 ([18F]F-DED) reaktive Astrozytose durch MAO-B Expression im Vergleich von transgenen PS2APP Mäusen zu Wildtyp-Kontrollen zu detektieren. In einer Querschnittkohorte von 24 transgenen PS2APP Mäusen und 25 Wildtyp-Kontrollen in einer Altersspanne von 4,3 bis 21,0 Monaten wurden 60-minütige dynamische Scans mit [18F]F-DED, statische Scans mit [18F]GE-180 (TSPO) und [18F]Florbetaben (β-Amyloid) durchgeführt. Die Kohorten wurden in drei Altersgruppen (5 Monate, 13 Monate, 19 Monate) eingeteilt und als Zielregionen mit pathologisch erhöhter MAO-B Expression Hippocampus und Thalamus untersucht. Unsere erhobenen präklinischen Daten zeigten einen altersabhängigen Anstieg der [18F]F-DED Bindung im Hippocampus und im Thalamus innerhalb der transgenen PS2APP Mäuse und im Vergleich zu den Wildtyp-Kontrollen. Da MAO-B ubiquitär im Gehirn exprimiert wird [29, 31], evaluierten wir das Cerebellum als Pseudoreferenzregion mit geringer spezifischer Traceraufnahme. Wir stellten im Cerebellum, unabhängig von Alter und Genotyp, keinen signifikanten Unterschied im [18F]F-DED Signal fest. Die immunhistochemische Untersuchung des Kleinhirns bestätigte die Ergebnisse der PET Scans und ergab ebenfalls in dieser Region nur wenige GFAP-positive Zellen mit geringer MAO-B Expression. Weiterhin konnten wir in den PS2APP Mäusen einen altersabhängigen signifikanten Anstieg der [18F]F-DED Bindung im Hippocampus und im Thalamus detektieren, im Gegensatz zu den Wildtyp-Kontrollen. Auch im direkten Vergleich der 13-monatigen und 19-monatigen PS2APP Mäuse gegen Wildtyp-Kontrollen fanden wir einen signifikanten Anstieg der [18F]F-DED Bindung. Die semiquantitative Validation durch den Goldstandard der Immunhistochemie unterstützte die PET Daten durch erhöhte MAO-B und GFAP-Levels im Hippocampus und im Thalamus mit einer engen topologischen Assoziation zu β-Amyloid Plaques. Das [18F]F-DED Signal korrelierte stark mit der MAO-B Expression in

GFAP-positiven Astrozyten, was die Annahme bestärkt, dass dieser Tracer MAO-B positive reaktive Astrozytose nachweist. Um eine zeitliche Einordnung der neuroinflammatorischen Komponente durch reaktive Astrozytose in die pathophysiologische Kaskade der experimentellen Alzheimer Krankheit vorzunehmen, verglichen wir den Verlauf von reaktiver Astrozytose ([^{18}F]F-DED), aktivierter Mikroglia ([^{18}F]GE-180) und β-Amyloidose ([^{18}F]Florbetaben). Bestätigt durch die Immunhistochemie fanden wir heraus, dass Astrozytose als frühes Ereignis bereits bei fünf Monate alten PS2APP Mäusen auftritt und mittels PET messbar ist. PS2APP Mäuse exprimieren typischerweise erste β-Amyloid Plaques mit fünf bis sechs Monaten [42], mit einer engen Korrelation zur TSPO Expression im weiteren Altersverlauf [49]. Bei dem Vergleich der PET Signale zwischen MAO-B mit β-Amyloid und TSPO im Altersverlauf von PS2APP Mäusen fiel auf, dass [^{18}F]F-DED bereits bei jungen Mäusen ein erhöhtes Signal aufwies, jedoch ein Plateau ab dem mittleren Lebensalter erreichte. Dieses Ergebnis werteten wir als einen weiteren Indikator für einen frühzeitigen „Astrocyte burst" [17] in der Kaskade der Alzheimer Krankheit, was die Bildgebung von reaktiver Astrozytose als früher Alzheimer-Biomarker interessant machen könnte. Aufgrund der vielversprechenden präklinischen Daten wurden in einer Pilotstudie Patienten mit verschiedenen neurologischen Erkrankungen (Alzheimer Krankheit n=2; Parkinson-Erkrankung n=2; Multiple Systematrophie n=2; Autoimmunenzephalitis (n=1) Oligodendrogliom n=1) und eine gesunde Probandin ebenfalls mit [^{18}F]F-DED gescannt. Die [^{18}F]F-DED Bindung stimmte mit der erwarteten Topologie der reaktiven Astrozytose bei neurodegenerativen (MSA) und neuroinflammatorischen Erkrankungen überein. Eine Patientin mit einem Oligodendrogliom und eine gesunde Probandin wiesen eine [^{18}F]F-DED-Bindung auf, die der bekannten physiologischen MAO-B Expression im Gehirn entsprach. Die Topologie der MAO-B Expression und somit [^{18}F]F-DED Bindung könnte in Zukunft die Differentialdiagnostik neurologischer Erkrankungen vereinfachen. Diese ersten Ergebnisse sollten durch die Untersuchung einer größeren Kohorte und einer Längsschnittstudie bestätigt werden. Zusammenfassend ließ sich

feststellen, dass das Potenzial für die Detektion und Bewertung von reaktiver Astrozytose in transgenen Mausmodellen und bei Patienten mit neurodegenerativen beziehungsweise neuroinflammatorischen Erkrankungen durch die vivo Bildgebung mittels PET mit dem neuartigen MAO-B Tracer [^{18}F]F-DED hoch ist.

In unserer zweiten Studie untersuchten wir die Möglichkeit der Darstellung des fortschreitenden Verlusts der synaptischen Dichte beziehungsweise Funktion mithilfe von [^{18}F]UCB-H und [^{18}F]FDG. Hierzu wählten wir zwei transgene Mausmodelle (PS2APP (Amyloid Modell), P301S (Tau Modell)), die zwei typische pathologische Merkmale der Alzheimer Krankheit aufweisen. Insgesamt erhielten 29 PS2APP Mäuse (vier Altersgruppen), 20 P301S Mäuse (zwei Altersgruppen) und 12 Wildtypen-Kontrollen (eine Gruppe) im Alter zwischen 4,4 bis 19,8 Monaten einen dynamischen [^{18}F]UCB-H SV2A PET Scan (0-60 Minuten nach Injektion). Als Zielregion mit erniedrigter SV2A-Konzentration aufgrund Synapsenuntergangs untersuchten wir den Cortex, das Kleinhirn und den Hirnstamm. Zusätzlich führten wir statische Scans mit [^{18}F]FDG (Glukoseaufnahme) und [^{18}F]GE-180 (Mikrogliaaktiverung) durch und verglichen diese Biomarker mit der [^{18}F]UCB-H Bindung in den verschiedenen Altersstufen, um eine Einordnung der Interaktion zwischen der Entitäten Neurodegeneration durch Neuronenuntergang, Glukosemetabolismus und Neuroinflammation durch Mikrogliaaktiverung vorzunehmen. Die Validierung der PET Daten erfolgte durch immunhistochemische Färbung mit synaptischen Markern. Da SV2A ubiquitär im Gehirn exprimiert wird und somit keine pathologiefreie Region vorliegt, entschieden wir uns für die Validierung einer Pseudoreferenzregion. Nach weiteren Analysen wählten wir das obere Mittelhirn als Pseudoreferenzgewebe für semiquantitative Berechnungen der SV2A PET in weiteren Vergleichen. Die [^{18}F]UCB-H Bindung in den Zielregionen war in den acht Monate alten P301S Tau Mäusen im Vergleich zu den Wildtyp-Kontrollen verringert. Diese Beobachtung unterstreicht die Ergebnisse aus einer Studie, die neurotoxische Tau Aggregate in Zusammenhang mit Synapsenverlust in Alzheimer Modellen lieferte [69]. Der Prozess der Degeneration von Sy-

napsen geht vermutlich dem Auftreten der eigentlichen pathologischen Tau Fibrillen vo-
raus, deren Anhäufung mit dem Auftreten und Fortschreiten klinischer Symptome beim
Menschen korreliert [74, 75]. Da auch in unserer Studie bereits bei 4-monatigen P301S-
Mäusen ein [^{18}F]UCB-H Signalverlust beobachtet werden konnte, deutet dies darauf hin,
dass der Synapsenverlust eine eigenständige frühe Komponente der Neurodegenera-
tion ist.

Bei den PS2APP Amyloid-Mäusen (13 Monate, 19 Monate) war die SV2A Tracerauf-
nahme im Temporallappen und im Cerebellum im Vergleich zu den Wildtyp-Kontrollen
ebenfalls verringert. Im Hirnstamm wies dieses Mausmodell jedoch keine signifikant ver-
änderte Bindung von [^{18}F]UCB-H auf. Das stimmte mit der Topologie der β-Amyloid Ag-
gregation überein, die im Hirnstamm von PS2APP Mäusen nahezu nicht auftritt. Somit
existiert nicht nur ein Zusammenhang von Synapsenverlust mit dem Auftreten von Tau-
Pathologien, sondern auch von β-Amyloid Plaques. Unsere Beobachtungen passen gut
zu Humanstudien, in denen eine signifikant verringerte [^{18}F]UCB-H und [^{11}C]UCB-J Tra-
ceraufnahme im mittleren Temporallappen und Hippocampus von Patienten mit Alzhei-
mer Krankheit beobachtet wurde [60, 76]. Die immunhistochemische Färbung der Maus-
gehirngewebe bestätigte die Erkenntnisse der PET Daten in den Mausmodellen.

Im Rahmen des Multi-Tracer-Ansatzes verglichen wir abschließend den regionalen Glu-
kosestoffwechsel in den Zielregionen mit der [^{18}F]UCB-H Aufnahme beziehungsweise
der Mikrogliaaktivierung. Korrelationsanalysen ergaben einen signifikant negativen Zu-
sammenhang zwischen [^{18}F]UCB-H und [^{18}F]FDG im PS2APP Mausmodell, sprich der
Synapsendichte und dem Glukosemetabolismus. Weitere explorative Analysen zeigten
jedoch eine positive Korrelation zwischen [^{18}F]FDG und [^{18}F]GE-180 (Mikrogliaaktivität)
in dieser Kohorte. Diese Ergebnisse unterstrichen die Annahme, dass eine mögliche
Ursache für den erhöhten Glukosestoffwechsel die Co-Lokalisation von aktivierter
Mikroglia zu degenerierten Synapsen sein könnte und der Glukosemetabolismus somit
durch die Neuroinflammation beeinflusst wird [55]. In einer kürzlich veröffentlichten Un-
tersuchung von Patienten mit Chorea Huntington wurde festgestellt, dass ein größerer

Synapsenverlust als Hypometabolismus beobachtet werden konnte, was darauf hindeutet, dass [^{18}F]FDG möglicherweise nicht sensitiv genug für die Erkennung früher Veränderungen in der Pathophysiologie der Erkrankung ist [77]. Diese Erkenntnis wird in weiteren Studien genauer beleuchtet werden müssen. Für die Einordnung des zeitlichen und räumlichen Zusammenhangs zwischen Glukosemetabolismus, Synapsenverlust und Neurodegeneration bedarf es weiterer Studien. Die in vivo Bildgebung mit [^{18}F]UCB-H detektiert zuverlässig den voranschreitenden Synapsenverlust in zwei transgenen Mausmodellen mit Pathologien der Alzheimer Krankheit und könnte somit einen robusten Biomarker für die präklinische Alzheimerforschung darstellen.

4.   Abstract (English)

The aim of this work was to explore novel alternative preclinical biomarkers for neu-roinflammatory or neurodegenerative processes in transgenic mouse models. Among others, we investigated the ability of the novel fluorine-based MAO-B ligand [^{18}F]fluro-deprenyl-D2 ([^{18}F]F-DED) to detect reactive astrocytosis by MAO-B expression in comparison of PS2APP transgenic mice to wild-type controls. In a cross-sectional cohort of 24 PS2APP transgenic mice and 25 wild-type controls ranging in age from 4.3 to 21.0 months, 60-minute dynamic scans were performed with [^{18}F]F-DED and static scans with [^{18}F]GE-180 (TSPO), and [^{18}F]florbetaben (β-amyloid). Cohorts were divided into three age groups (5 months, 13 months, 19 months) and the target regions hippocampus and thalamus were examined. Our collected preclinical data showed an age-dependent increase in [^{18}F]F-DED binding in the hippocampus and the thalamus within PS2APP transgenic mice and compared with wild-type controls. Since MAO-B is ubiquitously expressed in the brain [29, 31], we evaluated the cerebellum as a pseudo-reference region with low specific tracer uptake. We found no significant differences in the cerebellum, independent of age and genotype. Immunohistochemical analysis of the cerebellum confirmed the PET data and also revealed few GFAP-positive cells with low MAO-B expression. Furthermore, we detected an age-dependent significant increase in [^{18}F]F-DED binding in the hippocampus and the thalamus in PS2APP mice, in contrast to wild-type controls. We also found a significant increase in [^{18}F]F-DED binding in a direct comparison of 13-month and 19-month PS2APP mice versus wild-type controls. Semiquantitative validation by the gold standard of immunohistochemistry supported the PET data through increased MAO-B and GFAP levels in the hippocampus and the thalamus with a close topological association to β-amyloid plaques. The [^{18}F]F-DED signal correlated strongly with MAO-B expression in GFAP-positive astrocytes, reinforcing the notion that this tracer detects MAO-B-positive reactive astrocytosis. To provide a temporal classification of reactive astrocytosis in the pathophysiological cascade of experimental AD, we compared the progression of reactive astrocytosis ([^{18}F]F-DED), activated microglia

([^{18}F]GE-180), and β-amyloidosis ([^{18}F]Florbetaben). Confirmed by immunohistochemical analysis, we discovered that astrocytosis occurs as an early event in five month old PS2APP mice and is measurable by PET. PS2APP mice typically express first β-amyloid plaques at five to six months [42], with a close correlation to TSPO expression with increasing age [49]. When comparing PET signals between MAO-B with β-amyloid and TSPO in the age progression of PS2APP mice, it was notable that [^{18}F]F-DED already showed an increased signal in young mice, but reached a plateau from middle age. We evaluated this result as another indicator of an early "astrocyte burst" [17] in the AD cascade, which could make imaging of reactive astrocytosis interesting as an early AD biomarker. Based on the promising preclinical data, patients with different neurological diseases (AD n=2; Parkinson's disease n=2; multiple system atrophy n=2; autoimmune encephalitis (n=1) oligodendroglioma n=1) and one healthy control were also scanned with [^{18}F]F-DED in a pilot study. The [^{18}F]F-DED binding was consistent with the expected topology of reactive astrocytosis in neurodegenerative (MSA) and neuroinflammatory diseases. One patient with oligodendroglioma and one healthy control exhibited [^{18}F]F-DED binding consistent with known physiological MAO-B expression in the brain. The topology of MAO-B expression and thus [^{18}F]F-DED binding may facilitate differential diagnosis of neurological diseases in the future. These initial results should be confirmed by studying a larger cohort in a longitudinal study. In conclusion, in vivo imaging by PET with the novel MAO-B tracer [^{18}F]F-DED indicates a potential for assessment of reactive astrogliosis in AD mouse models and patients with neurodegenerative and neuroinflammatory diseases

In our second study, we investigated the possibility of visualizing the progressive loss of synaptic density and function, using [^{18}F]UCB-H and [^{18}F]FDG. For this purpose, we chose two transgenic mouse models (PS2APP (amyloid model), P301S (tau model)) that exhibit two typical pathologies of AD. A total of 29 PS2APP (four age groups), 20 P301S (two age groups), and 12 wild-type controls (one group) received dynamic [^{18}F]UCB-H SV2A-PET scan (0-60 minutes after injection) at ages ranging from 4.4 to 19.8 months.

We examined the cortex, cerebellum, and brainstem as target regions. In addition, we performed static scans with [18F]FDG (glucose uptake) and [18F]GE-180 (microglial activation) and compared these biomarkers with [18F]UCB-H binding at different ages. Validation of PET data was performed by immunohistochemical staining with synaptic markers. Because SV2A is ubiquitously expressed in the brain, we chose to validate a pseudo reference region. After further analysis, we chose the upper midbrain as a pseudo reference region for semiquantitative calculations of SV2A PET in further comparisons. The [18F]UCB-H binding in the target regions was decreased in the eight month old P301S tau mice compared with the wild-type controls. This observation underscores the results from a study that showed an association between neurotoxic tau aggregates and synapse loss in AD models [69]. The process of degeneration of synapses presumably precedes the appearance of the actual pathological tau fibrils. The accumulation of tau fibrils correlates with the onset and progression of clinical symptoms in humans [74, 75]. Since [18F]UCB-H signal loss was also observed in four month old P301S mice in our study, this suggests that synapse loss is an independent early component of neurodegeneration.

In the PS2APP amyloid mice (13 months, 19 months), SV2A tracer uptake was also decreased in the temporal lobe and cerebellum compared with wild-type controls. However, in the brainstem, this mouse model did not show significantly altered binding of [18F]UCB-H. This was consistent with the topology of β-amyloid aggregation being almost absent in the brainstem of PS2APP mice. Thus, a correlation exists not only of synapse loss with the occurrence of tau pathologies but also of β-amyloid plaques. Our observations fit well with human studies in which significantly decreased [18F]UCB-H and [11C]UCB-J tracer uptake was observed in the middle temporal lobe and hippocampus of patients with AD [60, 76]. Immunohistochemical staining of mouse brain tissues confirmed the findings of PET data in the mouse models.

Finally, using a multi-tracer approach, we compared regional glucose metabolism in the target regions with [18F]UCB-H uptake and microglial activation, respectively. Correlation

analyses revealed a significant negative correlation between [^{18}F]UCB-H (synapse density) and [^{18}F]FDG (glucose metabolism) in the PS2APP mouse model. However, further exploratory analyses revealed a positive correlation between [^{18}F]FDG and [^{18}F]GE-180 (microglial activity) in this cohort. These results supported the assumption that a possible cause of the increased glucose metabolism could be the co-localization of activated microglia to degenerated synapses and that glucose metabolism is thus influenced by neuroinflammation [55]. A recent study examining patients with Huntington's disease showed that greater synapse loss than hypometabolism, suggesting that [^{18}F]FDG may not be sensitive enough for detecting early changes in the pathophysiology of the disease [77]. This findings will need to be further elucidated in studies. Additionally there is a need to classify the temporal and spatial relationship between glucose metabolism, synapse loss, and neurodegeneration. In conclusion, in vivo imaging with [^{18}F]UCB-H reliably detects advancing synapse loss in two transgenic mouse models with Alzheimer's disease pathologies and thus could provide a robust biomarker for preclinical Alzheimer's disease research.

5.   Publikation I

Journal of Neuroinflammation

RESEARCH   **Open Access**

[¹⁸F]F-DED PET imaging of reactive astrogliosis in neurodegenerative diseases: preclinical proof of concept and first-in-human data

Anna Ballweg[1†], Carolin Klaus[2†], Letizia Vogler[1†], Sabrina Katzdobler[3], Karin Wind[1,2], Artem Zatcepin[1,2], Sibylle I. Ziegler[1], Birkan Secgin[1], Florian Eckenweber[1], Bernd Bohr[1], Alexander Bernhardt[3], Urban Fietzek[3], Boris-Stephan Rauchmann[5,6], Sophia Stoecklein[5], Stefanie Quach[4], Leonie Beyer[1], Maximilian Scheifele[1], Marcel Simmet[1], Emanuel Joseph[1], Simon Lindner[1], Isabella Berg[1], Norman Koglin[7], Andre Mueller[7], Andrew W. Stephens[7], Peter Bartenstein[1,8], Joerg C. Tonn[4,9], Nathalie L. Albert[1,8], Tania Kümpfel[10], Martin Kerschensteiner[8,10,11], Robert Perneczky[2,6,8,12,13], Johannes Levin[2,3,8], Lars Paeger[2], Jochen Herms[2,8,14] and Matthias Brendel[1,2,8*]

Abstract

Objectives Reactive gliosis is a common pathological hallmark of CNS pathology resulting from neurodegeneration and neuroinflammation. In this study we investigate the capability of a novel monoamine oxidase B (MAO-B) PET ligand to monitor reactive astrogliosis in a transgenic mouse model of Alzheimer`s disease (AD). Furthermore, we performed a pilot study in patients with a range of neurodegenerative and neuroinflammatory conditions.

Methods A cross-sectional cohort of 24 transgenic (PS2APP) and 25 wild-type mice (age range: 4.3–21.0 months) underwent 60 min dynamic [¹⁸F]fluorodeprenyl-D2 ([¹⁸F]F-DED), static 18 kDa translocator protein (TSPO, [¹⁸F]GE-180) and β-amyloid ([¹⁸F]florbetaben) PET imaging. Quantification was performed via image derived input function (IDIF, cardiac input), simplified non-invasive reference tissue modelling (SRTM2, DVR) and late-phase standardized uptake value ratios (SUVr). Immunohistochemical (IHC) analyses of glial fibrillary acidic protein (GFAP) and MAO-B were performed to validate PET imaging by gold standard assessments. Patients belonging to the Alzheimer's disease continuum (AD, $n = 2$), Parkinson's disease (PD, $n = 2$), multiple system atrophy (MSA, $n = 2$), autoimmune encephalitis ($n = 1$), oligodendroglioma ($n = 1$) and one healthy control underwent 60 min dynamic [¹⁸F]F-DED PET and the data were analyzed using equivalent quantification strategies.

Results We selected the cerebellum as a pseudo-reference region based on the immunohistochemical comparison of age-matched PS2APP and WT mice. Subsequent PET imaging revealed that PS2APP mice showed elevated hippocampal and thalamic [¹⁸F]F-DED DVR when compared to age-matched WT mice at 5 months (thalamus: $+4.3\%$; $p = 0.048$), 13 months (hippocampus: $+7.6\%$, $p = 0.022$) and 19 months (hippocampus: $+12.3\%$, $p < 0.0001$;

†A. Ballweg, C. Klaus and L. Vogler contributed equally as first authors.

*Correspondence:
Matthias Brendel
matthias.brendel@med.uni-muenchen.de
Full list of author information is available at the end of the article

thalamus: $+15.2\%$, $p < 0.0001$). Specific [18F]F-DED DVR increases of PS2APP mice occurred earlier when compared to signal alterations in TSPO and β-amyloid PET and [18F]F-DED DVR correlated with quantitative immunohistochemistry (hippocampus: $R = 0.720$, $p < 0.001$; thalamus: $R = 0.727$, $p = 0.002$). Preliminary experience in patients showed [18F]F-DED V_T and SUVr patterns, matching the expected topology of reactive astrogliosis in neurodegenerative (MSA) and neuroinflammatory conditions, whereas the patient with oligodendroglioma and the healthy control indicated [18F]F-DED binding following the known physiological MAO-B expression in brain.

Conclusions [18F]F-DED PET imaging is a promising approach to assess reactive astrogliosis in AD mouse models and patients with neurological diseases.

Keywords MAO-B, PET, Astrocytes, Deprenyl

Introduction

In recent years, a growing body of research has been dedicated to deciphering the involvement of non-neuronal cells in neurodegenerative diseases [1–3]. In this regard, Alzheimer's disease (AD), as the most common cause of dementia is characterized by the "A-T-N" co-occurrence of beta-amyloid, hyperphosphorylated tau-fibrils, and neuronal loss [4, 5], but compelling evidence further suggests that neuroinflammation is another major hallmark of the disease. Dysregulated microglia and astroglia significantly contribute to the progression of AD and various other neurodegenerative diseases as well, often even predating the onset of cognitive decline and increase of other biomarkers [6–8]. Even though the temporal and causal relationship between these two glial entities and their various neuroprotective and neurotoxic subtypes remain to be further elucidated, in vivo detection of these cell types holds the potential to diagnose and intervene in the earliest disease stages. Astrocytes in particular have been proposed as an additional, inflammatory biomarker within the A–T–N scheme (I+ or I-) to further improve the phenotyping and staging of the disease [9]. In response to different stimuli, this cell type acquires a reactive state by changing its function, morphology and gene expression profile [10]. As a result, many proteins are upregulated, some of which have been introduced as semi-specific biomarkers for astrogliosis. For example, increases of glial fibrillary acidic protein (GFAP) in various biofluids—albeit heterogeneously expressed by astrocytes—have been associated with both traumatic and neurodegenerative brain diseases as well as in healthy aging brains due to astrocyte hypertrophy and proliferation [11, 12]. Consequently, GFAP is currently used as a frequent marker of reactive astrocytes in brain tissue, blood and cerebrospinal fluid [10]. However, to date, no small molecular compounds have been established that selectively bind to GFAP when using more precise in-vivo imaging techniques, such as positron emission tomography (PET) [13]. It is for this reason that multiple radiotracers have so far targeted another semi-specific surrogate for reactive astrocytes, namely, monoamine

oxidase B (MAO-B) [13]. This enzyme is predominantly located in the outer mitochondrial membrane of astrocytes and to a lesser extent in other cell types, such as serotonergic neurons, oligodendrocytes and microglia [13, 14]. Initial PET studies with the [11C] labeled MAO-B inhibitor Deprenyl have shown significantly higher binding in prodromal AD patients when compared to healthy controls [15]. However, the short half-life of [11C] (20.4 min) limits the use of these tracers to centers with on-site cyclotrons [16]. Therefore, [18F]fluorodeprenyl has recently been developed as a more practical alternative, showing comparable binding patterns to [11C]-based tracers while also reducing the trapping rate and increasing elimination from regions with low MAO-B expression due to deuteration (i.e., [11C]Deprenyl-D2). As such, [18F]fluorodeprenyl-D2 ([18F]F-DED) is dependent on MAO-B concentrations rather than a combination of MAO-B and blood flow [16]. Given promising first-in-human results that were recently described for imaging of reactive astrogliosis in AD [17, 18], we sought to target astrogliosis in-vivo in a transgenic mouse model of AD at various ages by means of [18F]F-DED and to provide histological validation using GFAP immunostaining. We further aimed to evaluate the clinical feasibility of [18F]F-DED in a pilot cohort of patients with various neurological diseases. To determine the temporal and spatial relationship with other established biomarkers of AD, we also aimed to directly compare the time course of astrogliosis in transgenic and wild-type mice with microgliosis and beta-amyloid burden using [18F]GE-180 and [18F]florbetaben, respectively.

Materials and methods

Radiochemistry

[18F]F-DED was synthesized on a Trasis AllinOne (Ans, Belgium) automated synthesis unit (ASU) consisting of 3 series-connected manifolds with a total of 18 valves. The manifolds were clamped into the correct position at the module. All reagents and materials were assembled on the pre-defined positions of the manifold (position 2: eluent, position 5: SAX cartridge, position 8:

precursor solution, position 11: water bag, position 12: PBS bag, position 13: SPE cartridge, position 15: EtOH, position 16: HPLC solvent). The software prompts were followed, and manual intervention was necessary only during HPLC purification. No carrier added [18F]fluoride was produced via $^{18}O(p, n)^{18}F$ reaction by proton irradiation of ^{18}O-enriched water and delivered to the activity inlet reservoir. The activity was then trapped on a Waters QMA Plus Light Carb cartridge and eluted into the reactor using the eluent solution (5 mg K_{222}, 7.24 µL 1 M K_2CO_3, 300 µL H_2O and 300 µL MeCN). After azeotropic drying, the precursor solution (2 mg Cl-Deprenyl-D2 in 600 µL MeCN) was transferred to the reactor, and the reaction mixture was heated at 120 °C for 20 min. The reaction mixture was quenched with HPLC solvent (4 mL) and purified via semi-preparative HPLC (Inertsil ODS-4 C18, 250×10 mm, 5 µm, 100 Å; isocratic elution with 60% (v/v) 5 mM NaOAc (pH 4)/40% (v/v) EtOH; flow: 5 ml/min; UV detection: 254 nm). The product peak was collected, diluted with water (48 mL) and passed through a Waters Oasis Plus Light HLB cartridge pre-conditioned with 10 ml EtOH and 10 ml water. The cartridge was rinsed with water (10 mL) and the radiolabeled product was eluted with 1 mL EtOH and diluted with phosphate buffered saline (11 mL). The formulated product solution was transferred to a dispenser and filtered through a Merck Cathivex-GV sterile filter. The product was obtained in a RCY of $15 \pm 3.0\%$ n.d.c. ($n = 16$) and a RCP of $98 \pm 1.2\%$ ($n = 16$). Specific activity was 267 ± 120 GBq/µmol ($n = 7$).

Preclinical study overview

All preclinical experiments were performed in compliance with the National Guidelines for Animal Protection, Germany, with approval of the local animal care committee of the Government of Upper Bavaria and overseen by a veterinarian. The preclinical study was conducted in a cross-sectional design. Small-animal PET scans were performed using the three tracers [18F]F-DED (MAO-B), [18F]GE-180 (TSPO) and [18F]florbetaben (β-amyloid) in male wild-type and transgenic mice (PS2APP) using young (5–6 months), intermediate (11–13 months), and aged (18–20 months) animals (Table 1). Every animal underwent dynamic [18F]F-DED (0–60 min p.i.) PET scans and static PET scans using [18F]GE-180 (60–90 min p.i.) and [18F]florbetaben (30–60 min p.i.). Wild-type controls for [18F]GE-180 and [18F]florbetaben were obtained from the large standardized in-house database [19]. After the final PET session, mice were perfused using phosphate-buffered saline while deeply anaesthetized. The brain was fixed overnight with paraformaldehyde 4% before immunohistochemical analysis.

Animals

Animals were housed in a temperature- and humidity-controlled environment with a 12-h light–dark cycle, with free access to food (Ssniff, Soest, Germany) and water. We used 25 male wild-type C57Bl/6 (WT) and 24 male PS2APP transgenic mice (TG) in this investigation. The transgenic B6.PS2APP (line B6.152H) is homozygous for both the human presenilin (PS) 2, N141I mutation and the human amyloid precursor protein (APP) K670N, M671L mutation. The APP and PS2 transgenes are driven by mouse Thy-1 and mouse prion promoters, respectively. This line had been created by co-injection of both transgenes into C57Bl/6 zygotes [20]. Homozygous B6.PS2APP (PS2APP) mice show first appearance of plaques in the cortex and hippocampus at 5–6 months of age [21].

Small-animal PET data acquisition, reconstruction and coregistration

All PET procedures followed an established standardized protocol for acquisition, reconstruction, and post-processing [22–24]. In brief, [18F]F-DED (13.0 ± 2.5 MBq) with an emission window of 0–60 min p.i. was used to

Table 1 Overview on animals and key results of the cross-sectional preclinical study

Mouse model	Age (mo)	[18F]F-DED small animal PET (n)	[18F]F-DED small animal PET (DVR_{HIP})	[18F]F-DED small animal PET (DVR_{THA})	[18F]GE-180 small animal PET (n)	[18F]florbetaben small animal PET (n)
PS2APP	5.9	7	1.09 ± 0.07	$1.17 \pm 0.06*$	7	6
	13.4	9	$1.11 \pm 0.05*$	1.18 ± 0.07	6	8
	19.5	8	$1.20 \pm 0.05**$	$1.25 \pm 0.07**$	5	8
Wild type	5.1	11	1.07 ± 0.03	1.09 ± 0.06		
	11.2	6	1.03 ± 0.07	1.08 ± 0.12		
	18.6	8	1.06 ± 0.06	1.08 ± 0.03		

Small-animal PET DVRs are shown for [18F]F-DED

Significant differences in PS2APP mice vs. age-matched wild-type controls are indicated by *$p < 0.5$; **$p < 0.001$

analyze MAO-B expression, [^{18}F]GE-180 TSPO–PET (14.2±2.6 MBq) with an emission window of 60–90 min p.i. was used to measure cerebral TSPO expression, and [^{18}F]florbetaben β-amyloid-PET (11.1±1.7 MBq) with an emission window of 30–60 min p.i. was used for assessment of fibrillary cerebral amyloidosis. Existing in-house normal cohorts of wild-type mice at matching ages were used for TSPO- and β-amyloid-PET [25, 26]. All analyses were performed by PMOD (V3.5, PMOD technologies, Basel, Switzerland). Spatial coregistration was performed with tracer specific templates as previously described [27].

Small-animal PET data analyses

Hippocampus (24 mm^3) and thalamus (27 mm^3) were defined as target regions of interests and the cerebellum (56 mm^3) was defined as a potential reference region based on the Mirrione atlas [28].

[^{18}F]F-DED volume-of-distribution (V_T) images were calculated with an image derived input function (IDIF) [29] using the methodology described by Logan et al. implemented in PMOD [30]. The plasma curve was obtained from a standardized VOI (3 mm sphere) placed in the left heart (including myocardium and ventricle). A maximum error of 10% and a V_T threshold of 0 were selected for modelling of the full dynamic imaging data. Cerebellar V_T were compared between young and aged mice from both genotypes to evaluate the suitability of the cerebellum as proposed pseudo-reference tissue. Distribution volume ratios (DVRs) of [^{18}F]F-DED PET were subsequently calculated by simplified reference tissue 2 (SRTM2) modelling in PMOD, using the cerebellum as a reference tissue. DVRs served as the primary endpoint of [^{18}F]F-DED PET analyses. SUV ratios (SUVR) of the 30–60 min p.i. time window were calculated with the cerebellum as a reference tissue to explore the suitability of simplified late-static imaging. TSPO- and β-amyloid PET were analogously quantified as SUVR with the same cerebellar reference tissue [23, 31].

Immunohistochemistry

A total of 19 PS2APP mice and 10 wild-type mice, each divided into three age-related groups, were used for immunohistochemistry (wild-type mice: 5 months $n=3$, 13 months $n=4$, 19 months $n=3$; PS2APP mice: 5 months $n=6$, 13 months $n=10$, 19 months $n=3$). 50 μm thick slices were cut in a sagittal plane using a vibratome (VT1200S, Leica Biosystems). Four slices per animal, between the lateral coordinates 2.16 mm and 0.84 mm, were collected, containing the regions of interest: hippocampus, thalamus and cerebellum. Slices were treated with blocking solution (3% normal goat serum and 2% BSA in 0.3%Triton and PBS to a total volume of at least 200 μl per well/slice) for 3 h at RT. The following

primary antibodies were used: rabbit anti-GFAP 1:500 (180063, Invitrogen by Thermo Fisher Scientific, California, USA), chicken anti-GFAP 1:500 (ab5541, Merck Millipore, Darmstadt, Germany), mouse anti-MAO-B 1:800 (D-6, sc-515354, Santa Cruz Biotechnology, Texas, USA), guinea pig anti-Iba1 1:500 (234004, Synaptic Systems, Göttingen, Germany), mouse anti-β-amyloid 1:500 (NAB228, sc-32277, Santa Cruz Biotechnology, Texas, USA) and goat anti-TPH2 1:500 (ab121013, Abcam, Cambridge, UK), diluted in blocking solution (1% normal goat serum and 1% BSA in 0.3% Triton and PBS to a total volume of at least 200 μl per well/slice), applied to the slices and incubated over-night at 4 °C on a horizontal shaker. Slices were washed three times, each 10 min with PBS to remove the spillover of the primary antibodies. Secondary antibodies, goat anti-rabbit Alexa Flour 488 (1:500), goat anti-chicken Alexa Fluor 488 (1:500), goat anti-guinea pig Alexa Fluor 555 (1:500), goat anti-mouse Alexa Fluor 647 (1:500) and donkey anti-goat Alexa Fluor 568 (1:500) diluted in blocking solution, were applied. Slices were incubated for 2 h at RT on a horizontal shaker, protected from light. Slices were washed 3 × 10 min with PBS and subsequently incubated in Sudan black for 15 min on a horizontal shaker at RT to reduce autofluorescence. After 3 × 10 min washing with PBS, slices were mounted and cover slipped with fluorescence mounting medium (Dako, Santa Clara, USA). Three-dimensional images were acquired with an Apotome microscope (Zeiss Oberkochen, Germany) using a 10×, 20× and 60× objective. The analysis programs Zeiss blue and ImageJ were used for quantification.

To analyze the MAO-B signal in GFAP positive astrocytes, two slices per animal were selected. From each of these slices, we acquired z-stack images (15 μm) in the hippocampus (CA1/Subiculum) and thalamus with a 60× objective. Each 4 cells per area got quantified as the perceptual area of MAO-B in GFAP-positive astrocytes. To this end, we created a mask of the GFAP-positive astrocyte and transferred it onto the MAO-B image. After a local brightness/contrast adjustment, we set a fixed threshold and used the "analyze particle" function to calculate the MAO-B area (%) inside the mask of the GFAP-positive astrocyte.

Plaque load (Aβ), astrogliosis (GFAP) and microgliosis (Iba1) were analyzed in the hippocampus/subiculum of 3 slices per animal by quantifying the total area (%) of each signal of an orthogonal projection of a 10 μm z-stack.

Human PET imaging

Eight patients belonging to the AD continuum ($n=2$), Parkinson's disease ($n=2$), multiple system atrophy (MSA, $n=2$), autoimmune encephalitis ($n=1$), oligodendroglioma ($n=1$), and one healthy control received [^{18}F]

F-DED PET in a clinical setting at a tertiary center after giving written informed consent at the Dept. of Nuclear Medicine, LMU University Hospital. Patient characteristics are provided in Table 2. Toxicology was assessed in rats prior to the human study, indicating a No Observed Adverse Effect Level (NOAEL) of 33.33 µg/kg. The maximum injected mass was determined at 3.22 µg [^{18}F]F-DED for a 60 kg patient and a 100-fold safety margin. The A–T–N status of patients belonging to the AD continuum was determined using PET (A: [^{18}F]flutemetamol late-phase 90–110 min p.i.; T: [^{18}F]PI-2620 30–60 min p.i.; N: either [^{18}F]flutemetamol early phase 0–10 min p.i. or [^{18}F] FDG 30–50 min p.i.) or CSF (A: A$\beta_{42/40}$ ratio; T: p-Tau).

Caffeine consumption was prohibited starting 3 h before tracer injection. No patients with active smoking history were examined. After ldCT for attenuation correction, 177 ± 35 MBq [^{18}F]F-DED were injected i.v. as a slow bolus injection (~ 10 s) followed by dynamic 60-min emission recording on harmonized Siemens PET/CT systems (Biograph 64, Biograph mCT). OSEM3D reconstruction was performed as previously described [32]. Data analysis was approved by the local ethics committee of the medical faculty of the LMU Munich (Application Number: 21-0721). Calculation of [^{18}F]F-DED PET volume of distribution (V$_T$) was performed using the average carotid tracer uptake as image-derived input function (IDIF) for non-invasive kinetic modeling. For proper quantitative representation of the tracer uptake in the brain, we calculated and compared four different kinetic models, since reversible and irreversible components of [^{18}F] F-DED were not investigated in the human brain yet: a one-tissue compartment model (Logan plot), a one-tissue compartment model with two rate constants (1TC2k) as well as two-tissue compartment models with either three (2TC3k) or four rate constants (2TC4k) depending on the reversibility of the binding behaviour. We then calculated *F* tests to statistically compare the simplest model to the more complex models in each brain region. Selected target regions of the Hammers atlas consisted of the brainstem, the cerebellar white matter, a cortical composite, the mesial temporal lobe and the putamen. Spatial normalization and brain region definition was performed using PMOD's PNEURO tool with existing MRI T1 MPRAGE sequences. Analysis of PET imaging data was performed visually and by volume-of-interest-(VOI)-based analysis of V$_T$. In addition, static 30–60 min SUVr images and regional SUVr were evaluated as simplified quantification using a parietal lobe white matter reference tissue (predefined by the Hammers atlas) to assess relative signal changes in the investigated subjects. Time-activity SUV curves were inspected qualitatively.
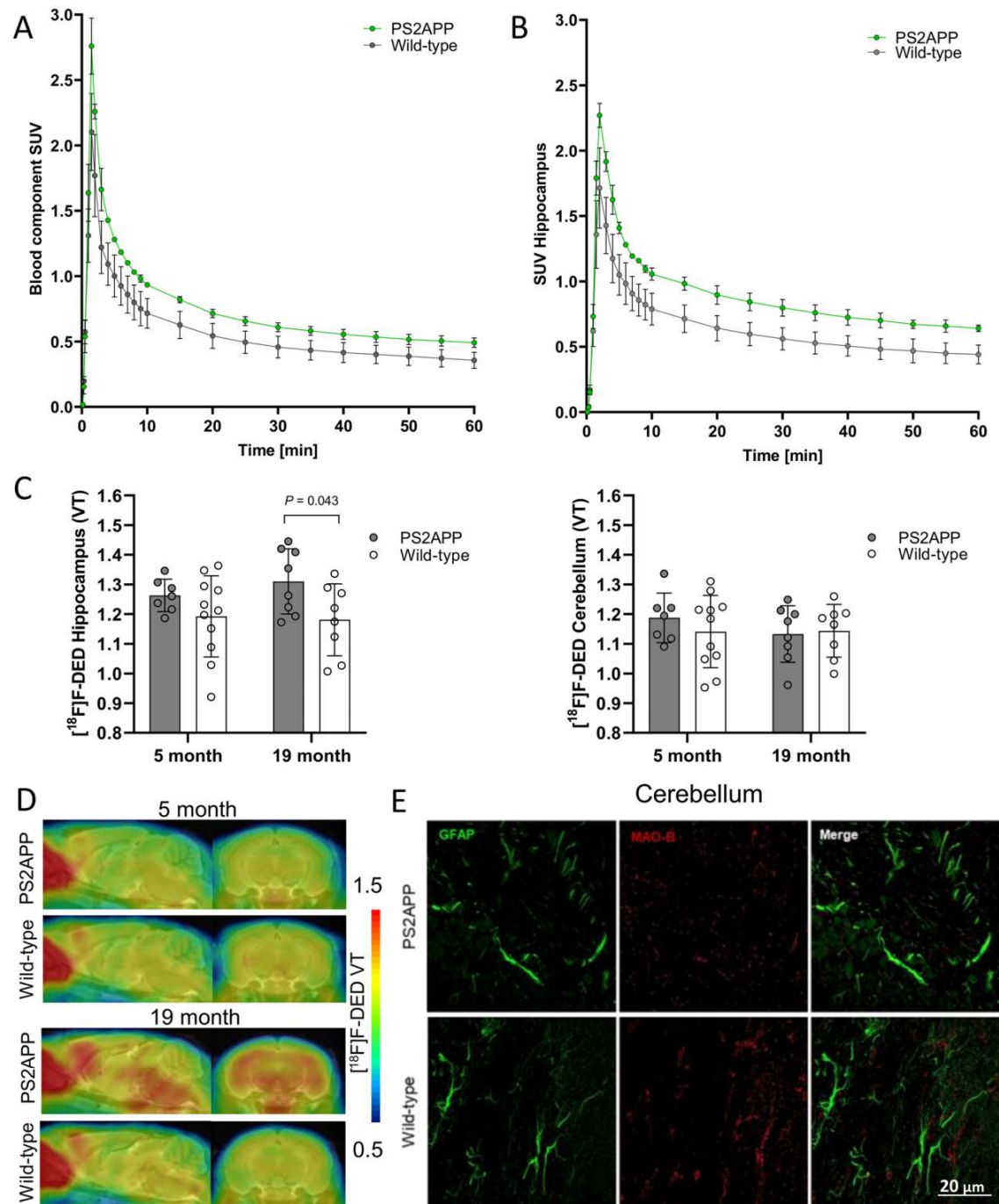
Statistics

Group comparisons of VOI-based small-animal PET results or immunohistochemical quantification were assessed by one-way ANOVA with Tukey post-hoc correction using Graph Pad Prism (V8). Two-way ANOVA was used when two categorical variables were included in the analysis. For correlation analyses, Pearson's coefficient of correlation was calculated after controlling for normal distribution. Immunohistochemistry data were expressed as mean $\pm$ standard deviation. A threshold of $P < 0.05$ was considered to be significant for rejection of the null hypothesis.
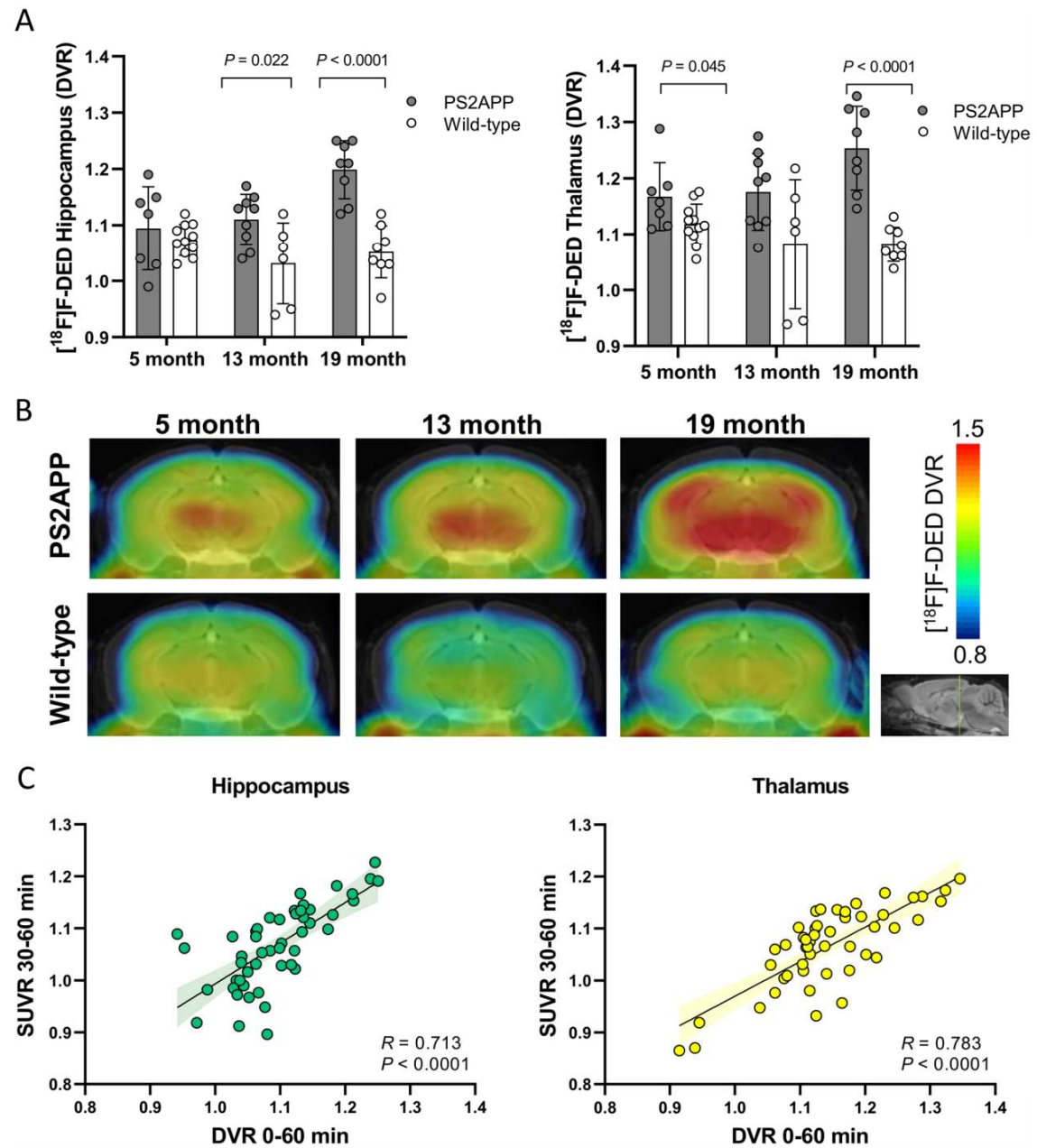
Table 2 Overview of the demographics of human subjects included in this study

Diagnosis	Age (years)	Gender	Disease duration (years)	[^{18}F]F-DED dose (MBq)	Height (cm)	Body weight (kg)	Disease severity indices
MCI Alzheimer's pathologic change (A+T − N −)	69	M	0.5	190	170	69	MMSE: 26/30
AD-Dementia (A+T+N+)	66	F	2.0	169	163	52	MMSE: 21/30
PD (1.7 y disease duration)	55	F	1.7	180	165	62	UPDRS III: 14; MoCA: 28/30
PD (4.8 y disease duration)	56	F	4.8	149	167	64	UPDRS III: 18; H&Y: 1; MoCA: 29/30
Autoimmune encephalitis	53	M	25.2	217	182	72	–
MSA-C	56	M	2.1	162	190	84	UPDRS III: 30; H&Y: 2; MoCA: 28/30
MSA-P	65	M	4.2	134	173	96	UPDRS III: 19; MoCA: 29/30
ODG	60	F	1.3	244	160	61	–
Healthy control	28	F	–	150	170	64	–

MCI mild cognitive impairment; *AD* Alzheimer's disease, *A* β-amyloid; *T* tau; *N* neurodegeneration; *PD* Parkinson's disease; *MSA* Multiple system atrophy; *C* cerebellar subtype; *P* parkinsonian subtype; *ODG* Oligodendroglioma; *MMSE* mini mental state examination; *MoCA* Montreal Cognitive Assessment; *UPDRS* Unified Parkinson's Disease Rating Scale; *H&Y* Hoehn and Yahr scale

Fig. 1 A, **B** [^{18}F]F-DED cardiac blood input curves and hippocampal time-activity-curves in comparison of PS2APP (green) and wild-type (grey) mice. **C** Image-derived input function derived [^{18}F]F-DED V_T in hippocampus and cerebellum of PS2APP and age matched wild-type mice at 5 and 19 months of age. **D** Coronal and sagittal slices of [^{18}F]F-DED V_T in PS2APP and age-matched wild-type mice are illustrated upon a MRI template. **E** Immunohistochemistry of similar GFAP and MAO-B levels in the cerebellum of PS2APP and wild-type mice at 19 months of age

Fig. 2 **A** Quantitative [18F]F-DED PET in comparison of PS2APP and age-matched wild-type mice animals at different ages. **B** Coronal planes of [18F]F-DED mean DVR maps at different ages of PS2APP animals and wild-type animals projected upon a MRI mouse atlas (gray scale). **C** Correlation of [18F]F-DED DVRs calculated from 60-min dynamic small-animal PET recordings with corresponding 30–60 min SUVR (reference region cerebellum). 95% confidence intervals are represented by color shaded areas
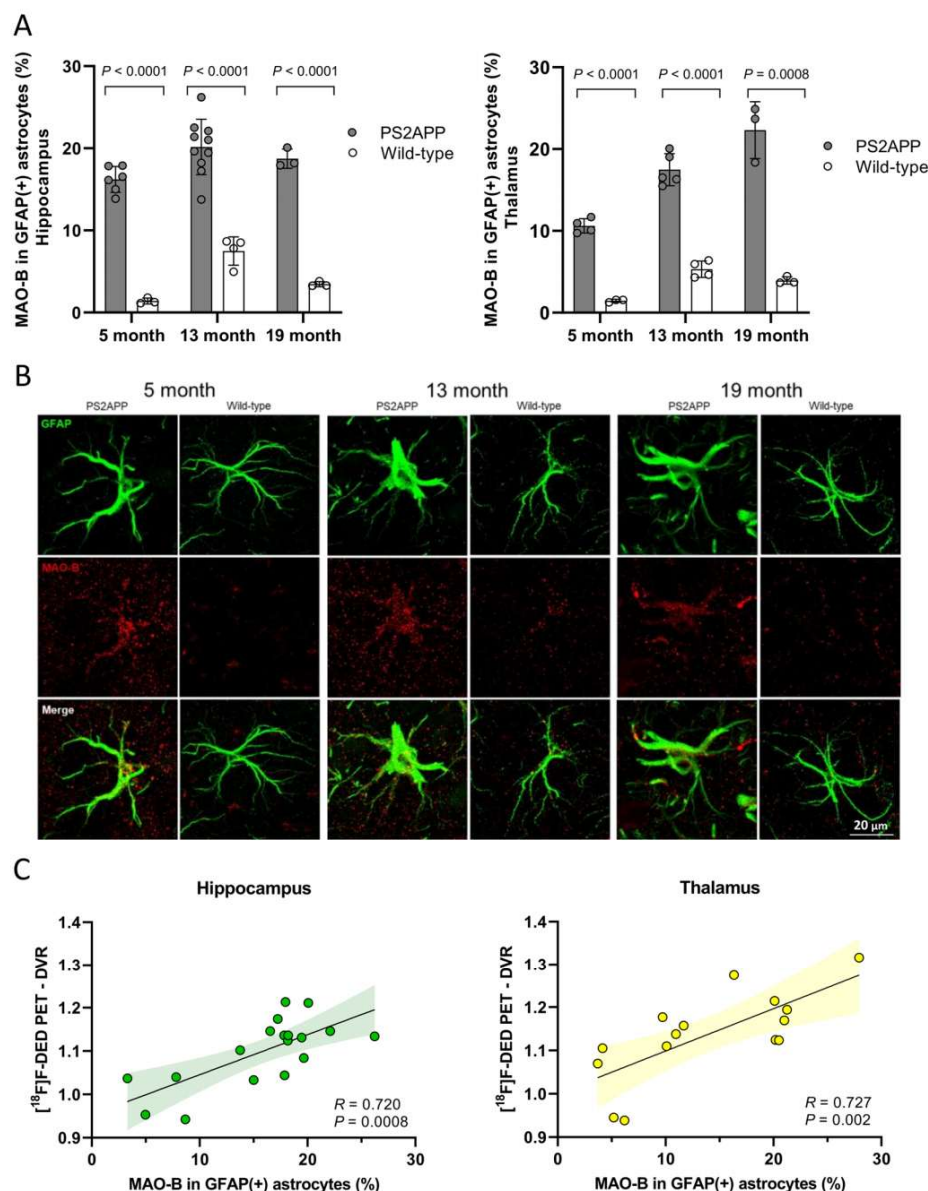
Results

Suitability of the cerebellum as a pseudo-reference region for [^{18}F]F-DED PET quantification in PS2APP and wild-type mice

The [^{18}F]F-DED blood input curve derived from the heart showed the expected sharp peak after 90 s and only low background activity in the late acquisition phase (Fig. 1A). Brain uptake of [^{18}F]F-DED indicated a rapid influx and sufficient washout from brain parenchyma (Fig. 1B). IDIF derived [^{18}F]F-DED V_T in hippocampus of PS2APP and wild-type mice were similar at 5 months of age (1.26 ± 0.06 vs. 1.19 ± 0.14; $p = 0.216$), but PS2APP mice had higher V_T at 19 months of age when compared to age-matched wild-type (1.31 ± 0.11 vs. 1.18 ± 0.12;

Fig. 3 **A** MAO-B expression in GFAP-positive astrocytes (%) in comparison of PS2APP and age-matched wild-type mice together with **B** illustration of immunohistochemical staining in the hippocampus. **C** Correlation of [^{18}F]F-DED PET DVRs with MAO-B in GFAP-positive astrocytes (%). 95% confidence intervals are represented by color shaded areas

$p = 0.043$; Fig. 1C, D). We observed no relevant difference in [18F]F-DED V_T of the cerebellum regardless of age and genotype (Fig. 1C, D). Immunohistochemistry of the cerebellum revealed only few GFAP positive cells with low MAO-B expression in PS2APP and wild-type mice (Fig. 1E).

[18F]F-DED PET detects reactive astrogliosis in PS2APP mice

PS2APP mice suggested an age-depended increase of [18F]F-DED DVR in hippocampus ($p = 0.003$) and thalamus ($p = 0.039$), whereas wild-type mice did not show significant changes of [18F]F-DED DVR with age in hippocampus ($p = 0.218$) and thalamus ($p = 0.372$). PS2APP mice showed elevated hippocampal [18F]F-DED DVR when compared to age-matched wild-type mice at 13 months ($+7.3\%$; $p = 0.022$) and 19 months of age ($+12.3\%$; $p < 0.0001$; Fig. 2A, B). Thalamic [18F]F-DED DVR of PS2APP mice were significantly higher at 5 months ($+4.3\%$; $p = 0.045$) and 19 months of age ($+15.2\%$; $p < 0.0001$; Fig. 2A, B) when compared to age-matched wild-type mice. There was a strong positive correlation between 0 and 60 min DVR, and the 30–60 min static frame SUVr for hippocampus ($R = 0.713$; $p < 0.0001$) and thalamus ($R = 0.783$; $p < 0.0001$; Fig. 2C). [18F]F-DED quantification in the neocortex showed similar results when compared to hippocampus and thalamus (Additional file 1: Fig. S1).

Immunohistochemical staining for MAO-B expression in GFAP-positive astrocytes showed an early onset of elevated MAO-B expression in PS2APP mice when compared to wild-type mice which increased with age (Fig. 3A, B). Higher MAO-B expression with increase in GFAP-positive astrocytes of PS2APP mice of all age-related groups was observed when compared to their age-matched wild-type controls in hippocampus (all $p < 0.001$) and thalamus (all $p < 0.01$). MAO-B in GFAP-positive astrocytes showed a strong positive correlation with the [18F]F-DED uptake in vivo in hippocampus ($R = 0.720$; $p < 0.001$) and in thalamus ($R = 0.727$; $p = 0.002$; Fig. 3C).

Hippocampal MAO-B PET signal as a potential early biomarker in PS2APP mice
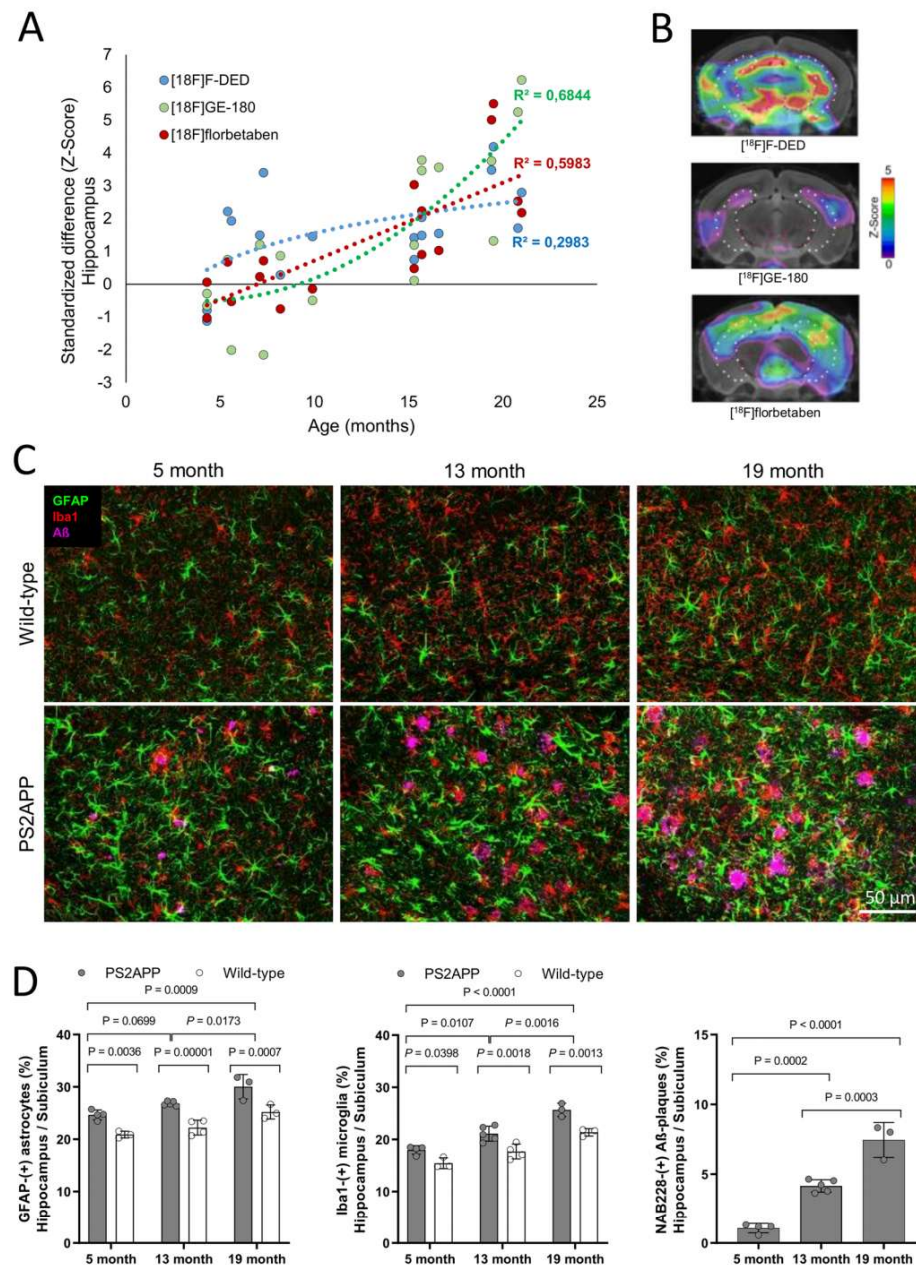
To compare trajectories of reactive astrocytes, activated microglia and β-amyloidosis, we calculated standardized differences of tracer signals in the hippocampus of PS2APP mice (vs. WT) for [18F]F-DED, [18F]GE-180 and [18F]florbetaben. [18F]F-DED as a function of age indicated a logarithmic fit ($y = 1.33\ln(x) - 1.50$; $R^2 = 0.298$), whereas [18F]GE-180 ($y = 0.02x^2 - 0.15x - 0.20$; $R^2 = 0.684$) and [18F]florbetaben ($y = 0.01x^2 - 0.05x - 0.28$; $R^2 = 0.621$) indicated exponential fits (Fig. 4A, B). Standardized

differences between 4.3 and 9.9 months of age were higher for [18F]F-DED when compared to [18F]GE-180 ($p = 0.044$) and [18F]florbetaben ($p = 0.039$). Immunohistochemistry confirmed astrogliosis in PS2APP mice starting as early as 5 months, accompanying the Aβ-plaque formation, which occurs first in the hippocampus/subiculum and spreads to the cortex and thalamus with increasing age (Fig. 4C, D; Additional file 1: Fig. S2). In PS2APP mice at 5 months of age, visual and quantitative increases of GFAP(+) astrocytes exceeded the increases of Iba1(+) microglia (Fig. 4C, D).

Initial clinical experience with [18F]F-DED PET matches expected magnitude and topology of reactive astrogliosis in patients with neurological diseases

Based on the promising preclinical data, [18F]F-DED imaging was translated to the clinical stage. [18F]F-DED was administered to eight patients and one healthy control (Table 2). The mean and standard deviation of the administered mass of [18F]F-DED was 0.074 ± 0.057 µg (range, 0.020–0.197 µg). The mean administered activity was 177 ± 35 MBq (range, 134–244 MBq). There were no adverse or clinically detectable pharmacologic effects in any of the nine subjects and no significant changes in vital signs. The injection and PET/CT procedures were well-tolerated in all participants. In the kinetic modeling analyses, a slightly superior fit of the 2TC3k model over the 1TC2k model was observed in the brainstem, the medio-temporal lobe and the putamen, however, driven by a single patient with exceptionally high fitting values. There was also no further improvement when comparing the 2TC4k model with the 2TC3k model, since a fourth parameter to the kinetic model did not lead to a significant reduction in the variation of residuals (Additional file 1: Table S1). We, therefore, concluded that the 1TC2k model represents human [18F]F-DED PET data best and generated V_T images based on that model (see Fig. 5). In addition, we validated the agreement between V_T values based on the 1TC2k compartment model and Logan Plot by computing Bland–Altman as well as scatter plots which showed no significant over- or underestimation for either method of quantification (Additional file 1: Fig. S3). A visual comparison of the quantitative V_T values regions confirmed this high level of concordance in all five target regions (Additional file 1: Table S2).

[18F]F-DED PET V_T and SUVr images corresponded to the expected patterns of MAO-B expression in brain and to the phenotype of the examined patients (Fig. 5, Additional file 1: Figs. S4–S6). The patient with Alzheimer's pathologic change that did not yet show evidence of tau pathology ([18F]PI-2620 PET) and who had no significant neurodegeneration as assessed by β-amyloid-PET perfusion imaging (A + T-N-), revealed high cortical and
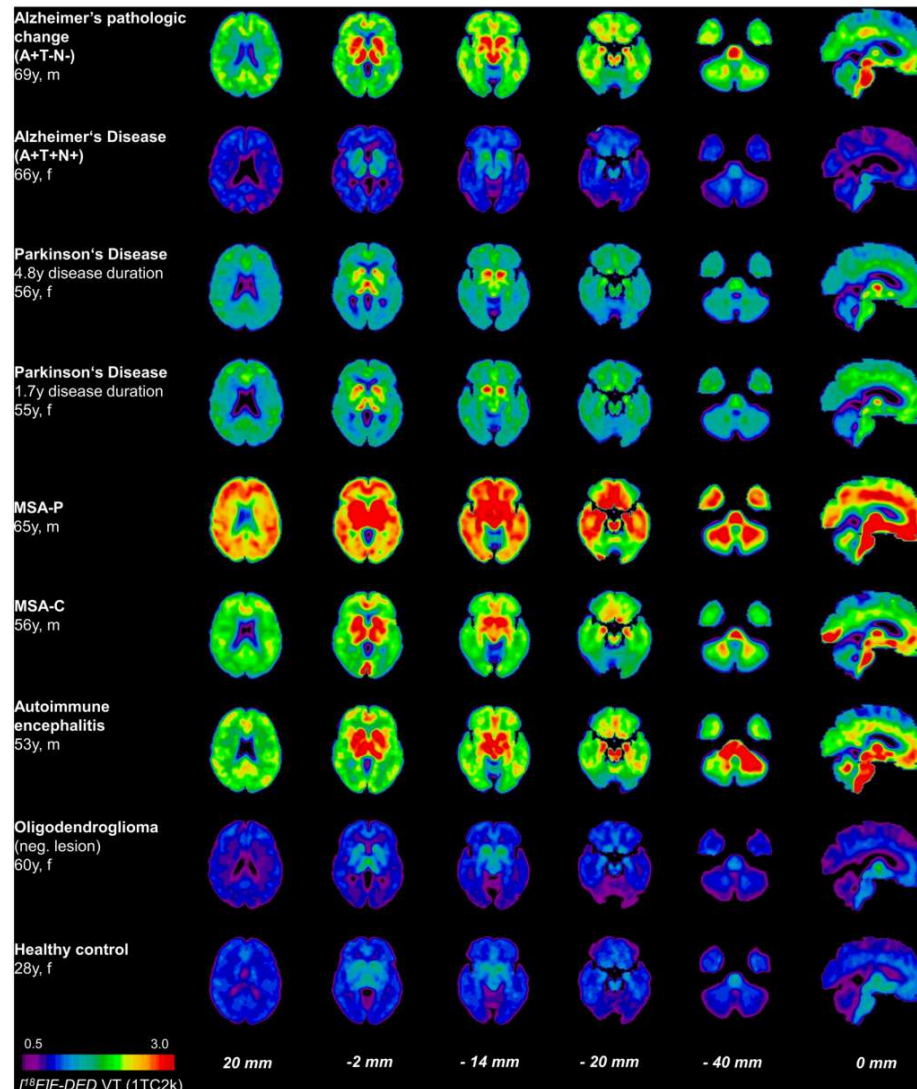
Fig. 4 **A** Life-course kinetics for PS2APP mice as expressed by standardized differences (z-score) in hippocampus for the 3 radiotracers. **B** Coronal planes of z-scores for the three radiotracers. **C** Sagittal plane of the hippocampus/subiculum of wild type and PS2APP mice stained against GFAP, Iba1 and Aβ at 5, 13 and 19 months of age. **D** Mean (± SD) GFAP, Iba1 and Aβ staining (area-%) for PS2APP animals at different ages compared to age-matched wild-type animals

subcortical [^{18}F]F-DED binding with regional predominance in cortical AD signature regions (Fig. 5; Additional file 1: Figs. S4–S7). Relatively low [^{18}F]F-DED binding

was observed in the patient with AD and who had evidence for the presence of β-amyloid and tau pathology (both assessed in CSF) and neurodegeneration as

Fig. 5 Axial and sagittal planes show [^{18}F]F-DED volumes of distribution (V$_T$) based on the 1TC2k compartment model at levels of neocortical regions, basal ganglia, hippocampus, cerebellum (all coronal) and brainstem (sagittal). The lesions of patients with autoimmune encephalitis and oligodendroglioma are indicated with white arrows. ATN indicates biomarker positivity for β-amyloid, tau and neurodegeneration in patients belonging to the AD continuum. MSA = multiple systems atrophy

assessed by [^{18}F]FDG–PET (A + T + N +; Fig. 5; Additional file 1: Fig. S7). In Parkinson's disease, moderate global [^{18}F]F-DED binding with pronounced signal in the basal ganglia was observed in two patients with 1.7 and 4.8 year disease duration. Both patients with MSA had much stronger [^{18}F]F-DED binding in cortical and subcortical brain regions when compared to patients with PD (MSA-P > MSA-C > PD) with predominance in basal ganglia (MSA-P), pons (both) and cerebellar white

matter (MSA-C) and with a higher cerebellum-to-putamen-ratio in the patient with MSA-C (0.81) when compared to MSA-P (0.73; Fig. 5; Additional file 1: Fig. S7). The patient with autoimmune encephalitis had a strong [^{18}F]F-DED binding with predominance in the cerebellar peduncles and the left cerebellar deep white matter, matching but also extending the lesions on MRI (Fig. 5; Additional file 1: Fig. S7). The patient with oligodendroglioma was [^{18}F]F-DED negative at the lesion site (right

frontal cortex) and indicated regional [^{18}F]F-DED binding that followed physiological MAO-B expression in healthy brain, such as the healthy control (Fig. 5) [17, 18]. [^{18}F]F-DED V_T images based on Logan Plot analysis revealed matching regions of elevated [^{18}F]F-DED binding (Additional file 1: Fig. S4).

Time-activity-curves showed fast brain uptake and a region dependent washout until 10–20 min p.i.. The cerebellar white matter indicated further moderate washout > 20 min p.i., whereas [^{18}F]F-DED binding in all target regions indicated stable (irreversible) binding in the late acquisition phase (Additional file 1: Fig. S8).

Discussion
In recent years, several PET tracers have been developed that target MAO-B, a surrogate for reactive astrocytes and, therefore, a promising new biomarker for neuroinflammation in various neurological diseases. However, most of these ligands have so far been based on [^{11}C] [33–35], whose short half-life (20.4 min) limits its use in clinical settings to centers with on-site cyclotrons. Consequently, an alternative radiolabeling has recently been carried out on the basis of [^{18}F], which possesses a much longer half-life of 109.8 min and is, therefore, more suitable for broad clinical use. Adding to that, the deuteration of [^{18}F]F-DED overcomes previous issues concerning high background signaling by enabling a better wash-out from regions low in MAO-B expression [16], thus yielding excellent tracer properties for neuroimaging in both rodents and humans. Even though in the present study, we were not able to directly provide evidence for the binding specificity of [^{18}F]F-DED, initial work done by Nag et al. (2015) showed high in vitro binding of this radiotracer to regions with increased levels of MAO-B in the monkey brain. In addition, blocking of MAO-B with L-deprenyl successfully suppressed any [^{18}F]F-DED binding thereafter [16]. We, therefore, based our work on the assumption that this tracer targets MAO-B with adequate specificity. With regard to radiometabolites, we were not able to obtain a direct analysis of arterial blood in the current study. Here, too, we based our assumption on previous findings indicating that [^{18}F]F-DED is partly metabolized and has a similar retention time when compared to the less lipophilic metabolites [16]. However, even though this byproduct could likely contaminate [^{18}F]F-DED PET signal, only about 5% of overall radioactivity was previously attributed to [^{18}F]flurometamphatamine-D2 [16]. Hence, we assumed that a sufficiently high proportion of our [^{18}F]F-DED signal represents the parent compound and, therefore, aimed to investigate the potential use of this radiotracer as a biomarker for early neuroinflammation in both transgenic mice as well as a human pilot sample.

The first part of our study consisted of a cross-sectional investigation of [^{18}F]F-DED PET in the PS2APP β-amyloid mouse model in conjunction with semi-quantitative immunohistochemical validation. Our preclinical findings showed an age-dependent increase of [^{18}F]F-DED signal in the hippocampus and thalamus in PS2APP mice. These transgenic mice typically start expressing β-amyloid plaques at about 5–6 months of age [21], with a close correlation to TSPO expression during the later life course [23]. Similarly, reactive astrogliosis in PS2APP showed a close topological association with β-amyloid pathology during aging with highest abundance in hippocampus, thalamus and cortex. Increasing MAO-B PET signals with age in transgenic models of β-amyloid pathology are in line with a previous study using [^{11}C]DED in APP$_{ArcSwe}$ mice compared to wild-type mice [36]. However, another study using this tracer in APP$_{Swe}$ mice found increased MAO-B PET signals before onset of fibrillary β-amyloid pathology compared to wild type but decreases of cortical and hippocampal [^{11}C]DED signals towards wild-type levels during aging [7]. Thus, longitudinal trajectories of MAO-B PET signals may depend on the used mouse model and specific characteristics of their β-amyloid pathology which deserves head-to-head comparison with equal methodology in future studies. Interestingly, in our study, we found a [^{18}F]F-DED signal elevation that preceded those of other AD biomarkers, showing earlier elevation and a plateau (logarithmic vs. exponential function) when compared to TSPO–PET and β-amyloid-PET signal. Keeping potential differences in both the sensitivity of the tracer and the target abundance in mind, this supports the assumption of an early astrocyte burst [37] in the pathophysiology of AD and substantiates the value of imaging astrogliosis as an early AD biomarker. In line, elevated GFAP levels were observed in plasma of early and late onset AD [38], but also in β-amyloid-positive cognitively normal individuals when compared to β-amyloid-negative controls [39]. Furthermore, [^{18}F]F-DED signal strongly correlated with MAO-B expression in GFAP-positive astrocytes in our study, which strengthens the assumption that this radiotracer detects MAO-B positive reactive astrogliosis in a proportional manner. Importantly, the correlation of MAO-B PET signals with MAO-B positivity in GFAP(+) astrocytes allowed to correlate PET signal increases specifically with the claimed astrocytic source. We note that previous studies did not consistently report co-localized MAO-B and GFAP expression in immunohistochemistry [36], which indicates that our validated antibody could have superior sensitivity to astrocytic MAO-B expression.

Our preclinical study was also used to investigate the cerebellum as a potential reference tissue for simplified

[^{18}F]F-DED quantification, as previous studies have revealed that this region expresses only low amounts of MAO-B and shows only low ligand uptake [15, 40]. Adding to that, this tissue is also often used for standardization of other radiotracers used in this mouse model [23]. However, defining a proper reference region, i.e., one with no specific radiotracer uptake, is not entirely possible with MAO-B due to it being ubiquitously expressed throughout the brain (Additional file 1: Fig. S9). We, therefore, decided to normalize our preclinical [^{18}F]F-DED data by defining a pseudo-reference region with comparatively low specific radiotracer uptake. This was indeed the case for the cerebellum, for which we did not find any significant differences in [^{18}F]F-DED V_T signal between transgenic and wild-type mice as well as similarly low staining patterns of GFAP. Thus, we concluded that specific uptake was not affected by diseases status or age and that this region could, therefore, serve as a suitable pseudo-reference for our quantitative analyses (Fig. 1C, E).

Based on our previous experience with [^{18}F]THK-5351 in MSA and PD [41], we further applied [^{18}F]F-DED in a pilot sample of patients and one healthy control, with the rationale to detect globally and regionally increased MAO-B expression. Preliminary data of our first-in-human [^{18}F]F-DED sample matched the expected binding magnitude and topology of MAO-B expression in various neurological diseases, although no generalized conclusions can yet be drawn due to the low number of cases. The topology in the healthy control and in regions with assumed low neuropathology matched the expression of MAO-B in healthy brain with highest abundance in the basal ganglia and low abundance in the cerebellum [17, 18]. Increased MAO-B expression in early stages of the AD continuum which were ameliorated at later stages were previously described for [^{11}C]DED [15]. In line with the hypothesis of an astrocyte burst in early AD, we found strong [^{18}F]F-DED binding with predominance in parietal and temporal AD signature regions when examining one β-amyloid-positive MCI patient that had no evidence of tau pathology and neurodegeneration yet. Contrary, [^{18}F]F-DED binding was only low in the second patient with AD that had elevation of p-tau and widespread FDG hypometabolism. [^{18}F]F-DED binding in two patients with PD indicated low and similar MAO-B expression at 1.7 and 4.8 year disease duration, whereas previous observations with the imidazoline 2 astrocyte tracer [^{11}C]BU99008 showed a decline at later stages [42]. [^{18}F]F-DED PET in both examined patients with MSA was higher when compared to PD and congruent with the phenotype, indicating pronounced binding in cerebellar white matter and pons in presence of clinical cerebellar predominance and pronounced binding

in the putamen in MSA-P. A broader range of patients with typical and atypical Parkinsonian syndromes needs to be investigated with [^{18}F]F-DED to allow conclusions on specific binding characteristics. Assessment of astrogliosis could also reflect a useful diagnostic biomarker in MSA, since MAO-B expression levels of patients with MSA exceeded the levels of patients with PD and healthy controls in autopsy [43]. Strong [^{18}F]F-DED binding was also observed in a patient with autoimmune encephalitis with predominant cerebellar involvement, indicating astrocytosis/reactive astrogliosis. Thus, [^{18}F]F-DED PET could be an interesting additional tool for assessment of the regional extent and the lesion activity in patients with inflammatory diseases of the CNS. The patient with oligodendroglioma had lower [^{18}F]F-DED binding in the lesion when compared to cortical regions. Thus, the signal in brain tissue outside the lesion may serve as a preliminary pseudo control of normal MAO-B expression together with the young healthy control investigated. Taken together, these first-in-human [^{18}F]F-DED data revealed MAO-B expression patterns of interest that may serve differential diagnosis of various neurodegenerative diseases. However, given the small sample size of the human cohort and lacking controls these observations should be interpreted with caution. Confirmation in a larger cohort and longitudinal follow-up imaging is warranted. The [^{18}F]F-DED V_T obtained by an exploratory IDIF encourage further validation by arterial sampling including metabolite correction.

Conclusion

In vivo imaging by PET with the novel MAO-B tracer [^{18}F]F-DED indicates a potential for assessment of reactive astrogliosis in AD mouse models and patients with neurological diseases. [^{18}F]F-DED binding correlates with immunohistochemical gold standard assessment and our results suggest that [^{18}F]F-DED could be used as an early biomarker for neuroinflammation in this transgenic AD mouse model. Translation into preliminary human data showed regional congruence between tracer signal and expected disease topology, which indicates the potential for detection of regionally altered MAO-B expression.

Supplementary Information

The online version contains supplementary material available at https://doi.org/10.1186/s12974-023-02749-2.

Additional file 1: Table S1. Kinetic modelling overview in the human cohort**.** A superior fit (*) of the 2TC3k compared to the 1TC2k model was found in three target regions due to high values in the autoimmune encephalitis (AIE) patient. F tests indicate that the more complex 2TC4k model does not lead to a further significant reduction in the variation of residuals. AIC = Akaike Information Criterion; SC = Schwartz Information Criterion; χ^2 = Sum of Squares of the weighted residuals divided by the degrees of freedom; AD = Alzheimer's disease continuum; PD =

Parkinson's disease; MSA = multiple systems atrophy; ODG = oligodendroglioma. **Table S2.** Quantitative comparison of Volumes of distribution (V_T) generated on the basis of a 1TC2k compartmental and a Logan Plot. Intraindividual comparison reveals similar values across all target regions for both quantification methods. AD = Alzheimer's disease continuum; PD = Parkinson's disease; MSA = multiple systems atrophy; AIE = autoimmune encephalitis; ODG = oligodendroglioma. **Figure S1.** (A) Mean (± SD) distribution volume ratios (DVRs) of [^{18}F]F-DED PET for PS2APP animals at different ages compared to age-matched wild-type animals for the target region cortex. Significant differences between genotypes per timepoint are indicated. (B) Correlation of [^{18}F]F-DED DVRs calculated from 60-min dynamic small-animal PET recordings with corresponding 30–60-min SUVR (reference region cerebellum). 95% confidence intervals are represented by dotted lines. **Figure S2.** Sagittal plane showing the cortex, hippocampus and thalamus stained against GFAP for astrocytes and Aβ (NAB228) for Aβ plaques in PS2APP mice at 5, 13 and 19 months of age. Plaques start to from in the subiculum at 5 months of age and spread to the cortex and thalamus. The plaque load is accompanied by astrogliosis which also starts 5 months and increases in an age-related manner. **Figure S3.** Bland–Altman plots (first row) comparing V_T values based on compartmental and Logan Plot analyses. The red line corresponds to the mean difference of V_T values, the black lines indicate the limits of agreement (Mean ± 1.96 * SD). Correlational analyses (second row) reveal high correlations between V_T values based on the 1TC2k and those based on Logan Plot. **Figure S4.** Axial and sagittal planes show [^{18}F]F-DED Volumes of distribution (V_T) based on a Logan Plot at levels of neocortical regions, basal ganglia, hippocampus, cerebellum (all coronal) and brainstem (sagittal). The lesions of patients with autoimmune encephalitis and oligodendroglioma are indicated with white arrows. **Figure S5.** Axial and sagittal planes show [^{18}F]F-DED standardized uptake value ratios (SUVr) based on a parietal white matter reference region and a 30–60-min time frame at levels of neocortical regions, basal ganglia, hippocampus, cerebellum (all coronal) and brainstem (sagittal). Scaling is optimized to evaluate signal changes in the basal ganglia and brainstem regions. Parietal and temporal Alzheimer's disease signature regions are indicated with pink arrows. Regions of interest in patients with Parkinson's disease and multiple systems atrophy (MSA) are indicated with orange arrows. The lesions of the patient with autoimmune encephalitis are indicated with white arrows. **Figure S6.** Axial and sagittal planes show [^{18}F]F-DED standardized uptake value ratios (SUVr) based on a parietal white matter reference region and a 30–60-min time frame at levels of neocortical regions, basal ganglia, hippocampus, cerebellum (all coronal) and brainstem (sagittal). Scaling is optimized to evaluate signal changes in the cortical regions. Parietal and temporal Alzheimer's disease signature regions are indicated with pink arrows. Regions of interest in patients with Parkinson's disease and multiple systems atrophy (MSA) are indicated with orange arrows. The lesions of the patient with autoimmune encephalitis are indicated with white arrows. **Figure S7.** Additional imaging characteristics of investigated patients of the Alzheimer's disease (AD) continuum, multiple systems atrophy (MSA) and autoimmune encephalitis as assessed by β-amyloid-PET, tau-PET, FDG–PET and MRI. **Figure S8.** [^{18}F]F-DED time-activity-curves (TACs) of patients with neurodegenerative diseases and multiple sclerosis in contrast to a patient with MAO-B negative oligodendroglioma. All TACs are scaled to the maximum SUV to allow direct comparison of the washout phase. MSA-P = Multiple systems atrophy–parkinsonian subtype; MSA-C = Multiple systems atrophy–cerebellar subtype; ODG = Oligodendroglioma; PD = Parkinson's disease; AD = Alzheimer's disease (A = amyloid-β; T = tau; N = neurodegeneration); SUV = standard-uptake-value; min = minutes. **Figure S9.** (**A**) MAO-B expression in GFAP-(+) astrocytes, (**B**) TPH2-(+) serotonergic neurons of the raphe nucleus and (**C**) in endothelia cells of blood vessels of wild type and PS2APP mice.

Author contributions
AB: performed PET acquisition, image analysis and interpretation of preclinical scans, performed regional PET analyses, correlated multitracer results and performed statistical analyses, wrote the first draft of the manuscript with input of all co-authors. CK: performed immunohistochemical staining and analysis, participated in writing the manuscript with input of all co-authors. LV: performed PET acquisition, image analysis and interpretation of human scans, performed regional PET analyses, participated in writing the manuscript with input of all co-authors. SK: recruited patients with neurodegenerative diseases and assessed clinical scores. KW, FE, BB: performed preclinical PET acquisition, image analysis and interpretation. BS, MS: performed clinical PET acquisition, image analysis and interpretation. AB, UF, SQ: contributed to patient recruitment and interpretation of clinical PET results. BSR, SS: acquisition, analysis, and interpretation of clinical MRI scans. LB: analysis and interpretation of PET results. MS, EJ, SL: performed and improved radiosynthesis of tracer, performed analyses of. the tracer synthesis. IB: performed clinical PET acquisition. NK, AM, AWS: development of the radiotracer, precursor, contributed to interpreting data, enhancing intellectual content of manuscript. PB, JCT, TK, RP: contributed to interpreting data, enhancing intellectual content of manuscript. NLA, MK, RP: conception and design, contributed to interpreting data, enhancing intellectual content of manuscript. LP, JH: contributed to conception and design, interpretation of IHC data. MB: contributed to conception and design, acquiring PET data, analyzing and interpreting data, fusion of data, wrote the manuscript with input of all co-authors. All authors read and approved the final manuscript.

Availability of data and materials
All raw data can be obtained by the corresponding author upon reasonable request.

Declarations

Ethics approval and consent to participate
The study was approved by the local ethics committee of the medical faculty of the LMU Munich (Application Number: 21-0721) and written informed consent was obtained from all participants.

Consent for publication
Not applicable.

Competing interests
NK, AM and AWS are employees of Life Molecular Imaging. MB received research funding from Life Molecular Imaging. No other potential competing interest relevant to this article exist.

Author details
[1]Department of Nuclear Medicine, University Hospital of Munich, LMU Munich, Marchioninistr.15, 81377 Munich, Germany. [2]German Center for Neurodegenerative Diseases (DZNE), Munich, Germany. [3]Department of Neurology, University Hospital of Munich, LMU Munich, Munich, Germany. [4]Department of Neurosurgery, University Hospital, LMU Munich, Munich, Germany. [5]Department of Radiology, University Hospital of Munich, LMU Munich, Munich, Germany. [6]Department of Psychiatry and Psychotherapy, University Hospital of Munich, LMU Munich, Munich, Germany. [7]Life Molecular Imaging GmbH, Berlin, Germany. [8]Munich Cluster for Systems Neurology (SyNergy), Munich, Germany. [9]German Cancer Consortium (DKTK), Partner Site Munich, German Cancer Research Center (DKFZ), Heidelberg, Germany. [10]Institute of Clinical Neuroimmunology, University Hospital, LMU Munich, Munich, Germany. [11]Biomedical Center, Faculty of Medicine, LMU Munich, Munich, Germany. [12]Ageing Epidemiology (AGE) Research Unit, School of Public Health, Imperial College, London, UK. [13]Sheffield Institute for Translational Neuroscience (SITraN), University of Sheffield, Sheffield, UK. [14]Center for Neuropathology and Prion Research, LMU Munich, Munich, Germany.

References

1. Keren-Shaul H, Spinrad A, Weiner A, Matcovitch-Natan O, Dvir-Szternfeld R, Ulland TK, David E, Baruch K, Lara-Astaiso D, Toth B, et al. A unique microglia type associated with restricting development of Alzheimer's disease. Cell. 2017;169:1276-1290.e1217.
2. Liddelow SA, Guttenplan KA, Clarke LE, Bennett FC, Bohlen CJ, Schirmer L, Bennett ML, Munch AE, Chung WS, Peterson TC, et al. Neurotoxic reactive astrocytes are induced by activated microglia. Nature. 2017;541:481–7.
3. Rostami J, Mothes T, Kolahdouzan M, Eriksson O, Moslem M, Bergström J, Ingelsson M, O'Callaghan P, Healy LM, Falk A, Erlandsson A. Cross-talk between astrocytes and microglia results in increased degrada-tion of α-synuclein and amyloid-β aggregates. J Neuroinflammation. 2021;18:124.
4. Ballard C, Gauthier S, Corbett A, Brayne C, Aarsland D, Jones E. Alzheimer's disease. Lancet. 2011;377:1019–31.
5. Jack CR Jr, Bennett DA, Blennow K, Carrillo MC, Dunn B, Haeberlein SB, Holtzman DM, Jagust W, Jessen F, Karlawish J, et al. NIA-AA research framework: toward a biological definition of Alzheimer's disease. Alzhei-mers Dement. 2018;14:535–62.
6. González-Reyes RE, Nava-Mesa MO, Vargas-Sánchez K, Ariza-Salamanca D, Mora-Muñoz L. Involvement of astrocytes in Alzheimer's disease from a neuroinflammatory and oxidative stress perspective. Front Mol Neurosci. 2017;10:427.
7. Rodriguez-Vieitez E, Ni R, Gulyás B, Tóth M, Häggkvist J, Halldin C, Voytenko L, Marutle A, Nordberg A. Astrocytosis precedes amyloid plaque deposition in Alzheimer APPswe transgenic mouse brain: a correlative positron emission tomography and in vitro imaging study. Eur J Nucl Med Mol Imaging. 2015;42:1119–32.
8. Rodriguez-Vieitez E, Saint-Aubert L, Carter SF, Almkvist O, Farid K, Schöll M, Chiotis K, Thordardottir S, Graff C, Wall A, et al. Diverging longitudinal changes in astrocytosis and amyloid PET in autosomal dominant Alzhei-mer's disease. Brain. 2016;139:922–36.
9. Bellaver B, Ferrari-Souza JP, da Uglione Ros L, Carter SF, Rodriguez-Vieitez E, Nordberg A, Pellerin L, Rosa-Neto P, Leffa DT, Zimmer ER. Astrocyte biomarkers in Alzheimer disease: a systematic review and meta-analysis. Neurology. 2021. https://doi.org/10.1212/WNL.0000000000012109.
10. Escartin C, Galea E, Lakatos A, O'Callaghan JP, Petzold GC, Serrano-Pozo A, Steinhäuser C, Volterra A, Carmignoto G, Agarwal A, et al. Reactive astrocyte nomenclature, definitions, and future directions. Nat Neurosci. 2021;24:312–25.
11. Eng LF, Ghirnikar RS, Lee YL. Glial fibrillary acidic protein: GFAP-thirty-one years (1969–2000). Neurochem Res. 2000;25:1439–51.
12. Sofroniew MV. Molecular dissection of reactive astrogliosis and glial scar formation. Trends Neurosci. 2009;32:638–47.
13. Harada R, Furumoto S, Kudo Y, Yanai K, Villemagne VL, Okamura N. Imaging of reactive astrogliosis by positron emission tomography. Front Neurosci. 2022;16: 807435.
14. Levitt P, Pintar JE, Breakefield XO. Immunocytochemical demonstration of monoamine oxidase B in brain astrocytes and serotonergic neurons. Proc Natl Acad Sci USA. 1982;79:6385–9.
15. Carter SF, Scholl M, Almkvist O, Wall A, Engler H, Langstrom B, Nordberg A. Evidence for astrocytosis in prodromal Alzheimer disease provided by 11C-deuterium-L-deprenyl: a multitracer PET paradigm combining 11C-Pittsburgh compound B and 18F-FDG. J Nucl Med. 2012;53:37–46.
16. Nag S, Fazio P, Lehmann L, Kettschau G, Heinrich T, Thiele A, Svedberg M, Amini N, Leesch S, Catafu AM, et al. In vivo and in vitro characterization of a novel MAO-B inhibitor radioligand, 18F-labeled deuterated fluorode-prenyl. J Nucl Med. 2016;57:315–20.
17. Villemagne VL, Harada R, Dore V, Furumoto S, Mulligan R, Kudo Y, Burn-ham S, Krishnadas N, Bozinovski S, Huang K, et al. First-in-human evalua-tion of (18)F-SMBT-1, a novel (18)F-labeled MAO-B PET tracer for imaging reactive astrogliosis. J Nucl Med. 2022. https://doi.org/10.2967/jnumed.121.263254.
18. Villemagne VL, Harada R, Dore V, Furumoto S, Mulligan R, Kudo Y, Burn-ham S, Krishnadas N, Bourgeat P, Xia Y, et al. Assessing reactive astrogliosis with (18)F-SMBT-1 across the Alzheimer's disease spectrum. J Nucl Med. 2022. https://doi.org/10.2967/jnumed.121.263255.
19. Sacher C, Blume T, Beyer L, Biechele G, Sauerbeck J, Eckenweber F, Deussing M, Focke C, Parhizkar S, Lindner S, et al. Asymmetry of fibrillar plaque burden in amyloid mouse models. J Nucl Med. 2020;61:1825–31.
20. Richards JG, Higgins GA, Ouagazzal AM, Ozmen L, Kew JN, Bohrmann B, Malherbe P, Brockhaus M, Loetscher H, Czech C, et al. PS2APP transgenic mice, coexpressing hPS2mut and hAPPswe, show age-related cognitive deficits associated with discrete brain amyloid deposition and inflamma-tion. J Neurosci. 2003;23:8989–9003.
21. Ozmen L, Albientz A, Czech C, Jacobsen H. Expression of transgenic APP mRNA is the key determinant for beta-amyloid deposition in PS2APP transgenic mice. Neurodegener Dis. 2009;6:29–36.
22. Biechele G, Blume T, Deussing M, Zott B, Shi Y, Xiang X, Franzmeier N, Kleinberger G, Peters F, Ochs K, et al. Pre-therapeutic microglia activation and sex determine therapy effects of chronic immunomodulation. Thera-nostics. 2021;11:8964–76.
23. Brendel M, Probst F, Jaworska A, Overhoff F, Korzhova V, Albert NL, Beck R, Lindner S, Gildehaus FJ, Baumann K, et al. Glial activation and glucose metabolism in a transgenic amyloid mouse model: a triple-tracer PET study. J Nucl Med. 2016;57:954–60.
24. Biechele G, Monasor LS, Wind K, Blume T, Parhizkar S, Arzberger T, Sacher C, Beyer L, Eckenweber F, Gildehaus FJ, et al. Glitter in the darkness? Nonfibrillar beta-amyloid plaque components significantly impact the beta-amyloid PET signal in mouse models of alzheimer disease. J Nucl Med. 2022;63:117–24.
25. Biechele G, Franzmeier N, Blume T, Ewers M, Luque JM, Eckenweber F, Sacher C, Beyer L, Ruch-Rubinstein F, Lindner S, et al. Glial activation is moderated by sex in response to amyloidosis but not to tau pathology in mouse models of neurodegenerative diseases. J Neuroinflammation. 2020;17:374.
26. Sacher C, Blume T, Beyer L, Peters F, Eckenweber F, Sgobio C, Deussing M, Albert NL, Unterrainer M, Lindner S, et al. Longitudinal PET monitoring of amyloidosis and microglial activation in a second-generation amyloid-beta mouse model. J Nucl Med. 2019;60:1787–93.
27. Overhoff F, Brendel M, Jaworska A, Korzhova V, Delker A, Probst F, Focke C, Gildehaus FJ, Carlsen J, Baumann K, et al. Automated spatial brain normalization and hindbrain white matter reference tissue give improved [(18)F]-Florbetaben PET quantitation in Alzheimer's model mice. Front Neurosci. 2016;10:45.
28. Ma Y, Hof PR, Grant SC, Blackband SJ, Bennett R, Slatest L, McGuigan MD, Benveniste H. A three-dimensional digital atlas database of the adult C57BL/6J mouse brain by magnetic resonance microscopy. Neurosci-ence. 2005;135:1203–15.
29. Xiang X, Wind K, Wiedemann T, Blume T, Shi Y, Briel N, Beyer L, Biechele G, Eckenweber F, Zatcepin A, et al. Microglial activation states drive glucose uptake and FDG-PET alterations in neurodegenerative diseases. Sci Transl Med. 2021;13:eabe5640.
30. Logan J, Fowler JS, Volkow ND, Wolf AP, Dewey SL, Schlyer DJ, MacGregor RR, Hitzemann R, Bendriem B, Gatley SJ, et al. Graphical analysis of revers-ible radioligand binding from time-activity measurements applied to [N-11C-methyl]-(-)-cocaine PET studies in human subjects. J Cereb Blood Flow Metab. 1990;10:740–7.
31. Rominger A, Brendel M, Burgold S, Keppler K, Baumann K, Xiong G, Mille E, Gildehaus FJ, Carlsen J, Schlichtiger J, et al. Longitudinal assessment of cerebral beta-amyloid deposition in mice overexpressing Swedish mutant beta-amyloid precursor protein using 18F-florbetaben PET. J Nucl Med. 2013;54:1127–34.
32. Brendel M, Barthel H, van Eimeren T, Marek K, Beyer L, Song M, Palleis C, Gehmeyr M, Fietzek U, Respondek G, et al. Assessment of 18F-PI-2620 as a biomarker in progressive supranuclear palsy. JAMA Neurol. 2020;77:1408–19.
33. Fowler JS, MacGregor RR, Wolf AP, Arnett CD, Dewey SL, Schlyer D, Christman D, Logan J, Smith M, Sachs H, et al. Mapping human brain monoamine oxidase A and B with 11C-labeled suicide inactivators and PET. Science. 1987;235:481–5.
34. Rusjan PM, Wilson AA, Miler L, Fan I, Mizrahi R, Houle S, Vasdev N, Meyer JH. Kinetic modeling of the monoamine oxidase B radioligand [(1)(1)C]SL25.1188 in human brain with high-resolution positron emission tomography. J Cereb Blood Flow Metab. 2014;34:883–9.
35. Santillo AF, Gambini JP, Lannfelt L, Långström B, Ulla-Marja L, Kilander L, Engler H. In vivo imaging of astrocytosis in Alzheimer's disease: an ¹¹C-L-deuteriodeprenyl and PIB PET study. Eur J Nucl Med Mol Imaging. 2011;38:2202–8.

36. Olsen M, Aguilar X, Sehlin D, Fang XT, Antoni G, Erlandsson A, Syvänen S. Astroglial responses to amyloid-beta progression in a mouse model of Alzheimer's disease. Mol Imaging Biol. 2018;20:605–14.
37. Carter SF, Herholz K, Rosa-Neto P, Pellerin L, Nordberg A, Zimmer ER. Astrocyte biomarkers in Alzheimer's disease. Trends Mol Med. 2019;25:77–95.
38. Elahi FM, Casaletto KB, La Joie R, Walters SM, Harvey D, Wolf A, Edwards L, Rivera-Contreras W, Karydas A, Cobigo Y, et al. Plasma biomarkers of astrocytic and neuronal dysfunction in early- and late-onset Alzheimer's disease. Alzheimers Dement. 2020;16:681–95.
39. Chatterjee P, Pedrini S, Stoops E, Goozee K, Villemagne VL, Asih PR, Verberk IMW, Dave P, Taddei K, Sohrabi HR, et al. Plasma glial fibrillary acidic protein is elevated in cognitively normal older adults at risk of Alzheimer's disease. Transl Psychiatry. 2021;11:27.
40. Gulyás B, Pavlova E, Kása P, Gulya K, Bakota L, Várszegi S, Keller E, Horváth MC, Nag S, Hermecz I, et al. Activated MAO-B in the brain of Alzheimer patients, demonstrated by [11C]-L-deprenyl using whole hemisphere autoradiography. Neurochem Int. 2011;58:60–8.
41. Schonecker S, Brendel M, Palleis C, Beyer L, Hoglinger GU, Schuh E, Rauchmann BS, Sauerbeck J, Rohrer G, Sonnenfeld S, et al. PET imaging of astrogliosis and tau facilitates diagnosis of Parkinsonian syndromes. Front Aging Neurosci. 2019;11:249.
42. Wilson H, Dervenoulas G, Pagano G, Tyacke RJ, Polychronis S, Myers J, Gunn RN, Rabiner EA, Nutt D, Politis M. Imidazoline 2 binding sites reflecting astroglia pathology in Parkinson's disease: an in vivo11C-BU99008 PET study. Brain. 2019;142:3116–28.
43. Tong J, Rathitharan G, Meyer JH, Furukawa Y, Ang LC, Boileau I, Guttman M, Hornykiewicz O, Kish SJ. Brain monoamine oxidase B and A in human parkinsonian dopamine deficiency disorders. Brain. 2017;140:2460–74.

Publisher's Note

6.   Publikation II

Assessment of synaptic loss in mouse models of β-amyloid and tau pathology using [18F]UCB-H PET imaging

Letizia Vogler [a], Anna Ballweg [a], Bernd Bohr [a], Nils Briel [d], Karin Wind [a], Melissa Antons [a], Lea H. Kunze [a], Johannes Gnörich [a], Simon Lindner [a], Franz-Josef Gildehaus [a], Karlheinz Baumann [e], Peter Bartenstein [a], Guido Boening [a], Sibylle I. Ziegler [a], Johannes Levin [b,c,f], Andreas Zwergal [f,g], Günter U. Höglinger [b,f], Jochen Herms [d], Matthias Brendel [a,b,c,*]

[a] Department of Nuclear Medicine, University Hospital of Munich, Ludwig-Maximilians-University (LMU) Munich, Munich, Germany
[b] German Center for Neurodegenerative Diseases (DZNE), Munich, Germany
[c] Munich Cluster for Systems Neurology (SyNergy), Munich, Germany
[d] Center for Neuropathology, LMU Munich, Munich, Germany
[e] Roche Pharma Research and Early Development, Neuroscience Discovery, Roche Innovation Center Basel, F. Hoffmann-La Roche Ltd., Basel, Switzerland
[f] Department of Neurology, University Hospital of Munich, LMU Munich, Munich, Germany
[g] German Center for Vertigo and Balance Disorders (DSGZ), University Hospital of Munich, LMU Munich, Munich, Germany

ARTICLE INFO

ABSTRACT

Objective: In preclinical research, the use of [18F]Fluorodesoxyglucose (FDG) as a biomarker for neurodegeneration may induce bias due to enhanced glucose uptake by immune cells. In this study, we sought to investigate synaptic vesicle glycoprotein 2A (SV2A) PET with [18F]UCB-H as an alternative preclinical biomarker for neurodegenerative processes in two mouse models representing the pathological hallmarks of Alzheimer's disease (AD).

Methods: A total of 29 PS2APP, 20 P301S and 12 wild-type mice aged 4.4 to 19.8 months received a dynamic [18F]UCB-H SV2A-PET scan (14.7 ± 1.5 MBq) 0–60 min post injection. Quantification of tracer uptake in cortical, cerebellar and brainstem target regions was implemented by calculating relative volumes of distribution (V_T) from an image-derived-input-function (IDIF). [18F]UCB-H binding was compared across all target regions between transgenic and wild-type mice. Additional static scans were performed in a subset of mice to compare [18F]FDG and [18F]GE180 (18 kDa translocator protein tracer as a surrogate for microglial activation) standardized uptake values (SUV) with [18F]UCB-H binding at different ages. Following the final scan, a subset of mouse brains was immunohistochemically stained with synaptic markers for gold standard validation of the PET results.

Results: [18F]UCB-H binding in all target regions was significantly reduced in 8-months old P301S transgenic mice when compared to wild-type controls (temporal lobe: p = 0.014; cerebellum: p = 0.0018; brainstem: p = 0.0014). Significantly lower SV2A tracer uptake was also observed in 13-months (temporal lobe: p = 0.0080; cerebellum: p = 0.006) and 19-months old (temporal lobe: p = 0.0042; cerebellum: p = 0.011) PS2APP transgenic versus wild-type mice, whereas the brainstem revealed no significantly altered [18F]UCB-H binding. Immunohistochemical analyses of post-mortem mouse brain tissue confirmed the SV2A PET findings. Correlational analyses of [18F]UCB-H and [18F]FDG using Pearson's correlation coefficient revealed a significant negative association in the PS2APP mouse model (R = -0.26, p = 0.018). Exploratory analyses further stressed microglial activation as a potential reason for this inverse relationship, since [18F]FDG and [18F]GE180 quantification were positively correlated in this cohort (R = 0.36, p = 0.0076).

Conclusion: [18F]UCB-H reliably depicts progressive synaptic loss in PS2APP and P301S transgenic mice, potentially qualifying as a more reliable alternative to [18F]FDG as a biomarker for assessment of neurodegeneration in preclinical research.

* Corresponding author at: Department of Nuclear Medicine, University Hospital of Munich, Ludwig-Maximilians-University (LMU) Munich, Munich, Germany.
E-mail address: matthias.brendel@med.uni-muenchen.de (M. Brendel).

1. Introduction

Within the spectrum of neurodegenerative diseases, Alzheimer's disease (AD) is not only the most prevalent but also amongst the most complex in terms of its intricate pathophysiology. With many dots yet to be connected, current consensus defines plaque and neurofibrillary tangle formation – due to amyloid-beta accumulation and associated with tau hyperphosphorylation, respectively – as two core characteristics of the disease's pathogenesis (Jack et al., 2018). In a cascade-like process, the formation of amyloid-β deposits presumably represents the central pathology during initial stages, while the aggregation of characteristic tau fibrils occurs at later times (Jack et al., 2010; Lemere and Masliah, 2010). Furthermore, a wealth of studies suggests that inflammatory cells such as activated microglia and reactive astrocytes are also a key element of the neurodegenerative trajectories, exerting both beneficial and harmful effects in a dynamic process over time. Microglia, in particular, likely engage in the clearance of amyloid debris early on but become dystrophic when chronically activated, resulting in wide spread synaptic loss, neuronal apoptosis and propagation of tau aggregates (Kitazawa et al., 2004; Leng and Edison, 2021). Taken together, this simplified pathological model builds the basis of the current A-T-N classification of AD, which aims to integrate three biomarkers (amyloidosis, tau, neurodegeneration) into the diagnostic research protocol, facilitating a uniform quantification independent of clinical symptoms (Jack et al., 2018).

Translated into practice, the challenge of both quantifying and locating these biomarkers in-vivo can be overcome by using target-specific radiotracers in positron emission tomography (PET). This has been done both preclinically as well as in humans, e.g. with [18F]flutemetamol to aim at amyloid plaques or [18F]AV1451 to locate neurofibrillary tangles (Villemagne et al., 2018). With regards to PET targets representing neurodegeneration, studies in humans have so far taken advantage of the fact that degenerative processes are accompanied by reduced regional glucose metabolism, which is reflected by lower [18F] Fluorodesoxyglucose (FDG) uptake (Jack et al., 2018). In preclinical studies, however, FDG-PET delivered controversial results including hyper- and hypometabolism in AD mouse models (Bouter and Bouter, 2019). In this regard, neuroinflammation in transgenic mouse models was associated with increased glucose metabolism of astroglial immune cells (Choi et al., 2021; Xiang, 2021; Zimmer et al., 2017). This discrepancy between preclinical and human PET imaging results substantiates the need to identify alternative biomarkers for regional assessment of neurodegeneration in preclinical research, which could also translate to more reliable determination of regional neurodegeneration in humans. In the present study, we aimed to investigate the potential use of [18F]UCB-H as an alternative neurodegeneration biomarker of AD models. As a modification of the antiepileptic drug levetiracetam, this radiotracer specifically targets the synaptic vesicle glycoprotein 2A (SV2A), which is spread out ubiquitously in synaptic terminals across the brain (Rossi, 2022). Consequently, PET imaging of decreased [18F]UCB-H uptake facilitates the in-vivo visualization of synaptic decline in various neurodegenerative diseases. Here, previous preclinical as well as human studies have shown that decreases in [18F] UCB-H binding is congruent with synaptic loss in brain regions typically affected in AD (Xiong, 2021; Bastin et al., 2020).

On the basis of this observation, we sought to explore the synaptic loss representing the degenerative pathology in two distinct mouse models: one with amyloid-beta (PS2APP) and one with tau (P301S) pathology. Furthermore, we validated our in-vivo findings histologically by using immunostaining of SV2A in the same mouse cohort. Lastly, we also assessed the relationship between [18F]UCB-H and [18F]FDG binding in both mouse models and explored a potentially confounding influence by microglial activation in PS2APP transgenic mice.

2. Materials and methods

2.1. Radiochemistry

[18F]UCB-H was synthesized on a Trasis AllinOne (Ans, Belgium) automated synthesis unit (ASU) with 3 single-use disposable manifolds connected in series with a total of 18 valves. The manifolds were clamped into the correct position at the module. The software prompts were followed to run the cassette test. All reagents were assembled on the pre-defined positions of the manifold (position 2: eluent, position 8: precursor solution pre-mixed with TEMPO in MeCN, position 11: MeCN, position 12: saline bag, position 15: EtOH, position 16: sodium ascorbate) followed by HPLC priming and preliminary steps. No carrier added [18F]fluoride was produced via $^{18}O(p, n)^{18}F$ reaction by proton irradiation of ^{18}O-enriched water and delivered to the activity inlet reservoir. The precursor is labelled by replacement of the iodonium aryl triflate leaving group by [18F]fluoride in a S_NAr reaction. [18F]UCB-H is purified by reversed phase semi-preparative HPLC (Phenomenex Luna C18(2) column, 5 μm, 10 × 250 mm; isocratic elution with 61% (v/v) / 39% (v/v) acetonitrile; flow: 5 ml/min) and trapped on a SPE cartridge. The cartridge is rinsed and [18F]UCB-H is eluted with ethanol and saline. The formulated product solution was transferred to a dispenser and filtered through a Merck 0.22 μm Cathivex-GV sterile filter. The product was obtained in radiochemical yields of 32 ± 5.0 % non d.c. (n = 12) within a synthesis time of 55 min. The RCP was > 99%.

2.2. Animals

We used a total of 49 male transgenic mice in this study, 29 of which were homozygous B6.PS2APP (PS2APP) mice (Ozmen et al., 2009), while the other 20 belonged to a homozygous P301S mutant strain (Allen et al., 2002). Furthermore, 12 male C57Bl/6 wild-type (WT) mice were used as a control group. More detailed information on each mouse model is provided in the Supplementary Material. All animals were exposed to a 12 h: 12 h light–dark cycle and their housing environment was assured to maintain room temperature and approximately 50% humidity. Food and water were provided in standard pellets with unrestricted access (Ssniff, Soest, Germany).

2.3. Small-Animal PET

2.3.1. Study Overview

The preclinical procedure was approved by the local animal care committee of the Government of Upper Bavaria. All experiments were conducted on the basis of the National Guidelines for Animal Protection and constantly supervised by a veterinarian. Small-animal PET scans with [18F]UCB-H were carried out dynamically 0–60 min after radiotracer injection via a tail vein (14.7 ± 1.5 MBq). A detailed overview of each groups' characteristics is given in Table 1. Additional static [18F] FDG PET scans (30–60 min p.i.) were performed on a subset of transgenic and wild-type mice. All mice were deprived of food at least two hours before scanning and blood glucose levels were measured prior to each PET scan. These showed no significant difference between P301S (4 m: 150 ± 26 mg/dL; 8 m: 156 ± 17 mg/dL) and PS2APP mice (4 m: 137 ± 15 mg/dL; 7 m: 134 ± 9 mg/dL; 13 m: 137 ± 12 mg/dL; 19 m: 131 ± 11 mg/dL) when compared to wild-type controls (145 ± 16 mg/dL), irrespective of the age. For more details on the scanning procedure, we refer to our previous study (Xiang, 2021). Furthermore, a subset of PS2APP mice (n = 18) received a third scan with [18F]GE180 60–90 min after injection. Once the final PET scan was accomplished, all mice were anaesthetized and perfused with phosphate-buffered saline. To conduct immunohistochemical analysis, the brain was preserved using paraformaldehyde 4%.

Table 1
Overview of the cross-sectional quantitative SV2A analysis. Small-animal PET V_T ratios are shown for [^{18}F]UCB-H. Significant differences in PS2APP and P301S mice versus wild-type controls are indicated by *$P \leq 0.05$; **$P \leq 0.01$; ***$P \leq 0.001$.

Mouse Model	Age (mo)	[^{18}F]UCB-H Small Animal PET (n)	Cerebellum [^{18}F]UCB-H signal ($V_{Tr\ CB}$)	Brainstem [^{18}F]UCB-H signal ($V_{Tr\ BS}$)	Temporal Lobe [^{18}F]UCB-H signal ($V_{Tr\ TL}$)
PS2APP	4.4	5	0.72 ± 0.05	0.76 ± 0.02	0.88 ± 0.04
	7.1	7	0.69 ± 0.09	0.74 ± 0.05	0.87 ± 0.07
	13.5	10	0.62 ± 0.05***	0.74 ± 0.02	0.79 ± 0.07**
	19.8	7	0.60 ± 0.05***	0.74 ± 0.01	0.77 ± 0.06**
P301S	4.3	6	0.66 ± 0.05*	0.70 ± 0.03**	0.80 ± 0.09
	8.4	14	0.65 ± 0.05**	0.71 ± 0.02**	0.80 ± 0.08*
WT	12.7	12	0.75 ± 0.08	0.75 ± 0.04	0.90 ± 0.10

2.3.2. PET data Acquisition, reconstruction and analysis

For all PET data acquisition, reconstruction, and image pre-processing were conducted according to an established, standardized protocol (Overhoff, 2016). The PET analyses were performed using PMOD (v3.5, PMOD technologies, Basel, Switzerland). As part of the PET data quantification, we first defined the temporal lobe, cerebellum, and brainstem as three target regions of interest. Both the cerebellum and brainstem volume-of-interest (VOI) were drawn from the standardized Mirrione atlas (Ma et al., 2005). A predefined VOI of the temporal lobe was created as a subregion of the Mirrione cortex VOI (Supplemental Fig. S1). Standardized uptake values (SUV) for [^{18}F]UCB-H and [^{18}F]GE180 (60–90 min p.i.) as well as [^{18}F]FDG (30–60 min p.i.) were calculated for the static late-phase time. In addition, volumes-of-distribution (V_T) were computed for [^{18}F]UCB-H image data on the basis of an image derived input function (IDIF), as has been described by Logan et al. (Logan et al., 1990). For this purpose, we obtained a blood input curve from a standardized VOI of the left ventricle (3 mm) with a maximum error tolerance of 10% and a threshold of 0. No corrections for radiometabolites were applied. However, according to a recent study conducted by Goutal et al. in 2021 (Goutal et al., 2021), the metabolite-corrected plasma input function as well as the plasma to whole-blood ratio of [^{18}F]UCB-H SUV has been shown to be stable both within and between non-human primates. We therefore assumed a stable metabolization across all models and ages.

2.4. Immunohistochemistry and synaptic puncta analysis

Post-mortem mouse brain processing was performed as described elsewhere (Xiang, 2021; Briel et al., 2021). In brief, parasagittal slices were cut from paraformaldehyde-fixed hemispheres at 50 μm thickness using a VT1000S vibratome (Leica, Germany). From each animal 2–3 free-floating slices were stained immunofluorescently for SV2A. The protocol included permeabilization (2% Triton X-100 in PBS) and blocking (10% normal goat serum) steps before incubation with diluted primary antibodies (SV2A; 1:200, #ab32942; Abcam, Germany). After several washing steps secondary antibody goat anti-rabbit Alexa-Flour®488 (1:1000, #A11008; Thermo Fisher Scientific, Germany) was applied. DAPI (1:1000, #D9542; Sigma-Aldrich, Germany) was used as nuclei counterstain. Slides were mounted on Superfrost-plus® slides (Thermo Fisher Scientific, Germany) with Fluorescence Mounting Medium (#S302380-2, Agilent Dako, Germany) and covered with #1.5H high-precision imaging glass coverslips (#48393-059, VWR, Germany).

Synapse imaging has also already been described in previous studies (Xiang, 2021; Briel et al., 2021). In brief, a Zeiss LSM780 confocal system (Zeiss, Germany) with Plan-Apochromat 40X (NA 1.4, DIC M27, oil immersion) objective was used. At constant settings, across 2–3 slices per animal 5–9 high-resolution images (image depth = 16-bit, dpi = 2048) of size (101.21×101.21) μm^2 from the Somatosensory Cortex, Layers II/III, (75.87×75.87) μm^2 from the hippocampal CA1, Stratum radiatum (PS2/APP cohort), the medial vestibular nucleus (VM) located

in the brainstem and the nucleus interpositus of the cerebellum, and (48.87×75.87) μm^2 from the hippocampal CA1, Stratum radiatum (P301S cohort) were sampled randomly. Image processing was automized with custom IJ2 macros in Fiji/ImageJ, including background subtraction, thresholding, and 'Analyze Particles' for puncta metrics.

2.5. Statistics

For each target VOI, a Shapiro-Wilk test was computed to test for normality of the data, followed by a Bartlett test to check for homogeneity of variances. When both tests proved insignificant across all target regions, multivariate group comparisons for each mouse model were carried out using a one-way ANOVA with post-hoc Tukey adjustment. If normal distribution and homogeneity of variances was not met, a Kruskal-Wallis Test followed by post-hoc pairwise Wilcoxon-Mann-Whitney-tests was computed. A p-value of 0.05 or less was considered significant. Furthermore, we explored the association between the [^{18}F]UCB-H and [^{18}F]FDG signal as well as [^{18}F]FDG and [^{18}F]GE180 uptake in a subset of mice by means of Pearson's correlation coefficients and linear regression. All descriptive and inference statistics were computed using R Core Team (2022).
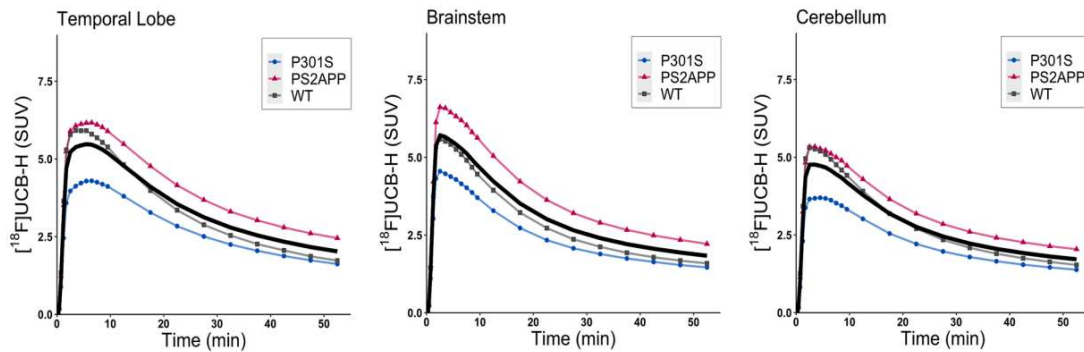
3. Results

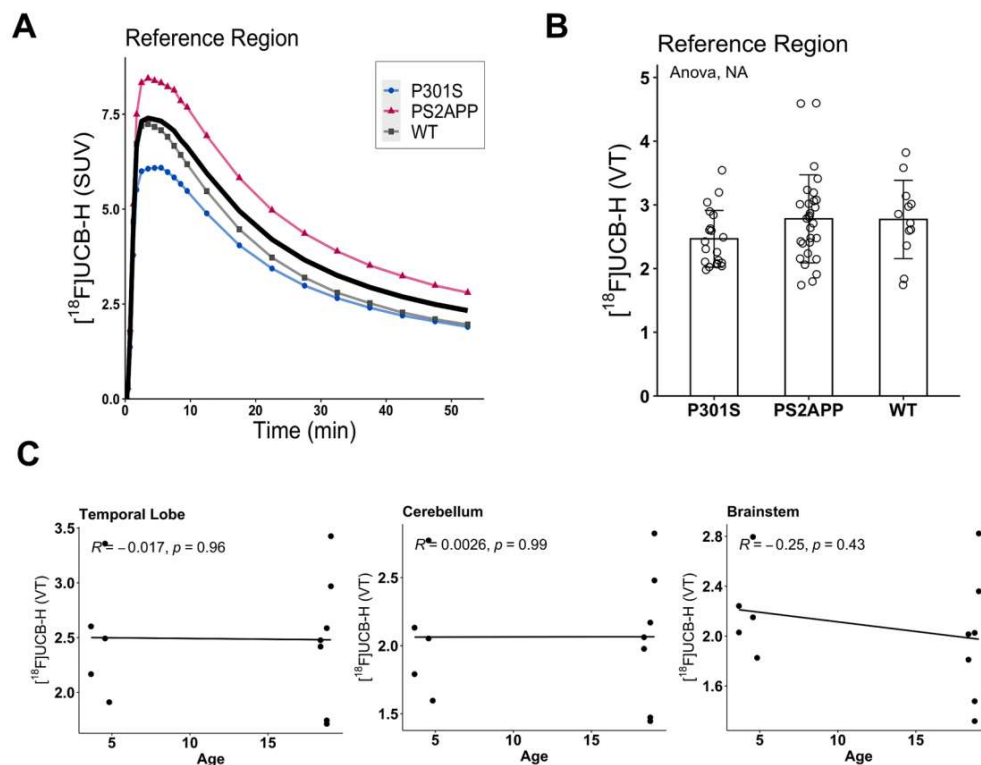### 3.1. [^{18}F]UCB-H tracer kinetics indicate rapid influx and washout from brain parenchyma

Averaged [^{18}F]UCB-H time activity curves (0–60 min) of standardized uptake values (SUV) for each genotype and region of interest showed an influx peak after about five minutes post injection. This was followed by a continuous decline in radioactive signaling corresponding to a fast tracer washout from the regional brain tissue (Fig. 1).

3.2. Low variability of [^{18}F]UCB-H uptake in the upper midbrain region suggests suitability as a pseudoreference region

First, we computed V_T images with IDIF to allow unbiased assessment of SV2A quantification across the brain. Exploratory analyses of [^{18}F]UCB-H binding in VOIs predefined by the Mirrione atlas revealed least variation of uptake in an upper midbrain region, dominantly composed of white matter (CoV = 22.6%), across all investigated mouse models and wild-type mice. Pairwise comparisons of corresponding V_T values using Bonferroni-corrected t-tests showed no significant differences between PS2APP, P301S and wild-type mice for any age-related cohort (Fig. 2B and Supplemental Table S1). Additionally, an intra-cohort ANOVA of the PS2APP strain as well as t-tests of the respective P301S and wild-type cohorts also did not show any significant differences in the VT signal of this region between the different age groups (PS2APP: p = 0.11; P301S: p = 0.37; WT: p = 0.19). Consequently, we selected the upper midbrain region as a pseudoreference tissue for the

Fig. 1. Time activity curves (TAC) of [^{18}F]UCB-H (SUV) showed a similar influx peak after approximately five minutes followed by a continuous washout of the radiotracer in all three target regions. Mean TAC across all cohorts is represented by a black graph.

Fig. 2. (A) Time activity curves of the reference region (upper midbrain) for each cohort showed equivalent kinetic features when compared to target regions. **(B)** Multivariate statistics (ANOVA) revealed no significant differences in [^{18}F]UCB-H binding in the reference region across all three cohorts. **(C)** Scatter plots show no significant correlations between age and [^{18}F]UCB-H binding (V_T) in the wild-type cohort across all target regions.

computation of V_T ratios in further quantitative comparisons. Furthermore, no significant correlations were found between [^{18}F]UCB-H uptake (V_T) and age in the wild-type cohort (Fig. 2C). Therefore, all wild-type mice were pooled into a larger and more robust control sample.
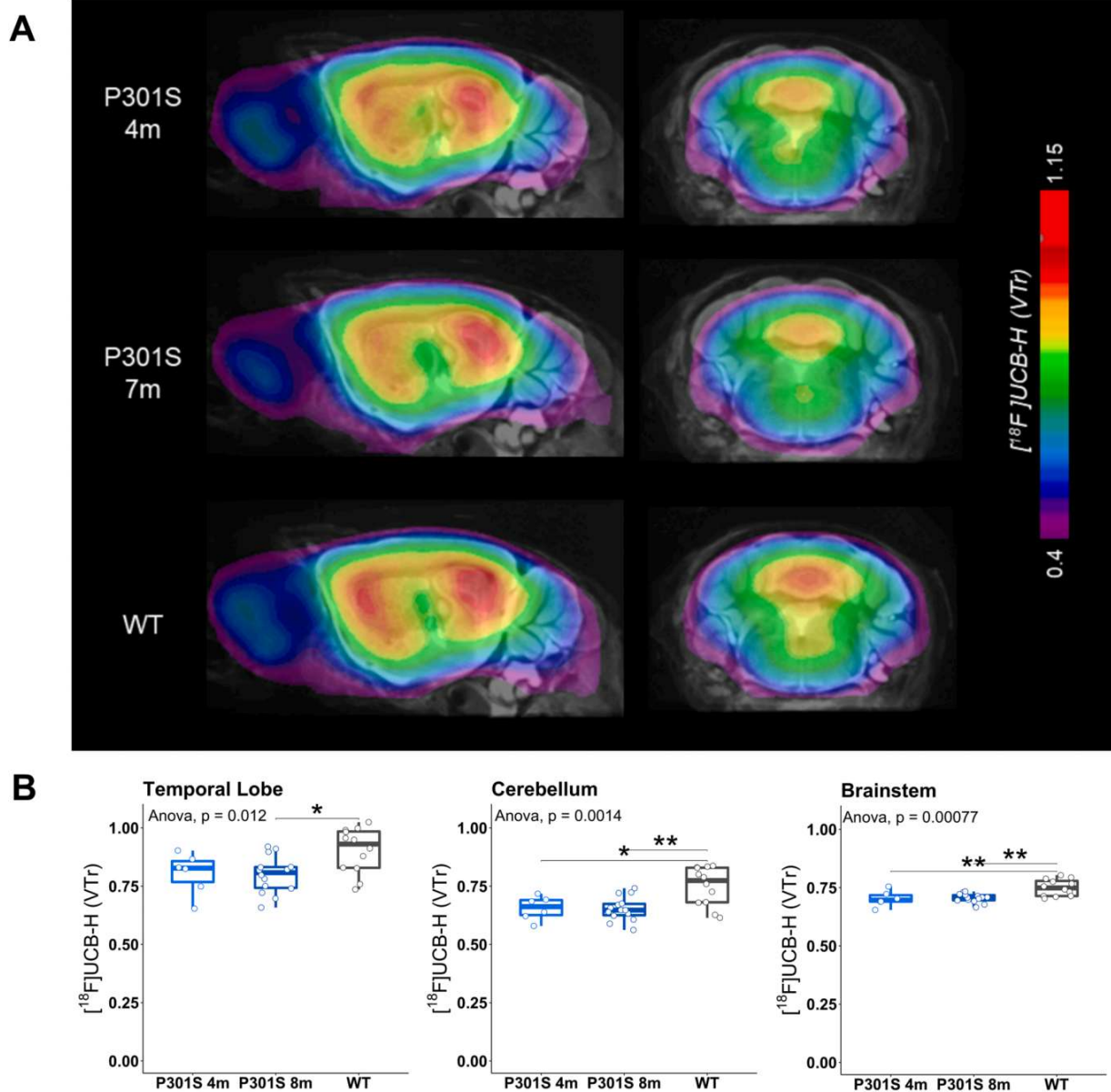
3.3. Reduced [^{18}F]UCB-H uptake portrays progressive synaptic loss in PS2APP and P301S mice

To test whether there were statistically significant differences in [^{18}F]UCB-H binding across the target regions of transgenic models, we next conducted multivariate analyses with post-hoc pairwise comparisons of V_T ratio values referenced to the upper midbrain region. By

means of validation, we also performed regression analyses on the V_T ratio and distribution volume ratios (DVR) values of all target regions across all mice which revealed a very high correlation between the two parameters ($R = 0.95$, $p < 2.2\text{e-}16$; Supplemental Fig. S2). Both young and old P301S mice showed significantly lower tracer binding than wild-type mice in the cerebellum (4 m vs. WT: $p = 0.018$; 8 m vs. WT: $p = 0.0018$; Fig. 3) and the brainstem (4 m vs. WT: $p = 0.0076$; 8 m vs. WT: $p = 0.0014$; Fig. 3). Additionally, a significantly decreased [^{18}F]UCB-H binding in the temporal lobe was found in 8-months old P301S mice when compared to wild-type controls ($p = 0.014$).

With regards to the PS2APP model, significantly reduced [^{18}F]UCB-H binding was detected in the temporal lobe of both 13-months ($p =$

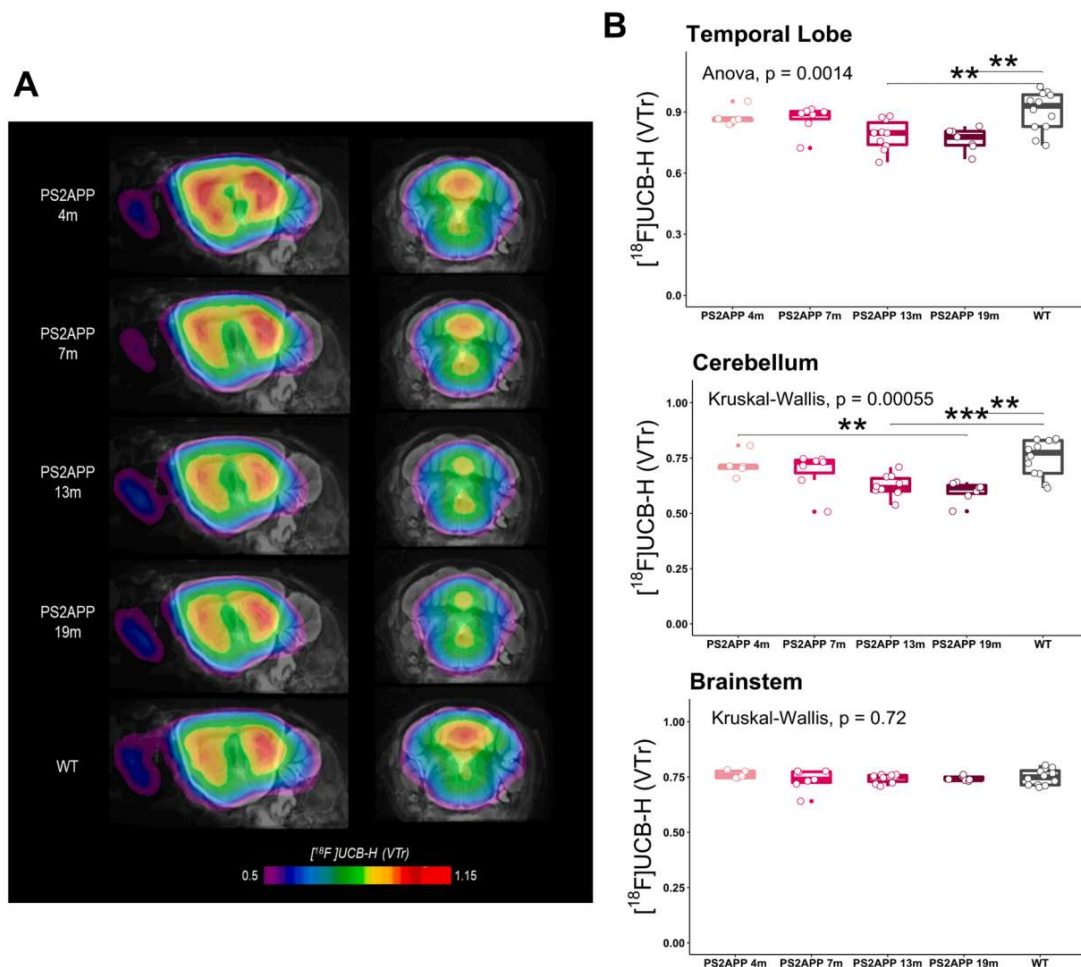**Fig. 3. (A)** Coronal sections of averaged [^{18}F]UCB-H images (V_T ratios) show all target regions projected onto a standard MRI atlas for both groups of P301S transgenic mice and wild-type controls. **(B)** Boxplots of [^{18}F]UCB-H binding (V_T ratios) across both groups of P301S mice showed significant SV2A reductions in all target regions when compared to wild-type controls. $*p \leq 0.05$; $**p \leq 0.01$; $***p \leq 0.001$.

0.0080) and 19-months (p = 0.0042) old mice when compared to wild-type controls (Fig. 4). As the data did not allow for parametric comparisons, non-parametric Kruskal-Wallis tests were computed for the brainstem and cerebellum in PS2APP mice. Post-hoc pairwise Wilcoxon-tests revealed significantly lower [^{18}F]UCB-H binding in 13-months (p = 0.006) and 19-months (p = 0.011) old PS2APP as opposed to wild-type mice in the cerebellum (Fig. 4). Brainstem V_T ratios did not show any significant differences between PS2APP and wild-type mice. With regards to the younger PS2APP cohorts (4 m, 7 m), no significant differences in V_T ratios were found in neither of the three target regions.

3.4. Synaptic loss is confirmed by immunohistochemical staining pattern in both PS2APP and P301S mice compared to wild-type controls

Immunohistochemical staining of SV2A was performed in the parieto-temporal cortex, the hippocampus, and the VM/NI as target regions of interest (Fig. 5A, B) (Institute, 2004) to evaluate the synaptic SV2A coverage and synaptic density in parallel to the PET results. A reduced synaptic SV2A coverage was observed in PS2APP mice when compared to wild-type controls in hippocampus (p = 0.0021) and parieto-temporal cortex (p = 0.002), and in P301S mice compared to wild-type controls in hippocampus (p = 2.3e-05) and VM/NI (p = 7e-09) (Fig. 5D). Similar results could be observed for synapse density of PS2APP mice when compared to wild-type controls in hippocampus (p

L. Vogler et al.

Fig. 4. (A) Coronal sections of averaged [^{18}F]UCB-H images (V$_T$ ratios) show all target regions projected onto a standard MRI atlas for all age groups of PS2APP transgenic mice and wild-type controls. **(B)** Boxplots of [^{18}F]UCB-H binding (V$_T$ ratios) across all ages of PS2APP mice indicate significant SV2A reductions in the temporal and cerebellar target regions when compared to wild-type controls. *$p \leq 0.05$; **$p \leq 0.01$; ***$p \leq 0.001$.

= 0.014) and parieto-temporal cortex (p = 0.0037) and in P301S mice compared to wild-type controls in hippocampus (p = 0.00025) and VM/NI (p = 4e-07) (Fig. 5E).

3.5. Reduced [^{18}F]UCB-H binding is associated with increased [^{18}F]FDG uptake in PS2APP mice
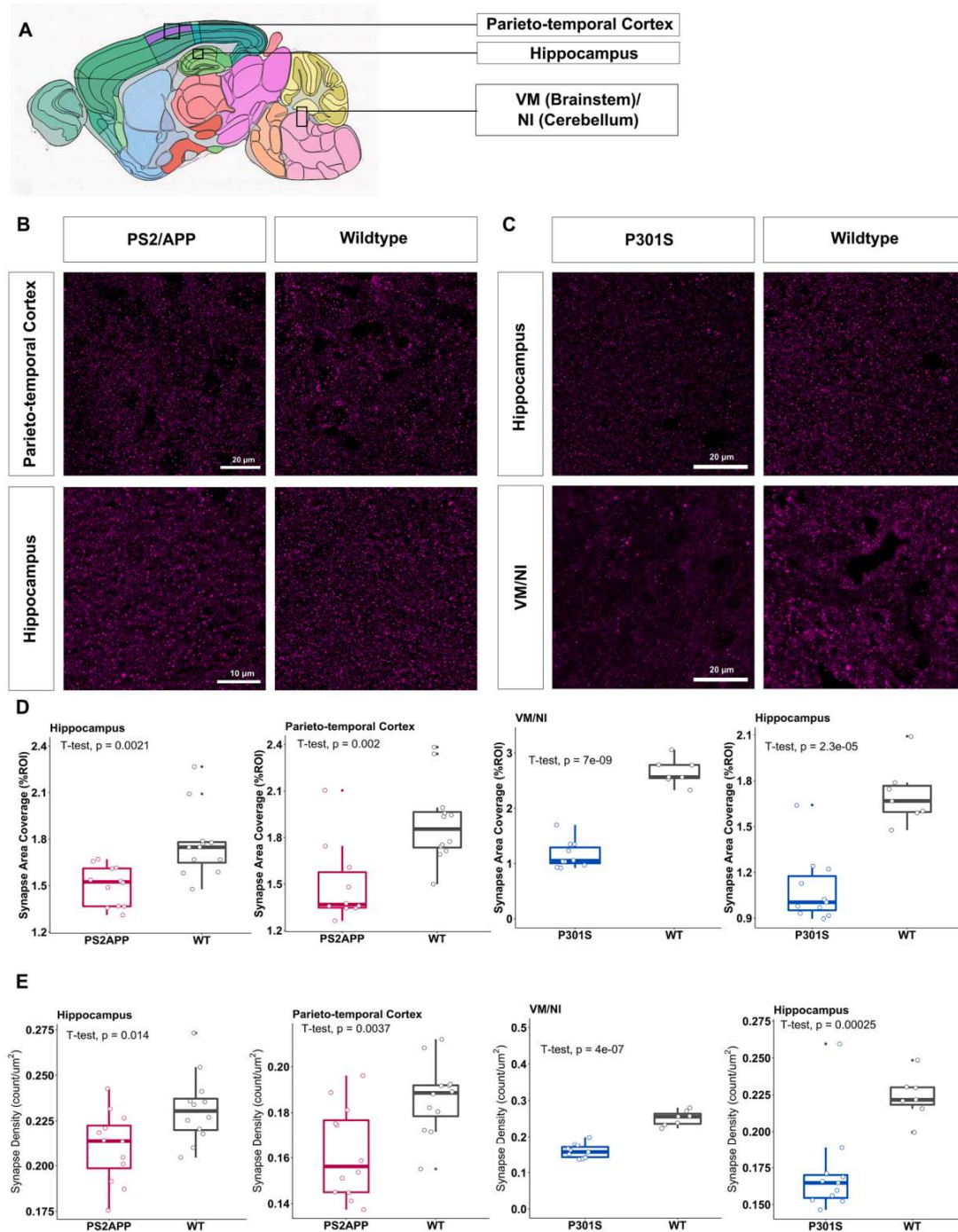
To test whether synaptic loss as expressed by reduced [^{18}F]UCB-H binding was associated with regional glucose metabolism, we calculated Pearson's coefficient of correlation for [^{18}F]UCB-H V$_T$ ratio and [^{18}F]FDG SUV across all target regions for both P301S and PS2APP genotypes (Table 2). As shown in Fig. 6A, no significant correlations between both biomarkers were found in the P301S model. However, there was a significant negative correlation between [^{18}F]UCB-H binding and [^{18}F]FDG uptake in the PS2APP cohort (R = − 0.26, p = 0.018), i.e. lower [^{18}F]UCB-H binding corresponded to elevated glucose metabolism. To further investigate a probable reason for this inverse relationship, we also calculated Pearson's correlation coefficient for [^{18}F]FDG and [^{18}F]GE180 SUV in the same PS2APP mice. Here, a positive relationship between the microglial signal and regional glucose metabolism was observed (Fig. 6B; R = 0.36, p = 0.008).

4. Discussion

The use of molecular imaging with PET in mouse models expressing specific disease-defining pathologies provides a unique opportunity to explore the precise interplay between different biomarkers. With regards to AD research, many radiotracers targeting amyloidosis and tau aggregates have already been well-established, contributing to a more detailed understanding of the temporal and spatial dynamics of the disease's pathomechanisms (Villemagne et al., 2018). However, using [^{18}F]FDG as a preclinical PET biomarker for neurodegeneration has so far yielded inconsistent data, thus driving the search for alternative molecular targets. In this study we investigated the capability to image progressive loss of synaptic density by means of [^{18}F]UCB-H in parallel to [^{18}F]FDG-related glucose metabolism in two distinct mouse models expressing major neuropathological characteristics of AD. This fluorine-18 labelled radiotracer selectively binds to the synaptic vesicle glycoprotein 2A and is therefore considered a surrogate biomarker for (pre-)synaptic density (Becker et al., 2020). Importantly, no on-site cyclotron is needed for [^{18}F]UCB-H to be used practically, thus making it an excellent candidate for broad clinical use.

Because SV2A is ubiquitously expressed throughout the entire brain, defining a proper reference region for the purpose of normalizing [^{18}F]

Fig. 5. (A) Overview of sagittal mouse brain highlighting the three brain regions of interest parieto-temporal cortex, hippocampus, and ventral medial nucleus/ nucleus interpositus (VM/NI) from the Allen Mouse Brain Atlas (https://atlas.brain-map.org/atlas). **(B, C)** Immunofluorescence signal of SV2A compared across the parieto-temporal cortex and hippocampus in the PS2APP cohort and across the VM/NI and hippocampus in the P301S cohort. **(D, E)** Boxplots of SV2A-positive synapse coverage respectively SV2A-positive synapse in the cortex, hippocampus, and VM/NI of PS2APP/ P301S transgenic mice, which showed significant reduction of both indices in transgenic mice when compared to wild-type controls.

Table 2
Overview of glucose uptake in the cross-sectional preclinical study. Small-animal PET SUVs are shown for $[^{18}F]$FDG.

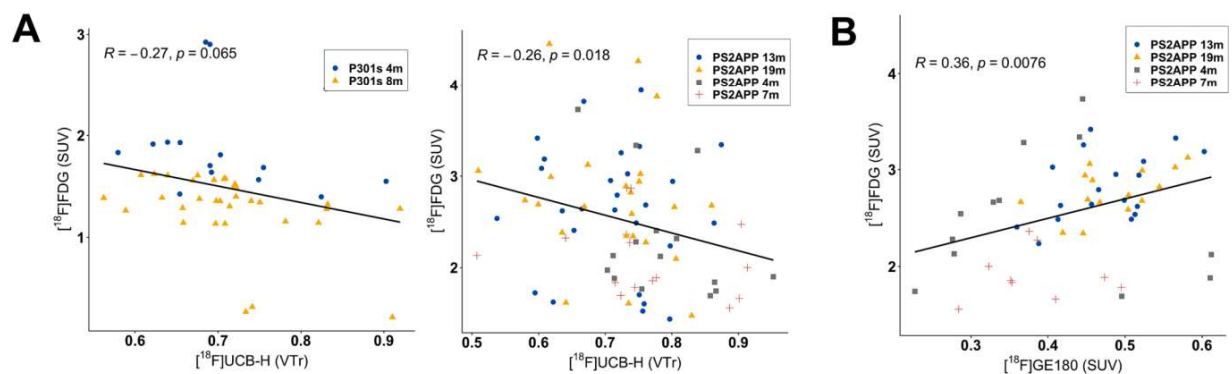| Mouse Model	Age (mo)	$[^{18}F]$FDG Small Animal Pet (n)	Cerebellum $[^{18}F]$FDG signal (SUV$_{CB}$)	Brainstem $[^{18}F]$FDG signal (SUV$_{BS}$)	Temporal Lobe $[^{18}F]$FDG signal (SUV$_{TL}$)
PS2APP	4.8	5	2.41 ± 0.76	2.38 ± 0.58	2.09 ± 0.67
	7.5	5	2.18 ± 0.44	2.26 ± 0.41	1.88 ± 0.37
	14.0	9	2.74 ± 0.73	2.75 ± 0.75	2.45 ± 0.65
	19.9	8	2.88 ± 0.80	2.80 ± 0.75	2.52 ± 0.68
P301S	4.8	4	1.83 ± 0.13	1.78 ± 0.11	1.48 ± 0.09
	7.4	10	1.49 ± 0.14	1.42 ± 0.14	1.26 ± 0.10
WT	4.7	6	1.60 ± 0.33	1.58 ± 0.27	1.43 ± 0.17

UCB-H data is not entirely possible (Serrano et al., 2019). We therefore sought to instead define a pseudoreference region which would express the least variability in $[^{18}F]$UCB-H uptake across all mouse models and target VOIs. Although the cerebellum is commonly used as a reference tissue in human studies of AD due to it being typically spared of amyloid debris (Chen et al., 2021), various preclinical observations have so far indicated considerable differences in cerebellar $[^{18}F]$FDG signal between transgenic and wild-type mice (Deleye et al., 2016). Therefore, other brain regions have been proposed for preclinical $[^{18}F]$UCB-H PET standardization, most commonly white matter regions with low specific binding characteristics such as the centrum semiovale (Nabulsi et al., 2016; Chen et al., 2018). However, reliably defining white matter regions in the mouse brain is quite challenging and hence prone to distortion. We therefore decided to base our reference tissue selection on statistical analyses of variation coefficients applied to predefined Mirrione atlas VOIs (Ma et al., 2005). To generate a robust area, we further combined upper midbrain VOIs with comparatively low variability and only few grey matter nuclei into one standardized reference VOI that we then used to quantify $[^{18}F]$UCB-H uptake by means of V_T ratios.

In P301S transgenic mice with pathological tau aggregation, our findings revealed significant decreases of $[^{18}F]$UCB-H uptake already at 4 months of age, which aggravated in 8-months old P301S mice when compared to wild-type controls. Decreases in synaptic density, as expressed by lower V_T ratio values, were found in all three target regions, i.e. the temporal lobe, brainstem and cerebellum at 8 months of age. These observations fit well with previous research causally linking neurotoxic tau aggregates to synaptic dysfunction and loss in AD models (Lasagna-Reeves, 2011) and primary tauopathies (Bigio et al., 2001; Briel et al., 2022). It is important to note, however, that this process presumably precedes the occurrence of the main pathological aggregate of tau, i.e. neurofibrillary tangles (NFTs), whose accumulation is strongly correlated with the onset and progression of clinical symptoms in humans (Arriagada et al., 1992; Long and Holtzman, 2019). In our study, this is particularly well illustrated in the P301S transgenic mouse

model, which already shows decreased $[^{18}F]$UCB-H signal by the age of 4 months in the cerebellum and brainstem. This finding is supported by previous studies observing synaptic impairment in 3-months old P301S mice long before the occurrence of NFTs at the age of 6 months (Yoshiyama et al., 2007). Taken together, this suggests that synaptic loss is a separate early entity of neurodegeneration which might facilitate preventive detection and timely intervention of AD-related pathomechanisms even before they manifest themselves clinically.

The second mouse model Included in this study represents another main feature of AD pathology, namely amyloidosis. Similar to our observations in P301S mice, we found significant reductions in $[^{18}F]$UCB-H signal in the temporal lobe and cerebellum, but not the brainstem, in both 13- and 19-months old transgenic mice when compared to wild-type controls. This shows that synaptic loss can not only triggered by neurotoxic tauopathy but also in presence of Aβ. In line, previous studies concluded that the accumulation of oligomeric forms of Aβ contribute to a reduction in synaptic density and function as well by directly targeting synaptic spines (Lacor, 2007; Lacor, 2004). Similar to tau oligomers and NFTs, this synapto-toxic form of Aβ is a separate entity to the insoluble amyloid plaques, whose presence is not directly related to synaptic decline (Einstein et al., 1994). Furthermore, our preclinical observations fit well with human studies, which found significantly reduced $[^{18}F]$UCB-H and $[^{11}C]$UCB-J tracer uptake in the median temporal lobe and more specifically the hippocampus of AD patients in comparison to heathy controls (Bastin et al., 2020; Chen et al., 2018). This synapse loss correlates strongly with cognitive decline in humans and is again supposed to occur even before the onset of amyloidosis, thus providing valuable insights into early disease stages (Scheff et al., 2006).

As part of our multi-tracer approach, we further compared the regional glucose metabolism in all target regions to previously mentioned quantitative $[^{18}F]$UCB-H uptake. We hypothesized that SV2A is a more specific biomarker of neuronal injury since glucose uptake in the brain is not restricted to neurons only but also driven by astroglial cells (Xiang, 2021; Zimmer et al., 2017). As a consequence, studies using

Fig. 6. (A) Scatter plots show a significant negative correlation between $[^{18}F]$UCB-H (V_T ratio) and $[^{18}F]$FDG (SUV) signal across all target regions in PS2APP mice. (B) A significant positive correlation was found between $[^{18}F]$FDG (SUV) and $[^{18}F]$GE180 (SUV) in the PS2APP cohort.

[^{18}F]FDG to measure hypometabolism observed that inflammatory glial cells infiltrating ischemic regions consume a disproportionate amount of glucose, thus distorting the actual extent of neurodegenerative decay (Backes et al., 2016). Contrary to previous findings (Endepols et al., 2022), we did not observe a significant positive association between glucose uptake and SV2A expression in either transgenic mice strain, but instead found that [^{18}F]UCB-H and [^{18}F]FDG signals were inversely associated with each other on a significant level in the PS2APP mouse strain while also showing a distinctly negative trajectory in the P301S strain. This finding might well be due to a signal distortion by glial cells colocalized to synaptic loss, which consume particularly high levels of glucose when in a functionally active state (Xiang, 2021). In line with our earlier findings (Brendel et al., 2016), we further found a significant correlation between [^{18}F]FDG and [^{18}F]GE180 in PS2APP mice, an observation which supports the stated hypothesis that increases of glucose uptake are linked to microglial activation. Further adding to this, a recently published clinical study also observed much more widespread synaptic loss than hypometabolism in extrastriatal areas of a cohort of patients with Huntington's Disease, thus concluding that [^{18}F]FDG is not as sensitive in detecting early changes in the disease's pathophysiology (Delva et al., 2022). In future preclinical research, it will be critical to further illuminate how glucose metabolism and synaptic decline are temporally and spatially linked to neuronal loss in order to justify the use of one or the other as a representative biomarker for neurodegeneration.

Several aspects should be mentioned as limitations for the interpretation of our results. First, a previous study has shown that P301S mice show generalized brain atrophy at 8 months of age, while synapse impairment was already detected at an even younger age of 3 months (Yoshiyama et al., 2007). Presence of atrophy needs to be considered for the interpretation of the SV2A-PET results in the P301S cohort since signal loss can be attributed to two reasons: synapse loss in the context of specific neurodegeneration and/or due to a general reduction of brain parenchyma. In this regard, we have not been able to perform a MRI-based partial volume effect correction in this study, so that we cannot rule out a signal interference through spill-over effects in particularly small volumes of interest. Missing PVE correction was also the reason for which we omitted the hippocampus as a target region as signal distortion due to the small size was to be expected. Furthermore, we have not been able to correct the image-derived input functions used in kinetic modelling for radiometabolites. A transfer of radiometabolite data from previous study results of non-human primates, to which we have referred in the methods section, is not entirely permissible since the metabolic profile of radiotracers can show considerable interspecies discrepancies. Future studies need to address radiometabolite analysis in mice and lacking radiometabolite data in this species need to be considered as a current limitation of [^{18}F]UCB-H. Finally, in the present study, we were unfortunately unable to perform a validation of the pseudoreference region at different ages by immunohistochemistry or immunoblotting. Thus, age-related reductions of SV2A in any pseudoreference tissue may limit the ability to detect small biological effects by relative SV2A-PET quantification in target tissues.

5. Conclusion

In-vivo PET imaging using [^{18}F]UCB-H reliably depicts progressive synaptic loss in two mouse models expressing the major characteristics of neurodegenerative disorders, i.e. tauopathy and beta-amyloid pathology. Due to distorting metabolic inconsistencies that have previously been observed with the use of [^{18}F]FDG, we therefore suggest that [^{18}F]UCB-H could be a more robust biomarker for neurodegeneration in preclinical AD research. As the onset of synapse loss is thought to occur even before other major pathological biomarkers, integrating [^{18}F]UCB-H into the diagnostic protocol could prospectively facilitate the detection and treatment monitoring in the earliest of disease stages of human patients.

Declaration of interest.

Johannes Levin reports speaker fees from Bayer Vital, Biogen and Roche, consulting fees from Axon Neuroscience and Biogen, author fees from Thieme medical publishers and W. Kohlhammer GmbH medical publishers. In addition, he reports compensation for serving as chief medical officer for MODAG GmbH, is beneficiary of the phantom share program of MODAG GmbH and is inventor in a patent "Pharmaceutical Composition and Methods of Use" (EP 22 159 408.8) filed by MODAG GmbH, all activities outside the submitted work.

Declaration of Competing Interest

The authors declare that they have no known competing financial interests or personal relationships that could have appeared to influence the work reported in this paper.

Data availability

Data will be made available on request.

Appendix A. Supplementary data

Supplementary data to this article can be found online at https://doi.org/10.1016/j.nicl.2023.103484.

References

Allen, B., Ingram, E., Takao, M., Smith, M.J., Jakes, R., Virdee, K., Yoshida, H., Holzer, M., Craxton, M., Emson, P.C., Atzori, C., Migheli, A., Crowther, R.A., Ghetti, B., Spillantini, M.G., Goedert, M., 2002. Abundant tau filaments and nonapoptotic neurodegeneration in transgenic mice expressing human P301S tau protein. J. Neurosci. 22 (21), 9340–9351.

Arriagada, P.V., Growdon, J.H., Hedley-Whyte, E.T., Hyman, B.T., 1992. Neurofibrillary tangles but not senile plaques parallel duration and severity of Alzheimer's disease. Neurology 42 (3), 631–639.

Backes, H., Walberer, M., Ladwig, A., Rueger, M.A., Neumaier, B., Endepols, H., Hoehn, M., Fink, G.R., Schroeter, M., Graf, R., 2016. Glucose consumption of inflammatory cells masks metabolic deficits in the brain. Neuroimage 128, 54–62.

Bastin, C., Bahri, M.A., Meyer, F., Manard, M., Delhaye, E., Plenevaux, A., Becker, G., Seret, A., Mella, C., Giacomelli, F., Degueldre, C., Balteau, E., Luxen, A., Salmon, E., 2020. In vivo imaging of synaptic loss in Alzheimer's disease with [18F]UCB-H positron emission tomography. Eur. J. Nucl. Med. Mol. Imaging 47 (2), 390–402.

Becker, G., Dammicco, S., Bahri, M.A., Salmon, E., 2020. The rise of synaptic density pet imaging. Molecules 25 (10), 2303.

Bigio, E.H., Vono, M.B., Satumtira, S., Adamson, J., Sontag, E., Hynan, L.S., White, C.L., Baker, M., Hutton, M., 2001. Cortical synapse loss in progressive supranuclear palsy. J. Neuropathol. Exp. Neurol. 60 (5), 403–410.

Bouter, C., Bouter, Y., 2019. (18)F-FDG-PET in mouse models of alzheimer's disease. Front Med (Lausanne) 6, 71.

Brendel, M., Probst, F., Jaworska, A., Overhoff, F., Korzhova, V., Albert, N.L., Beck, R., Lindner, S., Gildehaus, F.-J., Baumann, K., Bartenstein, P., Kleinberger, G., Haass, C., Herms, J., Rominger, A., 2016. Glial activation and glucose metabolism in a transgenic amyloid mouse model: a triple-tracer pet study. J. Nucl. Med. 57 (6), 954–960.

Briel, N., Pratsch, K., Roeber, S., Arzberger, T., Herms, J., 2021. Contribution of the astrocytic tau pathology to synapse loss in progressive supranuclear palsy and corticobasal degeneration. Contribution of the astrocytic tau pathology to synapse loss in progressive supranuclear palsy and corticobasal degeneration. 31 (4), e12914.

Briel, N., Ruf, V.C., Pratsch, K., Roeber, S., Widmann, J., Mielke, J., Dorostkar, M.M., Windl, O., Arzberger, T., Herms, J., Struebing, F.L., 2022. Single-nucleus chromatin

accessibility profiling highlights distinct astrocyte signatures in progressive supranuclear palsy and corticobasal degeneration. Acta Neuropathol. 144 (4), 615–635.

Chen, M.-K., Mecca, A.P., Naganawa, M., Finnema, S.J., Toyonaga, T., Lin, S.-F., Najafzadeh, S., Ropchan, J., Lu, Y., McDonald, J.W., Michalak, H.R., Nabulsi, N.B., Arnsten, A.F.T., Huang, Y., Carson, R.E., van Dyck, C.H., 2018. Assessing synaptic density in alzheimer disease with synaptic vesicle glycoprotein 2a positron emission tomographic imaging. JAMA Neurol. 75 (10), 1215.

Chen, M.-K., Mecca, A.P., Naganawa, M., Gallezot, J.-D., Toyonaga, T., Mondal, J., Finnema, S.J., Lin, S.-F., O'Dell, R.S., McDonald, J.W., Michalak, H.R., Vander Wyk, B., Nabulsi, N.B., Huang, Y., Arnsten, A.F.T., van Dyck, C.H., Carson, R.E., 2021. Comparison of [(11)C]UCB-J and [(18)F]FDG PET in Alzheimer's disease: a tracer kinetic modeling study. J. Cereb. Blood Flow Metab. 41 (9), 2395–2409.

Choi, H., Choi, Y., Lee, E.J., Kim, H., Lee, Y., Kwon, S., Hwang, D.W., Lee, D.S., 2021. Hippocampal glucose uptake as a surrogate of metabolic change of microglia in Alzheimer's disease. J. Neuroinflammation 18 (1).

S. Deleye A.-M. Waldron J.C. Richardson M. Schmidt X. Langlois S. Stroobants S. Staelens The Effects of Physiological and Methodological Determinants on 18F-FDG Mouse Brain Imaging Exemplified in a Double Transgenic Alzheimer Model Mol Imaging 15 2016 153601211562491.

Delva, A., Michiels, L., Koole, M., Van Laere, K., Vandenberghe, W., 2022. Synaptic damage and its clinical correlates in people with early huntington disease: a pet study. Neurology 98 (1), e83–e94.

Einstein, G., Buranosky, R., Crain, B.J., 1994. Dendritic pathology of granule cells in Alzheimer's disease is unrelated to neuritic plaques. J. Neurosci. 14 (8), 5077–5088.

Endepols, H., Anglada-Huguet, M., Mandelkow, E., Schmidt, Y., Krapf, P., Zlatopolskiy, B.D., Neumaier, B., Mandelkow, E.-M., Drzezga, A., 2022. Assessment of the in vivo relationship between cerebral hypometabolism, tau deposition, tspo expression, and synaptic density in a tauopathy mouse model: a multi-tracer pet study. Mol. Neurobiol. 59 (6), 3402–3413.

Goutal, S., Guillermier, M., Becker, G., Gaudin, M., Bramoullé, Y., Luxen, A., Lemaire, C., Plenevaux, A., Salmon, E., Hantraye, P., Barret, O., Van Camp, N., 2021. The pharmacokinetics of [(18)F]UCB-H revisited in the healthy non-human primate brain. EJNMMI Res. 11 (1).

Allen Institute for Brain Science. 2004; https://atlas.brain-map.org/atlas]. Available from: https://atlas.brain-map.org/atlas.

Jack, C.R., Knopman, D.S., Jagust, W.J., Shaw, L.M., Aisen, P.S., Weiner, M.W., Petersen, R.C., Trojanowski, J.Q., 2010. Hypothetical model of dynamic biomarkers of the Alzheimer's pathological cascade. The Lancet Neurology 9 (1), 119–128.

Jack, C.R., Bennett, D.A., Blennow, K., Carrillo, M.C., Dunn, B., Haeberlein, S.B., Holtzman, D.M., Jagust, W., Jessen, F., Karlawish, J., Liu, E., Molinuevo, J.L., Montine, T., Phelps, C., Rankin, K.P., Rowe, C.C., Scheltens, P., Siemers, E., Snyder, H.M., Sperling, R., Elliott, C., Masliah, E., Ryan, L., Silverberg, N., 2018. NIA-AA research framework: toward a biological definition of Alzheimer's disease. Alzheimers Dement. 14 (4), 535–562.

Kitazawa, M., Yamasaki, T.R., LaFerla, F.M., 2004. Microglia as a potential bridge between the amyloid beta-peptide and tau. Ann. N. Y. Acad. Sci. 1035, 85–103.

Lacor, P.N., et al., 2004. Synaptic targeting by Alzheimer's-related amyloid beta oligomers. J. Neurosci. 24 (45), 10191–10200.

Lacor, P.N., et al., 2007. Abeta oligomer-induced aberrations in synapse composition, shape, and density provide a molecular basis for loss of connectivity in Alzheimer's disease. J. Neurosci. 27 (4), 796–807.

Lasagna-Reeves, C.A., et al., 2011. Tau oligomers impair memory and induce synaptic and mitochondrial dysfunction in wild-type mice. Mol. Neurodegener. 6, 39.

Lemere, C.A., Masliah, E., 2010. Can Alzheimer disease be prevented by amyloid-beta immunotherapy? Nat. Rev. Neurol. 6 (2), 108–119.

Leng, F., Edison, P., 2021. Neuroinflammation and microglial activation in Alzheimer disease: where do we go from here? Nat. Rev. Neurol. 17 (3), 157–172.

Logan, J., Fowler, J.S., Volkow, N.D., Wolf, A.P., Dewey, S.L., Schlyer, D.J., MacGregor, R.R., Hitzemann, R., Bendriem, B., Gatley, S.J., Christman, D.R., 1990. Graphical analysis of reversible radioligand binding from time-activity measurements applied to [N-11C-methyl]-(-)-cocaine PET studies in human subjects. J. Cereb. Blood Flow Metab. 10 (5), 740–747.

Long, J.M., Holtzman, D.M., 2019. Alzheimer disease: an update on pathobiology and treatment strategies. Cell 179 (2), 312–339.

Ma, Y., Hof, P.R., Grant, S.C., Blackband, S.J., Bennett, R., Slatest, L., McGuigan, M.D., Benveniste, H., 2005. A three-dimensional digital atlas database of the adult C57BL/6J mouse brain by magnetic resonance microscopy. Neuroscience 135 (4), 1203–1215.

Nabulsi, N.B., Mercier, J., Holden, D., Carré, S., Najafzadeh, S., Vandergeten, M.-C., Lin, S.-F., Deo, A., Price, N., Wood, M., Lara-Jaime, T., Montel, F., Laruelle, M., Carson, R.E., Hannestad, J., Huang, Y., 2016. Synthesis and preclinical evaluation of 11c-ucb-j as a pet tracer for imaging the synaptic vesicle glycoprotein 2a in the brain. J. Nucl. Med. 57 (5), 777–784.

Overhoff, F., et al., 2016. Automated spatial brain normalization and hindbrain white matter reference tissue give improved [(18)f]-florbetaben pet quantitation in alzheimer's model mice. Front. Neurosci. 10, 45.

Ozmen, L., Albientz, A., Czech, C., Jacobsen, H., 2009. Expression of transgenic APP mRNA is the key determinant for beta-amyloid deposition in PS2APP transgenic mice. Neurodegener Dis 6 (1-2), 29–36.

Rossi, R., et al., 2022. Synaptic vesicle glycoprotein 2a: features and functions. Front. Neurosci. 16, 864514.

Scheff, S.W., Price, D.A., Schmitt, F.A., Mufson, E.J., 2006. Hippocampal synaptic loss in early Alzheimer's disease and mild cognitive impairment. Neurobiol. Aging 27 (10), 1372–1384.

Serrano, M.E., Bahri, M.A., Becker, G., Seret, A., Mievis, F., Giacomelli, F., Lemaire, C., Salmon, E., Luxen, A., Plenevaux, A., 2019. Quantification of [(18)F]UCB-H binding in the rat brain: from kinetic modelling to standardised uptake value. Mol. Imag. Biol. 21 (5), 888–897.

Villemagne, V.L., Doré, V., Burnham, S.C., Masters, C.L., Rowe, C.C., 2018. Imaging tau and amyloid-β proteinopathies in Alzheimer disease and other conditions. Nat. Rev. Neurol. 14 (4), 225–236.

X. Xiang et al. Microglial activation states drive glucose uptake and FDG-PET alterations in neurodegenerative diseases Sci Transl Med 13 615 2021 p. eabe5640.

Xiong, M., et al., 2021. In vivo imaging of synaptic density with [(11)C]UCB-J PET in two mouse models of neurodegenerative disease. Neuroimage 239, 118302.

Yoshiyama, Y., Higuchi, M., Zhang, B., Huang, S.-M., Iwata, N., Saido, T., Maeda, J., Suhara, T., Trojanowski, J.Q., Lee, V.-Y., 2007. Synapse loss and microglial activation precede tangles in a P301S tauopathy mouse model. Neuron 53 (3), 337–351.

Zimmer, E.R., Parent, M.J., Souza, D.G., Leuzy, A., Lecrux, C., Kim, H.-I., Gauthier, S., Pellerin, L., Hamel, E., Rosa-Neto, P., 2017. [(18)F]FDG PET signal is driven by astroglial glutamate transport. Nat. Neurosci. 20 (3), 393–395.

7. Literaturverzeichnis

1. Alzheimer Forschung Initiative e.V. (AFI). Was ist Alzheimer? Die Alzheimer-Krankheit: AFI; 2023 [Available from: https://www.alzheimer-forschung.de/alzheimer/.

2. Ziegler-Graham K, Brookmeyer R, Johnson E, Arrighi HM. Worldwide variation in the doubling time of Alzheimer's disease incidence rates. Alzheimers Dement. 2008;4(5):316-23.

3. World Health Organization. Dementia: WHO; 2023 [Available from: https://www.who.int/news-room/fact-sheets/detail/dementia.

4. Statistisches Bundesamt (Destatis). Krankheiskosten für Demenz: Destatis; 2022 [Available from: https://www-genesis.destatis.de/genesis/online?operation=previous&levelindex=1&step=1&titel=Ergebnis&levelid=1691311591065&acceptscookies=false#abreadcrumb.

5. Weller J, Budson A. Current understanding of Alzheimer's disease diagnosis and treatment. F1000Res. 2018;7.

6. Howard R, McShane R, Lindesay J, Ritchie C, Baldwin A, Barber R, et al. Donepezil and memantine for moderate-to-severe Alzheimer's disease. N Engl J Med. 2012;366(10):893-903.

7. Vitek GE, Decourt B, Sabbagh MN. Lecanemab (BAN2401): an anti-beta-amyloid monoclonal antibody for the treatment of Alzheimer disease. Expert Opin Investig Drugs. 2023;32(2):89-94.

8. Mullard A. FDA approves second anti-amyloid antibody for Alzheimer disease. Nat Rev Drug Discov. 2023;22(2):89.

9. Biechele G, Blume T, Deussing M, Zott B, Shi Y, Xiang X, et al. Pre-therapeutic microglia activation and sex determine therapy effects of chronic immunomodulation. Theranostics. 2021;11(18):8964-76.

10. Jack CR, Jr., Bennett DA, Blennow K, Carrillo MC, Feldman HH, Frisoni GB, et al. A/T/N: An unbiased descriptive classification scheme for Alzheimer disease biomarkers. Neurology. 2016;87(5):539-47.

11. Hardy JA, Higgins GA. Alzheimer's disease: the amyloid cascade hypothesis. Science. 1992;256(5054):184-5.

12. Jack CR, Knopman DS, Jagust WJ, Shaw LM, Aisen PS, Weiner MW, et al. Hypothetical model of dynamic biomarkers of the Alzheimer's pathological cascade. The Lancet Neurology. 2010;9(1):119-28.

13. Lemere CA, Masliah E. Can Alzheimer disease be prevented by amyloid-beta immunotherapy? Nat Rev Neurol. 2010;6(2):108-19.

14. Hampel H, Cummings J, Blennow K, Gao P, Jack CR, Jr., Vergallo A. Developing the ATX(N) classification for use across the Alzheimer disease continuum. Nat Rev Neurol. 2021;17(9):580-9.

15. Heneka MT, Kummer MP, Latz E. Innate immune activation in neurodegenerative disease. Nat Rev Immunol. 2014;14(7):463-77.

16. Pasqualetti G, Brooks DJ, Edison P. The role of neuroinflammation in dementias. Curr Neurol Neurosci Rep. 2015;15(4):17.

17. González-Reyes RE, Nava-Mesa MO, Vargas-Sánchez K, Ariza-Salamanca D, Mora-Muñoz L. Involvement of Astrocytes in Alzheimer's Disease from a Neuroinflammatory and Oxidative Stress Perspective. Front Mol Neurosci. 2017;10:427.

18. Rodriguez-Vieitez E, Ni R, Gulyás B, Tóth M, Häggkvist J, Halldin C, et al. Astrocytosis precedes amyloid plaque deposition in Alzheimer APPswe transgenic mouse brain: a correlative positron emission tomography and in vitro imaging study. Eur J Nucl Med Mol Imaging. 2015;42(7):1119-32.

19. Carter SF, Herholz K, Rosa-Neto P, Pellerin L, Nordberg A, Zimmer ER. Astrocyte Biomarkers in Alzheimer's Disease. Trends Mol Med. 2019;25(2):77-95.

20. Liddelow SA, Barres BA. Reactive Astrocytes: Production, Function, and Therapeutic Potential. Immunity. 2017;46(6):957-67.

21. Freeman MR. Specification and morphogenesis of astrocytes. Science. 2010;330(6005):774-8.

22. Verkhratsky A, Nedergaard M. Physiology of Astroglia. Physiol Rev. 2018;98(1):239-389.

23. Escartin C, Galea E, Lakatos A, O'Callaghan JP, Petzold GC, Serrano-Pozo A, et al. Reactive astrocyte nomenclature, definitions, and future directions. Nat Neurosci. 2021;24(3):312-25.

24. Liddelow S, Barres B. SnapShot: Astrocytes in Health and Disease. Cell. 2015;162(5):1170-.e1.

25. Anderson MA, Burda JE, Ren Y, Ao Y, O'Shea TM, Kawaguchi R, et al. Astrocyte scar formation aids central nervous system axon regeneration. Nature. 2016;532(7598):195-200.

26. Liddelow SA, Guttenplan KA, Clarke LE, Bennett FC, Bohlen CJ, Schirmer L, et al. Neurotoxic reactive astrocytes are induced by activated microglia. Nature. 2017;541(7638):481-7.

27. Eng LF, Ghirnikar RS, Lee YL. Glial fibrillary acidic protein: GFAP-thirty-one years (1969-2000). Neurochem Res. 2000;25(9-10):1439-51.

28. Tipton KF, Davey G, Motherway M. Monoamine oxidase assays. Curr Protoc Pharmacol. 2001;Chapter 3:Unit3.6.

29. Gaweska H, Fitzpatrick PF. Structures and Mechanism of the Monoamine Oxidase Family. Biomol Concepts. 2011;2(5):365-77.

30. Harada R, Furumoto S, Kudo Y, Yanai K, Villemagne VL, Okamura N. Imaging of Reactive Astrogliosis by Positron Emission Tomography. Front Neurosci. 2022;16:807435.

31. Levitt P, Pintar JE, Breakefield XO. Immunocytochemical demonstration of monoamine oxidase B in brain astrocytes and serotonergic neurons. Proceedings of the National Academy of Sciences of the United States of America. 1982;79(20):6385-9.

32. Tong J, Rathitharan G, Meyer JH, Furukawa Y, Ang LC, Boileau I, et al. Brain monoamine oxidase B and A in human parkinsonian dopamine deficiency disorders. Brain. 2017;140(9):2460-74.

33. Selkoe DJ. Alzheimer's disease is a synaptic failure. Science. 2002;298(5594):789-91.

34. Carson RE, Naganawa M, Toyonaga T, Koohsari S, Yang Y, Chen MK, et al. Imaging of Synaptic Density in Neurodegenerative Disorders. J Nucl Med. 2022;63(Suppl 1):60s-7s.

35. DeKosky ST, Scheff SW. Synapse loss in frontal cortex biopsies in Alzheimer's disease: correlation with cognitive severity. Ann Neurol. 1990;27(5):457-64.

36. Bajjalieh SM, Peterson K, Shinghal R, Scheller RH. SV2, a brain synaptic vesicle protein homologous to bacterial transporters. Science. 1992;257(5074):1271-3.

37. Buckley K, Kelly RB. Identification of a transmembrane glycoprotein specific for secretory vesicles of neural and endocrine cells. J Cell Biol. 1985;100(4):1284-94.

38. Bajjalieh SM, Frantz GD, Weimann JM, McConnell SK, Scheller RH. Differential expression of synaptic vesicle protein 2 (SV2) isoforms. J Neurosci. 1994;14(9):5223-35.

39. Lynch BA, Lambeng N, Nocka K, Kensel-Hammes P, Bajjalieh SM, Matagne A, et al. The synaptic vesicle protein SV2A is the binding site for the antiepileptic drug levetiracetam. Proc Natl Acad Sci U S A. 2004;101(26):9861-6.

40. Rossi R, Arjmand S, Baerentzen SL, Gjedde A, Landau AM. Synaptic Vesicle Glycoprotein 2A: Features and Functions. Front Neurosci. 2022;16:864514.

41. Drummond E, Wisniewski T. Alzheimer's disease: experimental models and reality. Acta Neuropathol. 2017;133(2):155-75.

42. Canevelli M, Piscopo P, Talarico G, Vanacore N, Blasimme A, Crestini A, et al. Familial Alzheimer's disease sustained by presenilin 2 mutations: systematic review of literature and genotype-phenotype correlation. Neurosci Biobehav Rev. 2014;42:170-9.

43. Teipel SJ, Buchert R, Thome J, Hampel H, Pahnke J. Development of Alzheimer-disease neuroimaging-biomarkers using mouse models with amyloid-precursor protein-transgene expression. Prog Neurobiol. 2011;95(4):547-56.

44. Richards JG, Higgins GA, Ouagazzal AM, Ozmen L, Kew JN, Bohrmann B, et al. PS2APP transgenic mice, coexpressing hPS2mut and hAPPswe, show age-related cognitive deficits associated with discrete brain amyloid deposition and inflammation. J Neurosci. 2003;23(26):8989-9003.

45. Ozmen L, Albientz A, Czech C, Jacobsen H. Expression of transgenic APP mRNA is the key determinant for beta-amyloid deposition in PS2APP transgenic mice. Neurodegener Dis. 2009;6(1-2):29-36.

46. Allen B, Ingram E, Takao M, Smith MJ, Jakes R, Virdee K, et al. Abundant tau filaments and nonapoptotic neurodegeneration in transgenic mice expressing human P301S tau protein. J Neurosci. 2002;22(21):9340-51.

47. Bellucci A, Westwood AJ, Ingram E, Casamenti F, Goedert M, Spillantini MG. Induction of inflammatory mediators and microglial activation in mice transgenic for mutant human P301S tau protein. Am J Pathol. 2004;165(5):1643-52.

48. Rominger A, Brendel M, Burgold S, Keppler K, Baumann K, Xiong G, et al. Longitudinal assessment of cerebral β-amyloid deposition in mice overexpressing Swedish mutant β-amyloid precursor protein using 18F-florbetaben PET. J Nucl Med. 2013;54(7):1127-34.

49. Brendel M, Jaworska A, Grießinger E, Rötzer C, Burgold S, Gildehaus FJ, et al. Cross-sectional comparison of small animal [18F]-florbetaben amyloid-PET between transgenic AD mouse models. PLoS One. 2015;10(2):e0116678.

50. Ottoy J, Niemantsverdriet E, Verhaeghe J, De Roeck E, Struyfs H, Somers C, et al. Association of short-term cognitive decline and MCI-to-AD dementia conversion with CSF, MRI, amyloid- and (18)F-FDG-PET imaging. Neuroimage Clin. 2019;22:101771.

51. Bouter C, Bouter Y. (18)F-FDG-PET in Mouse Models of Alzheimer's Disease. Front Med (Lausanne). 2019;6:71.

52. Brendel M, Probst F, Jaworska A, Overhoff F, Korzhova V, Albert NL, et al. Glial Activation and Glucose Metabolism in a Transgenic Amyloid Mouse Model: A Triple-Tracer PET Study. J Nucl Med. 2016;57(6):954-60.

53. Cerami C, Iaccarino L, Perani D. Molecular Imaging of Neuroinflammation in Neurodegenerative Dementias: The Role of In Vivo PET Imaging. Int J Mol Sci. 2017;18(5).

54. Liu GJ, Middleton RJ, Hatty CR, Kam WW, Chan R, Pham T, et al. The 18 kDa translocator protein, microglia and neuroinflammation. Brain Pathol. 2014;24(6):631-53.

55. Xiang X, Wind K, Wiedemann T, Blume T, Shi Y, Briel N, et al. Microglial activation states drive glucose uptake and FDG-PET alterations in neurodegenerative diseases. Sci Transl Med. 2021;13(615):eabe5640.

56. Masliah E, Terry RD, DeTeresa RM, Hansen LA. Immunohistochemical quantification of the synapse-related protein synaptophysin in Alzheimer disease. Neurosci Lett. 1989;103(2):234-9.

57. Li S, Cai Z, Zhang W, Holden D, Lin SF, Finnema SJ, et al. Synthesis and in vivo evaluation of [(18)F]UCB-J for PET imaging of synaptic vesicle glycoprotein 2A (SV2A). Eur J Nucl Med Mol Imaging. 2019;46(9):1952-65.

58. Becker G, Dammicco S, Bahri MA, Salmon E. The Rise of Synaptic Density PET Imaging. Molecules. 2020;25(10).

59. Bahri MA, Plenevaux A, Aerts J, Bastin C, Becker G, Mercier J, et al. Measuring brain synaptic vesicle protein 2A with positron emission tomography and [(18)F]UCB-H. Alzheimers Dement (N Y). 2017;3(4):481-6.

60. Bastin C, Bahri MA, Meyer F, Manard M, Delhaye E, Plenevaux A, et al. In vivo imaging of synaptic loss in Alzheimer's disease with [18F]UCB-H positron emission tomography. Eur J Nucl Med Mol Imaging. 2020;47(2):390-402.

61. Edison P, Donat CK, Sastre M. In vivo Imaging of Glial Activation in Alzheimer's Disease. Front Neurol. 2018;9:625.

62. Fowler JS, MacGregor RR, Wolf AP, Arnett CD, Dewey SL, Schlyer D, et al. Mapping human brain monoamine oxidase A and B with 11C-labeled suicide inactivators and PET. Science. 1987;235(4787):481-5.

63. Santillo AF, Gambini JP, Lannfelt L, Långström B, Ulla-Marja L, Kilander L, et al. In vivo imaging of astrocytosis in Alzheimer's disease: an ^{11}C-L-deuteriodeprenyl and PIB PET study. Eur J Nucl Med Mol Imaging. 2011;38(12):2202-8.

64. Rusjan PM, Wilson AA, Miler L, Fan I, Mizrahi R, Houle S, et al. Kinetic modeling of the monoamine oxidase B radioligand [(1)(1)C]SL25.1188 in human brain with high-resolution positron emission tomography. J Cereb Blood Flow Metab. 2014;34(5):883-9.

65. Carter SF, Scholl M, Almkvist O, Wall A, Engler H, Langstrom B, et al. Evidence for astrocytosis in prodromal Alzheimer disease provided by 11C-deuterium-L-deprenyl: a multitracer PET paradigm combining 11C-Pittsburgh compound B and 18F-FDG. J Nucl Med. 2012;53(1):37-46.

66. Nag S, Varrone A, Tóth M, Thiele A, Kettschau G, Heinrich T, et al. In vivo evaluation in cynomolgus monkey brain and metabolism of [^{18}F]fluorodeprenyl: a new MAO-B pet radioligand. Synapse. 2012;66(4):323-30.

67. Nag S, Fazio P, Lehmann L, Kettschau G, Heinrich T, Thiele A, et al. In Vivo and In Vitro Characterization of a Novel MAO-B Inhibitor Radioligand, 18F-Labeled Deuterated Fluorodeprenyl. J Nucl Med. 2016;57(2):315-20.

68. Villemagne VL, Harada R, Doré V, Furumoto S, Mulligan R, Kudo Y, et al. Assessing Reactive Astrogliosis with ^{18}F-SMBT-1 Across the Alzheimer Disease Spectrum. Journal of Nuclear Medicine. 2022;63(10):1560-9.

69. Villemagne VL, Harada R, Doré V, Furumoto S, Mulligan R, Kudo Y, et al. First-in-Humans Evaluation of 18F-SMBT-1, a Novel 18F-Labeled Monoamine Oxidase-B PET Tracer for Imaging Reactive Astrogliosis. Journal of Nuclear Medicine. 2022;63(10):1551-9.

70. Zhou R, Ji B, Kong Y, Qin L, Ren W, Guan Y, et al. PET Imaging of Neuroinflammation in Alzheimer's Disease. Front Immunol. 2021;12:739130.

71. Jack CR, Jr., Bennett DA, Blennow K, Carrillo MC, Dunn B, Haeberlein SB, et al. NIA-AA Research Framework: Toward a biological definition of Alzheimer's disease. Alzheimers Dement. 2018;14(4):535-62.

72. Zimmer ER, Parent MJ, Souza DG, Leuzy A, Lecrux C, Kim HI, et al. [(18)F]FDG PET signal is driven by astroglial glutamate transport. Nat Neurosci. 2017;20(3):393-5.

73. Xiong M, Roshanbin S, Rokka J, Schlein E, Ingelsson M, Sehlin D, et al. In vivo imaging of synaptic density with [(11)C]UCB-J PET in two mouse models of neurodegenerative disease. Neuroimage. 2021;239:118302.

74. Arriagada PV, Growdon JH, Hedley-Whyte ET, Hyman BT. Neurofibrillary tangles but not senile plaques parallel duration and severity of Alzheimer's disease. Neurology. 1992;42(3 Pt 1):631-9.

75. Long JM, Holtzman DM. Alzheimer Disease: An Update on Pathobiology and Treatment Strategies. Cell. 2019;179(2):312-39.

76. Chen MK, Mecca AP, Naganawa M, Gallezot JD, Toyonaga T, Mondal J, et al. Comparison of [(11)C]UCB-J and [(18)F]FDG PET in Alzheimer's disease: A tracer kinetic modeling study. J Cereb Blood Flow Metab. 2021;41(9):2395-409.

77. Delva A, Michiels L, Koole M, Laere KV, Vandenberghe W. Synaptic Damage and Its Clinical Correlates in People With Early Huntington Disease. A PET Study. 2022;98(1):e83-e94.

III. Danksagung

An erster Stelle möchte ich meinem Doktorvater Prof. Dr. med. Matthias Brendel (Klinik und Poliklinik für Nuklearmedizin der Universität München) für die Überlassung dieser spannenden Themen und die exzellente Betreuung danken. Durch seine hilfsbereite und engagierte Art half er mir die ersten unsicheren Schritte im Bereich der Nuklearmedizin zu gehen und stand mir bei jeder noch so kleinen Frage und Unsicherheit unterstützend zur Seite.

Vielen Dank auch an Prof. Dr. med. Peter Bartenstein als damaligen klinischen Direktor, für die Ermöglichung der Forschungsarbeiten im Rahmen meiner kumulativen Dissertation.

Auch Karin Bormann-Giglmaier und Giovanna Palumbo möchte ich für die harmonische, kompetente und hilfsbereite Zusammenarbeit bei der praktischen Umsetzung der Studien Danke sagen.

Darüber hinaus danke ich meiner Doktorandinkollegin Letizia Vogler. Die Zusammenarbeit mit dir war immer von Spaß und Produktivität geprägt.

Ich bin meinen Familien für die Unterstützung im Studium und dem stetigen Glauben in mich und meine Fähigkeiten sehr dankbar.

Zu guter Letzt geht mein größter Dank an meinen Ehemann Stephan, der immer an mich glaubt, mich bedingungslos unterstützt und hinter mir steht. Ohne dich hätte ich diese großen Meilensteine nicht geschafft.